Karlsruher Institut für Technologie

DIFFERENTIAL MEASUREMENTS OF THE SINGLE TOP QUARK CROSS SECTION IN THE t-CHANNEL WITH THE CMS EXPERIMENT AT $\sqrt{s} = 8$ TEV

Zur Erlangung des akademischen Grades eines
DOKTORS DER NATURWISSENSCHAFTEN
von der Fakultät für Physik des
Karlsruher Institut für Technologie (KIT)

genehmigte

DISSERTATION

von

Dipl.-Phys. Steffen Röcker
aus Sindelfingen

Mündliche Prüfung: 19. Juni 2015

Referent: Prof. Dr. Th. Müller

Korreferent: Prof. Dr. G. Quast

Für Kurt

Contents

List of Figures **v**

List of Tables **ix**

Introduction **1**

1. Theoretical Framework **3**
1.1. Standard Model of Particle Physics 3
1.1.1. Fermions and Bosons 4
1.1.2. Electroweak Symmetry Breaking and the Higgs Mechanism . . . 6
1.1.3. Quark Mixing and the CKM Matrix 8
1.2. Hard Scattering Processes 8
1.3. Top Quark Physics 12
1.3.1. Top Quark Pair Production 12
1.3.2. Single Top Quark Production 13
1.4. Top Quark Properties 17
1.4.1. Top Quark Mass 17
1.4.2. Top Quark Decay 18
1.4.3. Top Quark Spin Polarization 19

2. Experimental Status of Single Top Quark Production **21**
2.1. Cross Section Measurements 21
2.1.1. 7 TeV Measurement 21
2.1.2. 8 TeV Measurement 22
2.2. Determination of the CKM Matrix Element $|V_{tb}|$ 26
2.3. Top Quark Width 26
2.4. Top Quark Polarization 27

3. The Large Hadron Collider and CMS Detector **31**
3.1. The Large Hadron Collider 31
3.2. The Compact Muon Solenoid Detector 35
3.3. Computing Infrastructure 40
3.4. Reconstruction of Detector Objects 43
3.4.1. Particle Flow Reconstruction 43
3.4.2. Tracks 43
3.4.3. Vertices 44
3.4.4. Muons 44

    3.4.5. Electrons 45
    3.4.6. Jets 46
    3.4.7. Missing Transverse Energy 49

4. Simulation of Single Top Quark Production 51
  4.1. Monte Carlo Simulation 51
  4.2. Parton Showers and Monte Carlo Generators 53
  4.3. Simulation of *t*-channel Single Top Quark Physics 55

5. Event Selection and Signal Event Reconstruction 57
  5.1. Utilized Data Samples 57
  5.2. Background Processes 58
    5.2.1. Top Quark Production 58
    5.2.2. Vector Boson Production 58
    5.2.3. Diboson Production 60
    5.2.4. QCD Multijet Production 60
  5.3. Event Selection 61
  5.4. Data-driven Estimation of QCD Multijet Background 65

6. Multivariate Neural Network Analysis 71
  6.1. Theory of Neural Networks 71
  6.2. Selection of Input Variables 75
  6.3. Neural Network Training 77
  6.4. Estimation of Optimal Cut Values 85
  6.5. Background and Signal Estimation 85
  6.6. Resulting Templates 88

7. Differential Cross Section Measurements 91
  7.1. Background Subtraction 92
  7.2. Regularized Unfolding 92
  7.3. Closure Tests of the Unfolding Procedure 98
  7.4. Estimation of Systematic Uncertainties 103
  7.5. Results 113

8. Summary and Outlook 117
  8.1. Summary 117
  8.2. Outlook 118

Appendix 119

A. Statistical Methods 121
  A.1. Best Linear Unbiased Estimator (BLUE) 121

B. Event Shape Variables 123

C. Input variables **125**
C.1. Muon channel 125
C.2. Electron channel 132

Bibliography **139**

List of Figures

1.1. Mexican hat potential of the Higgs field. 7
1.2. Feynman diagrams of fundamental interactions. 8
1.3. Standard Model cross sections as a function of collider energy. 10
1.4. CT10 parton distribution functions at NLO. 11
1.5. Leading order Feynman diagrams of top quark pair production ($t\bar{t}$). . . . 12
1.6. Leading order Feynman diagrams of single top quark production. 13
1.7. LO Feynman diagram for single top quark *s*-channel production. 14
1.8. NLO Feynman diagrams for *s*-channel production. 14
1.9. Feynman diagram for single top quark *t*-channel production. 15
1.10. NLO Feynman diagrams for *t*-channel production. 15
1.11. Feynman diagram for associated single top quark production (tW). . . . 16
1.12. NLO Feynman diagrams for associated production (tW). 17
1.13. Spin analyzing powers of top quark decay products. 20

2.1. Pseudorapidity of the light quark jet η_{lj} in the 7 TeV measurement. . . . 22
2.2. Distributions of the NN discriminator output in the muon channel. . . . 22
2.3. Pseudorapidity of the light quark jet η_{lj} in the 8 TeV measurement. . . . 23
2.4. Single top quark production cross sections vs. center-of-mass energy. . . 24
2.5. Measured charge ratio compared to predictions with different PDF sets. 25
2.6. Unfolded distributions of $\cos\theta_l^*$. 27
2.7. BDT discriminator and $\cos\theta_l^*$ for the top quark polarization analysis. . . 29

3.1. Schematic layout of the LHC and CERN accelerator complex. 32
3.2. Total integrated luminosity for 2012. 34
3.3. Schematic overview of the CMS detector. 35
3.4. Schematic overview of the CMS tracking system. 36
3.5. Longitudinal view of one quarter of the CMS detector. 39
3.6. Longitudinal view of one quarter of the CMS muon system. 40
3.7. Architecture of the CMS Data Acquisition System. 41
3.8. Schematic overview of the CMS computing grid. 42
3.9. Schematic view of a B hadron decay inside a jet. 48
3.10. Discriminator values for the CSV algorithm. 49

4.1. Schematic illustration of the factorization of a proton-proton collision. . 52
4.2. Single top quark *t*-channel production in the 4- and 5-flavor scheme. . . 55
4.3. Transverse momentum p_{T} of the top quark and second b quark generated with aMC@NLO at NLO in the 4FS and 5FS. 56

5.1. Vector boson production. 58
5.2. Diboson production. 60
5.3. QCD multijet production. 61
5.4. Purity of the QCD multijet sideband selection. 67
5.5. QCD multijet sideband templates in the 2j1t region. 68
5.6. QCD multijet sideband templates in the 3j2t region. 69

6.1. Logistic sigmoid activation function. 72
6.2. Representation of a feed-forward neural network. 72
6.3. Visualization of overtraining. 74
6.4. Two of the most important input variables for the muon channel. 78
6.5. Tow of the most important input variables for the muon channel. 79
6.6. Correlation between the input variables. 82
6.7. Neural network training discriminator shapes. 82
6.8. Signal purity versus network discriminator. 83
6.9. Signal purity versus signal efficiency. 83
6.10. Neural network discriminator in the signal region (2j1t). 84
6.11. Neural network discriminator in the $\mathrm{t\bar{t}}$ control region (3j2t). 84
6.12. Neural network discriminator scan. 85
6.13. Distribution of top quark transverse momentum p_{T} and rapidity $|y|$. . . 88

7.1. Schematic representation of the unfolding procedure. 92
7.2. Selection efficiencies for top quark p_{T} and $|y|$. 95
7.3. Shape comparison of top quark p_{T} and $|y|$ at generator level. 96
7.4. Migration matrices for top quark p_{T} and $|y|$. 97
7.5. Relative differences for top quark p_{T}. 99
7.6. Relative differences for top quark $|y|$. 100
7.7. Pulls for top quark p_{T}. 101
7.8. Pulls for top quark $|y|$. 102
7.9. Effect on top-quark p_{T} due to systematic variations. 107
7.10. Effect on top-quark p_{T} due to systematic variations. 108
7.11. Effect on top-quark p_{T} due to systematic variations. 109
7.12. Effect on top-quark rapidity due to systematic variations 110
7.13. Effect on top-quark rapidity due to systematic variations 111
7.14. Effect on top-quark rapidity due to systematic variations 112
7.15. Normalized differential cross sections of top-quark p_{T} and $|y|$. 115

C.1. Muon channel input variables. η_{lq}, $m_{\ell\nu\mathrm{b}}$ and $m_{\mathrm{jet1,jet2}}$. 126
C.2. Muon channel input variables. $m_{\mathrm{T,W}}$, Q_{ℓ} and m_{lq}. 127
C.3. Muon channel input variables. η_{W}, $\Delta\phi[\ell, lq]$ and $m_{b_{top}}$. 128
C.4. Muon channel input variables. $\Delta\phi(jet1, \not{E}_{\mathrm{T}})$, C and $p_{\mathrm{T,lq}}$. 129
C.5. Muon channel input variables. D, m_{jet1} and $\not{E}_{\mathrm{T}}$. 130
C.6. Muon channel input variables. $\Delta\phi(jet2, \not{E}_{\mathrm{T}})$, m_{jet2} and $\Delta R(jet1, \not{E}_{\mathrm{T}})$. . . . 131
C.7. Electron channel input variables. η_{lq}, $m_{\ell\nu\mathrm{b}}$ and $m_{\mathrm{jet1,jet2}}$. 133

C.8. Electron channel input variables. $m_{\mathrm{T,W}}$, m_{jet1} and Q_{ℓ}. 134
C.9. Electron channel input variables. η_{W}, m_{jet2} and $p_{\mathrm{T,lq}}$. 135
C.10. Electron channel input variables. $\Delta\phi[jet2,\ell]$, $\Delta\phi[\ell,lq]$ and C. 136
C.11. Electron channel input variables. m_{lq}, $\not{E}_{\mathrm{T}}$ and $\Delta R(jet1,\not{E}_{\mathrm{T}})$. 137
C.12. Electron channel input variables. $\Delta\phi(jet2,\not{E}_{\mathrm{T}})$, D and A. 138

List of Tables

1.1. List of fermions in the standard model. 5
1.2. List of bosons in the standard model. 6
1.3. Predicted s-channel single top quark production cross sections. 14
1.4. Predicted single top quark t-channel production cross sections. 16
1.5. Predicted associated (tW) single top quark production cross sections. . . 17
1.6. Decay modes of the W^+ boson. 19

5.1. List of utilized Monte Carlo samples. 59
5.2. Matching of reconstructed jets to generator level partons. 65
5.3. Estimation of QCD multijet events in the signal and $\mathrm{t\bar{t}}$ control region. . . 68

6.1. Input variable ranking in the muon channel. 80
6.2. Input variable ranking in the electron channel. 81
6.3. Scale factors for the neural network discriminator fit in the muon channel. 87
6.4. Scale factors for the neural network discriminator fit in the electron channel. 87
6.5. Event yield in the muon channel after NN cut. 89
6.6. Event yield in the electron channel after NN cut. 89

7.1. Systematic uncertainties for the unfolding of top p_{T}. 105
7.2. Systematics uncertainties for the unfolding of top $|y|$. 106
7.3. Normalized differential cross sections of top-quark p_{T}. 114
7.4. Normalized differential cross sections of top-quark $|y|$. 114

Introduction

“Yesterday’s sensation is today’s calibration.” — R. P. Feynman
“. . . and tomorrow’s background.” — V. L. Telegdi

The standard model of particle physics has defied all challenges of the last few years and has been established with great success and precision. The first run of the Large Hadron Collider (LHC), the most powerful particle collider built to date, enabled precise measurements of particle properties and the discovery of the last missing piece of the standard model, the Higgs boson. Although the standard model seems to be complete now, a lot of questions are still unanswered. A couple of measurements deviate from the standard model predictions and hint that new physics must play a role. One key role in the standard model is played by the top quark, the heaviest known elementary particle. Due to its high mass the top quark is supposed to play an important role in electroweak symmetry breaking.

The recently finished shutdown phase of the LHC, required for the upgrade of the center-of-mass energy, was used to precisely analyze the currently available data and measure interesting observables with great scrutiny and precision to refine and prepare the state-of-the-art for the current Run II of the LHC. This thesis attempts to improve the understanding of the electroweak production of single top quarks. The electroweak production of single top quarks is a unique process which allows a detailed study of the electroweak force and the properties of the top quark, e.g its polarization. The measurement of the single top quark cross section allows to constrain the magnitude of the CKM matrix element V_{tb}, which can be used to exclude the existence of a possible fourth generation.

Since the establishment of single top quark production, in 2009 at the Tevatron, a vast amount of data has now been collected at the LHC. This enables a detailed study of top quark physics, even in single top quark production which has changed from yesterday’s signal to precision measurement and calibration and will play an important role in future searches for Higgs boson production in association with single top quarks.

This thesis introduces the theory of single top quark production and describes the cross section and property measurements performed by the CMS Collaboration in the context of the work performed during the creation of this thesis. The main focus of this thesis lies on the description of a differential cross section measurement of the top quark transverse momentum p_{T} and rapidity $|y|$ in the single top quark t-channel production mode. The analysis employs a multivariate technique, i.e. a neural network, to separate signal from background events with similar topologies and to create a signal enriched dataset. Detector reconstruction effects and selection efficiencies are corrected for with an unfolding method. Predictions from several Monte Carlo generators are compared with the corrected measured distributions. Differential measurements are well suited to establish the accuracy of current Monte Carlo generators and simulation techniques and to look for deviations from known physics.

This thesis is structured as follows: First a brief introduction to the theoretical framework of particle physics is given in Chapter 1. The current experimental status of single top quark measurements with contributions made in the scope of this thesis is summarized in Chapter 2. The experimental setup, consisting of the accelerator and detector, is described in Chapter 3. The reconstruction and simulation of the involved processes and particles are described at the end of Chapter 3 and in Chapter 4, respectively. The selection of particularly interesting events is described in Chapter 5. Chapter 6 describes the utilized neural network technique to further discriminate between signal and background events. In Chapter 7 a brief introduction and description of the unfolding procedure used to correct detector resolution and selection efficiencies is given. The background estimation and consistency checks are described before the systematic uncertainties and the result itself are discussed. Finally, a summary and outlook is given in Chapter 8.

For the sake of simplicity natural units are used in the following, $\hbar = c = 1$.

1. Theoretical Framework

Three of the four known fundamental forces are described by the standard model (SM) of particle physics. The SM is a quantum field theory which describes the interaction of elementary particles with the electromagnetic, weak and strong force. No current known framework allows to include the fourth fundamental force, gravity, for which only a classical field theory is known [1], into a so-called Theory of Everything. Although the SM correctly describes reasonably well most experimental observations made at colliders, recent cosmological measurements have shown that only around 4% of the matter in our universe is explained by the SM. The SM can not explain the bulk of matter and energy for which there is very strong evidence from cosmological observations: dark matter and dark energy [2]. Despite its shortcomings, the SM has been very successful in predicting particles and their properties before their discoveries. The most recent and exciting discovery was that of the Higgs boson [3,4], the last missing piece of puzzle in a self-coherent theory with massive particles.

In the following, a brief introduction to the SM is given. A more detailed introduction can be found in Ref. [5], an introduction focused on the theoretical foundations in Ref [6]. The historical development of quantum field theories and the SM is nicely summarized in Ref. [7].

1.1. Standard Model of Particle Physics

The dynamics of the elementary particles and fields of the SM are described by a Lagrangian. The symmetries of the SM are described by the Lie group $\mathrm{SU}(3)_C \times \mathrm{SU}(2)_L \times \mathrm{U}(1)_Y$. According to Noether's theorem [8] every global symmetry of the Lagrangian implies the conservation of a charge. The gauge symmetries of the SM lead to the conservation of the color charge (C), the weak isospin charge (L) and the weak hypercharge (Y). The unification of the weak and electromagnetic interaction was described by the Glashow-Weinberg-Salam theory [9–11].
The Lagrangian of the SM consists of the following four terms

$$\mathcal{L} = \mathcal{L}_{\mathrm{Yang-Mills}} + \mathcal{L}_{\mathrm{Fermions}} + \mathcal{L}_{\mathrm{Higgs}} + \mathcal{L}_{\mathrm{Yukawa}} \,, \tag{1.1}$$

which describe the dynamics of the gauge bosons ($\mathcal{L}_{\mathrm{Yang-Mills}}$) and fermions ($\mathcal{L}_{\mathrm{Fermions}}$) for the unbroken symmetry as well as the Higgs field ($\mathcal{L}_{\mathrm{Higgs}}$) and mass terms from the electroweak symmetry breaking ($\mathcal{L}_{\mathrm{Yukawa}}$).

The Yang-Mills term describes the free propagation of the gauge bosons and their self interactions. Since observed particles are massive and local gauge invariance forbids the addition of a mass term, a different concept has to be used to add massive particles to the SM. The last two terms introduced by electroweak symmetry breaking (EWSB) and the Higgs mechanism are explained in Section 1.1.2.

1.1.1. Fermions and Bosons

Each elementary particle has an internal quantum number called spin. Elementary particles are either of integer spin, e.g 0 or 1, or half integer spin, e.g $\frac{1}{2}$. Particles with integer spin are mediators of forces and called bosons. All gauge particles are bosons. Particles with half integer spin are called fermions.

Fermions

Fermions obey the Pauli principle, which forbids that two fermions can occupy the same quantum state. Fermions are classified into leptons and quarks. Leptons interact via the electroweak interaction, quarks via the strong and electroweak interaction. The leptons and quarks are grouped into three generations with a mass hierarchy. Each generation consists of two quarks, up and down type, a charged lepton and a corresponding neutrino. Neutrinos only interact via the weak force. The properties of the three generations are given in Table 1.1. The corresponding anti-particles are not listed, they have the same quantum numbers but opposite charge.

Quarks have an electric charge of either $2/3$ in units of the elementary charge e like the up, charm and top quark; or $-1/3$ like the down, strange and bottom quark. Outside hadrons quarks can not exist alone due to color confinement. When two quarks are beginning to separate, the gluon field between them forms strings of color charge which hold them together like a rubber band. Near each other quarks are asymptotically free. Each quark has a color charge which is either red, green or blue. Anti-quarks carry the corresponding anti-color. Together with gluons, the gauge bosons of the strong interaction, the quarks make up composite fermions called hadrons. Composites of quarks have to be colorless. Hadrons with two quarks are called mesons, e.g. kaons and pions. Hadrons made up of three quarks are called baryons, e.g. protons or neutrons. The dynamics of quarks and gluons are described by quantum chromodynamics (QCD).

Fermion masses in the SM are free parameters, the values are not predictable and have to be measured. The masses of the fermions increase with each generation. Why such a mass hierarchy exists in the SM is still an open question in particle physics.

The observation of neutrino oscillations shows that neutrinos must have non-vanishing masses as well [12]. The latest data from the Planck satellite [2] underpins the observation that neutrinos come in three generations. Together with observations from other telescopes the mass of all three known neutrinos is constrained to be less than 0.21 eV. The KATRIN experiment [13] will measure the upper bound of the electron

Table 1.1.: List of fermions in the standard model and their properties. The three generations of quarks and leptons, their masses and electric charges are shown [12]. The top quark mass is taken from Ref. [14]. Electric charges are given in units of the elementary charge e. Anti-particles have opposite charge.

Name	Symbol	Electric Charge [e]	Mass [MeV]
up quark	u	$+\frac{2}{3}$	$2.3^{+0.7}_{-0.5}$
down quark	d	$-\frac{1}{3}$	$4.8^{+0.5}_{-0.3}$
electron	e	-1	0.511
electron neutrino	ν_e	0	$< 2.2 \cdot 10^{-6}$
charm quark	c	$+\frac{2}{3}$	$(1.275 \pm 0.025) \cdot 10^3$
strange quark	s	$-\frac{1}{3}$	95 ± 5
muon	μ	-1	105.7
muon neutrino	ν_μ	0	< 0.17
top quark	t	$+\frac{2}{3}$	$(173.34 \pm 0.76) \cdot 10^3$
bottom quark	b	$-\frac{1}{3}$	$(4.18 \pm 0.03) \cdot 10^3$
tau	τ	-1	1776.82 ± 0.16
tau neutrino	ν_τ	0	< 15.5

anti-neutrino mass in the next few years and probably will give a hint how the hierarchy of the neutrino mass eigenstates is ordered.

Bosons

Bosons are integer spin particles, i.e. their behavior is described by Bose-Einstein statistics. The bosons governing the interactions of the SM are the photon, the neutral Z^0 boson, the charged W^+ and W^- bosons and the eight gluons. In addition, the Higgs boson is a remanent scalar with spin 0 of the Higgs mechanism, described in Section 1.1.2.

Photons are massless bosons with spin 1 and no electric charge and mediate the electromagnetic force. The gauge bosons of the electroweak force after EWSB are the $W^\pm$ and Z^0 bosons with spin 1. The Z^0 boson has no electric charge and a mass of around 91.2 GeV. W bosons either have positive, W^+, or negative, W^-, charge and a mass of around 80.4 GeV. Since the Z boson and W bosons have mass the range of the electroweak force is limited. Gluons are massless and have a simultaneous color and anti-color charge with eight possible independent combinations. Gluons are the gauge bosons of the strong interaction described by quantum chromodynamics and mediate the strong force between quarks and themselves.

The properties of the standard model bosons are summarized in Table 1.2.

Table 1.2.: List of bosons in the standard model.

Name	Symbol	Force	Electric Charge [e]	Mass [GeV]
Photon	γ	Electromagnetic	0	0
W bosons	$W^{\pm}$	Weak	± 1	80.385 ± 0.015
Z boson	Z^0	Weak	0	91.1876 ± 0.0021
Gluons	g	Strong	0	0

1.1.2. Electroweak Symmetry Breaking and the Higgs Mechanism

The Lagrangian of the SM is not allowed to have a mass term since this would violate local gauge invariance. Since the observed gauge bosons $W^{\pm}$, Z and fermions carry mass there must be another mechanism generating mass.

The answer is to generate the masses with a spontaneous electroweak symmetry breaking according to the Higgs-Brout-Englert-Guralnik-Hagen-Kibble mechanism [15–18], which will from now on be referred to as Higgs mechanism for simplicity. The last missing piece of the SM, the Higgs boson, was recently discovered by the ATLAS and CMS collaborations which lead to the Nobel price for Peter Higgs and François Englert in 2012.

An additional $SU(2)$ doublet of complex scalar fields is introduced to the SM Lagrangian. The Lagrangian density of this field is

$$\mathcal{L} = \frac{1}{2}\partial_{\mu}\partial^{\mu}\phi - V(\phi)\,, \tag{1.2}$$

where the Higgs potential $V(\phi)$ is given by

$$V(\phi) = \frac{1}{2}\mu^2\phi^2 + \frac{1}{4}\lambda\phi^4\,, \tag{1.3}$$

with a mass term μ^2 and self coupling term λ. When the mass term is negative $\mu^2 < 0$ the potential $V(\phi)$ has a local maximum and an infinite number of local minima, i.e a degenerate vacuum. This potential is known as the Mexican hat potential, shown in Fig. 1.1.

The minimum occurs at $\phi = e^{i\theta}\sqrt{\frac{\mu^2}{2\lambda}} = e^{i\theta}$. If one chooses $\theta = 0$ for the vacuum this breaks the U(1) invariance and the field ϕ has a non-zero vacuum expectation value (VEV) of $<\phi>= \frac{v}{\sqrt{2}}$, which results as seen later with the known values of the W boson and Z boson mass in $v \approx 246$ GeV. Since there are possible excitations that change the state of the vacuum but not the energy there must exist massless particles. The Goldstone theorem postulates that every broken symmetry with N degrees of freedom leads to $N - m$ massless scalar bosons, where m is the number of generators that leave the vacuum invariant. These bosons are called Goldstone bosons. In the case of $U(1)$ this leads to exactly one Goldstone boson [20–22].

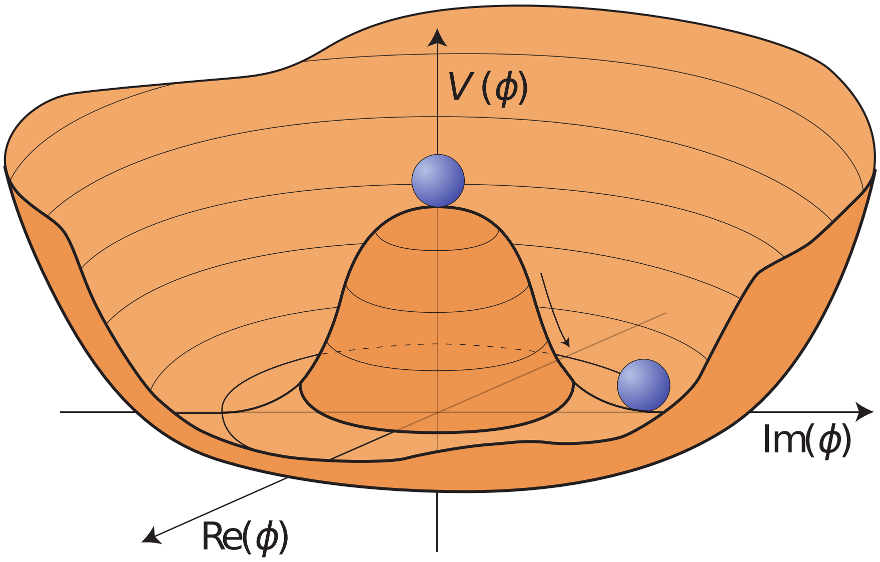

Figure 1.1.: Mexican hat potential of the Higgs field. Shown are the real and imaginary parts of the field ϕ introduced in Eq. (1.3). For the case of $\mu^2 < 0$ there are an infinite number of local minima around the vacuum expectation value of v. The blue ball symbolizes how the symmetry is spontaneous broken by rolling from the unstable local maximum to one of the local minima [19].

In the case of local symmetries the Goldstone bosons are "eaten" up by the gauge bosons which thereby gain their masses. One degree of freedom remains, which leads to the appearance of a massive scalar particle, the Higgs boson.

The non-zero vacuum expectation value breaks the electroweak symmetry and generates the masses of the gauge bosons

$$M_W = \frac{1}{2} g v, \quad M_Z = \frac{1}{2}\sqrt{g^2 + g'^2} v \tag{1.4}$$

where g and g' are free parameters.

The mass of the W boson and Z boson are related by the Weinberg angle. It can be expressed by the $SU(2)_L$ and $U(1)_Y$ coupling constants

$$\cos\theta_W = \frac{g}{\sqrt{g^2 + g'^2}}, \tag{1.5}$$

and can be written and measured in terms of the W boson and Z boson mass

$$\cos\theta_W = \frac{m_W}{m_Z}. \tag{1.6}$$

Fermions get their mass via the Yukawa coupling to the Higgs field. The Yukawa part of the Lagrangian couples the left and right handed up and down-type spinors to the

Yukawa coupling matrices. Since no right-handed neutrinos exist in the SM, the Yukawa coupling is not responsible for the observed Neutrino masses and there must be another mechanism, for example seesaw, responsible for generating these very small masses.

1.1.3. Quark Mixing and the CKM Matrix

The masses and mixings of the quarks arise from the Yukawa interaction with the Higgs field. Since the mass eigenstates (d, s, b) are not the same as the flavor eigenstates (d', s', b') quarks can mix. The mixings are described by the Cabbibo-Kobayashi-Maskawa (CKM) matrix [23,24], a 3 × 3 unitary matrix in the SM:

$$\begin{pmatrix} d' \\ s' \\ b' \end{pmatrix} = \begin{pmatrix} V_{ud} & V_{us} & V_{ub} \\ V_{cd} & V_{cs} & V_{cb} \\ V_{td} & V_{ts} & V_{tb} \end{pmatrix} \begin{pmatrix} d \\ s \\ b \end{pmatrix} . \tag{1.7}$$

Imposing the SM constraints (three generations, unitarity) the CKM matrix elements can be determined with a global fit [12] from several different measurements:

$$|V_{\mathrm{CKM}}| = \begin{pmatrix} 0.97427 \pm 0.00014 & 0.22536 \pm 0.00061 & 0.00355 \pm 0.00015 \\ 0.22522 \pm 0.00061 & 0.97343 \pm 0.00015 & 0.0414 \pm 0.0012 \\ 0.00886^{+0.00033}_{-0.00032} & 0.0405^{+0.0011}_{-0.0012} & 0.99914 \pm 0.00005 \end{pmatrix} . \tag{1.8}$$

The absolute squares of the matrix elements state the transition rates between the different flavor eigenstates. The small values in the off-diagonal entries in the last row lead to the fact, that top quarks almost exclusively decay into b quarks and W bosons.

1.2. Hard Scattering Processes

Fundamental interactions can be illustrated with Feynman diagrams [25]. Feynman diagrams for typical fundamental interactions are shown in Fig. 1.2.

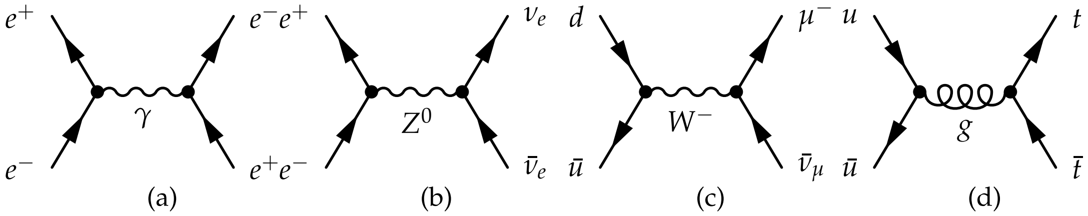

Figure 1.2.: Leading order Feynman diagrams of fundamental interactions. Time is evolving from left to right. As an example for electromagnetic interaction, electron-positron annihilation is shown in (a). Examples for the weak interaction are shown in (b) and (c). The annihilation of two quarks via the strong force is shown in (d).

These diagrams can be translated with Feynman rules into formulas to calculate the transition amplitude $\mathcal{M}$. The cross section of a given interaction can be calculated by integrating the transition amplitude over the complete phase space, taking into account all possible initial and final states. Cross sections are a measure of probability of an interaction and are typically given in the unit barn with $1\mathrm{b} = 10^{-28}\,\mathrm{m}^2$. Typical SM cross sections are shown in Fig. 1.3. The single top quark t-channel cross section, shown in red as σ_t, is around 11 magnitudes smaller than the total proton-antiproton cross section.

Parton Distribution Functions

The substructure of the proton consists of partons. A proton consists of two up quarks and one down quark. These valence quarks are bound through the exchange of virtual gluons. Additionally, virtual quark anti-quarks pairs are constantly created and destroyed by vacuum fluctuations and gluon splitting.

Knowledge about parton distribution functions (PDFs) is obtained mostly through deep inelastic scattering experiments, i.e. $ep+ \rightarrow eX$ collisions. Only in recent times, data from the LHC experiments is used to constrain some PDFs. The DGLAP (Dokshitzer [27], Gribow, Lipatow [28], Altarelli, Parisi [29]) QCD evolution function is used to calculate PDFs at different energy scales Q^2.

Parton distribution functions and the hard matrix element are assumed to collinear factorize in Monte Carlo (MC) generators based on the DGLAP evolution. The total cross section σ for a process $AB \rightarrow cd + X$ in this ansatz is then

$$\sigma(AB \rightarrow cd + X) = \sum_{i,j} \int dx_i dx_j f_{i/A}(x_i, \mu_F^2) f_{i/B}(x_i, \mu_F^2) \times \hat{\sigma_{ij}}(ij \rightarrow cd; \hat{s}, \mu_R^2, \mu_F^2)\,, \quad (1.9)$$

where $f_{i/A}(x_i, \mu_F^2)$ is the probability density to find a parton i with a longitudinal momentum fraction $x_i = \frac{p_i}{p_A}$ inside a hadron A, μ_F is the factorization scale describing the typical energy scale of the process, μ_R the renormalization scale of QCD and $\hat{\sigma_{ij}}(ij \rightarrow cd; \hat{s}, \mu_R^2, \mu_F^2)$ the partonic cross section of the hard interaction.

The square of the center-of-mass energy can be written in terms of the total hadronic center-of-mass energy, $s = (p_A + p_B)^2$, as $\hat{s} \approx x_i x_j s$. When the two incoming hadrons have the same energy E and negligible mass m, this formula reduces to $\hat{s} = 4x_i x_j E^2$.

Up to the factorization scale μ_F the process is calculated with the matrix element (ME) and then showered with the parton shower (PS), where the radiation of gluons and the subsequent radiation is simulated. Further splitting of gluons is parametrized with Sudakov form factors, using the DGLAP equation.

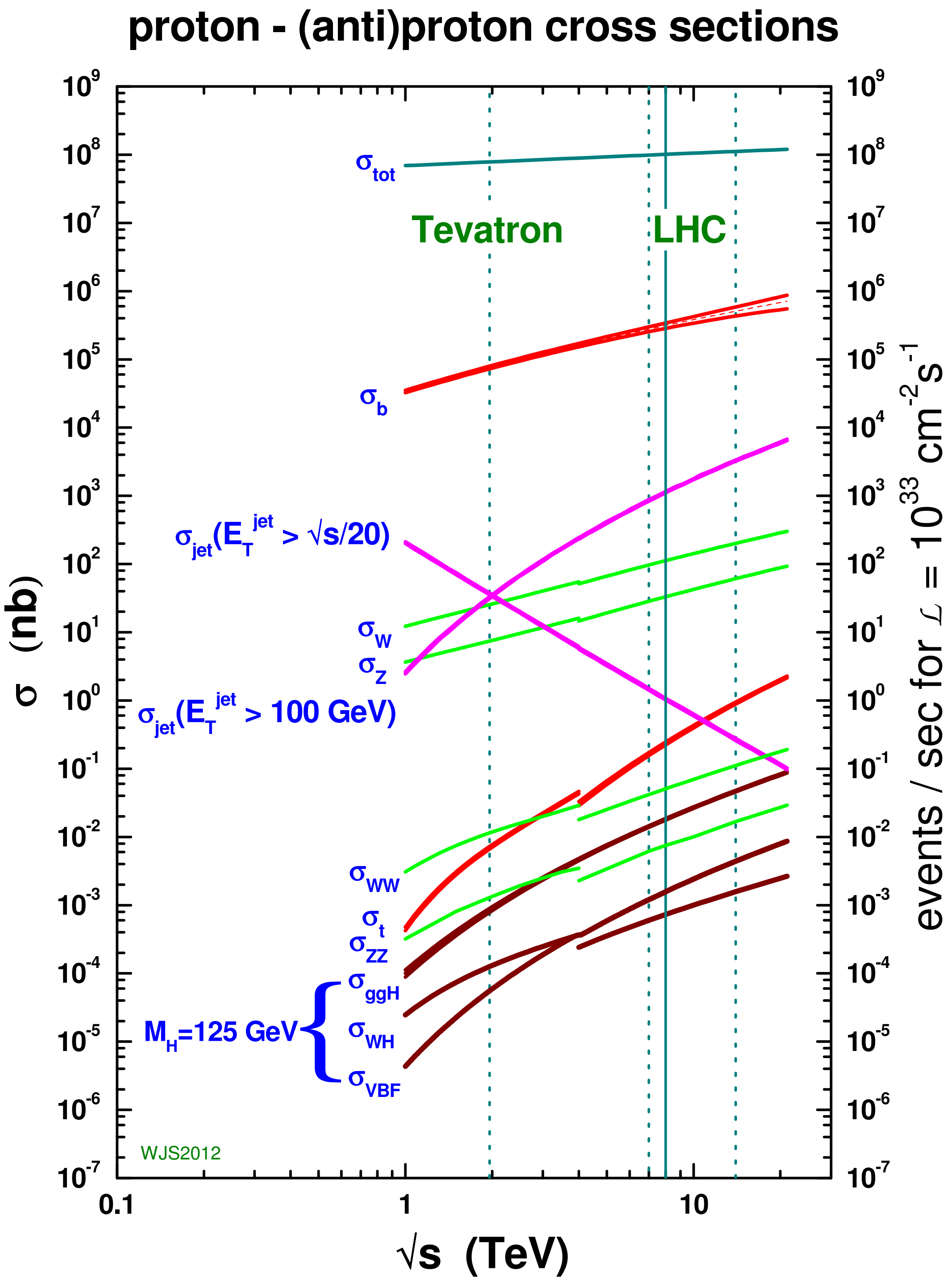

Figure 1.3.: Standard model cross sections as a function of collider energy [26].

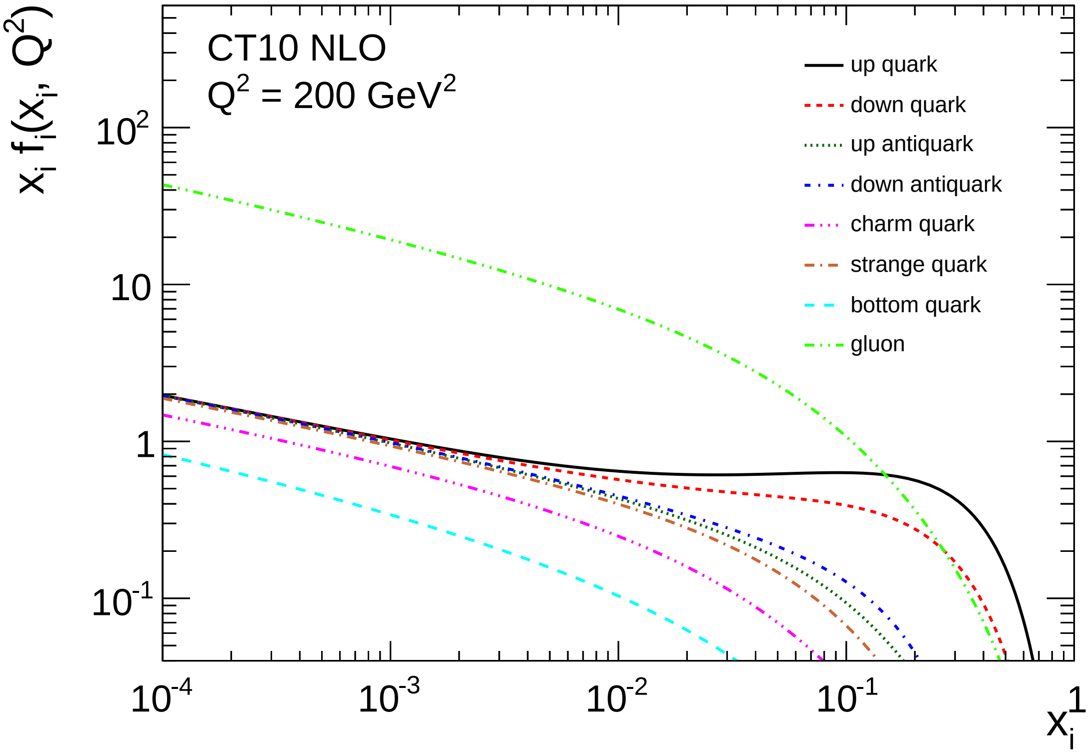

Figure 1.4.: CT10 [30] parton distribution functions for $u, \bar{u}, d, \bar{d}, c, s, b$ quarks and gluons at NLO. The energy scale was set to $Q^2 = 200$ GeV^2.

1.3. Top Quark Physics

The top quark is the heaviest known elementary particle. It was discovered in 1995 at the Tevatron by the CDF and DØ experiments [31,32]. Its mass of $173.34 \pm 0.27(\text{stat.}) \pm 0.71(\text{syst.})$ GeV [14], approximately the same as a tungsten atom, leads to a very short lifetime. Due to this large mass, it is suspected to play an important role in EWSB.

1.3.1. Top Quark Pair Production

Most top quarks at the LHC are produced in pairs via the flavor conserving strong interaction. The leading order (LO) Feynman diagrams of top quark anti-quark pair production are shown in Fig. 1.5. Pair production occurs either via quark-anti-quark annihilation (a) or gluon fusion processes (b)(c)(d). The probability of either is dictated by the initial state parton distributions which are described by PDFs evaluated at an energy scale μ^2, usually set to the top quark mass threshold m_t^2. At the LHC, the contribution to the total cross section is around 80% or 90% gluon-gluon fusion and 20% or 10% quark-anti-quark annihilation at center-of-mass-energies of $\sqrt{s} = 7$ TeV or $\sqrt{s} = 14$ TeV, respectively [12].

Recently the calculation of the $\mathrm{t\bar{t}}$ cross section reached an accuracy of next-to-next-to-leading order (NNLO) [33]. The predicted cross section for $\mathrm{t\bar{t}}$ production at $\sqrt{s} = 8$ TeV

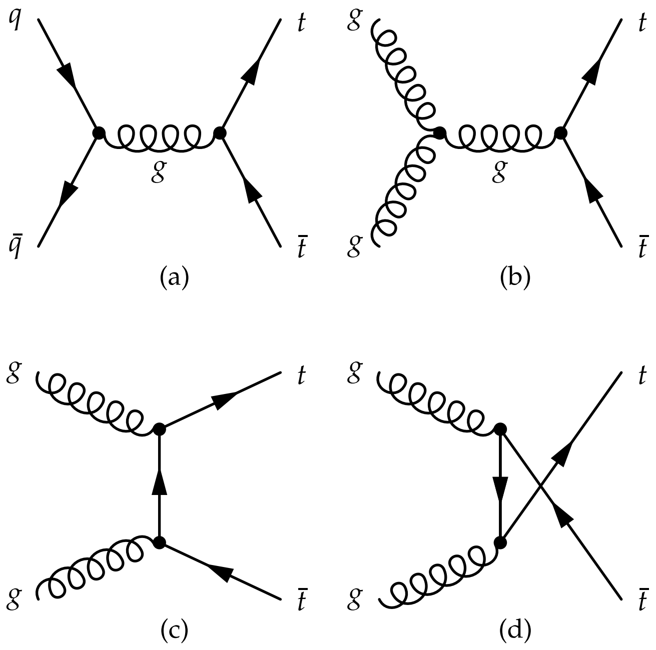

Figure 1.5.: Leading order Feynman diagrams of top quark pair production ($\mathrm{t\bar{t}}$) via light quark-anti-quark annihilation ($q\bar{q} \to \mathrm{t\bar{t}}$) (a), and gluon fusion ($gg \to \mathrm{t\bar{t}}$) (b),(c),(d).

is

$$\sigma_{t\bar{t}} = 245.8^{+6.2}_{-8.4}(\text{scale})^{+6.2}_{+6.4}(\text{PDF}), \tag{1.10}$$

assuming a top quark mass of $m_t = 173.3$ GeV and utilizing the "MSTW2008nnlo68cl" PDF [34,35].

1.3.2. Single Top Quark Production

Apart of the top-quark pair production via the strong interaction, single top quarks can be produced via the weak interaction. Single top quark production can be divided into three different mechanisms according to the virtuality of the involved W boson [36], $Q^2 = -q^2$, where q is the four momentum of the W boson. The corresponding leading order Feynman diagrams of s-channel, t-channel and associated production (tW) are depicted in Fig. 1.6. The s- and t-channel are named after the invariant quantities of the involved processes, the Mandelstam variables [37].

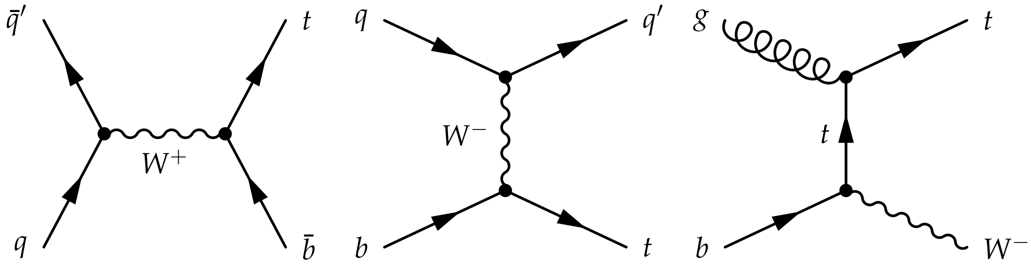

(a) s-channel (b) t-channel (c) tW

Figure 1.6.: Leading order Feynman diagrams of single top quark production in the s-channel (a), t-channel (b) and associated production (tW) (c).

Single top quark production was first observed in 2009 by the CDF [38] and DØ [39] experiments at the Tevatron. It offers a unique opportunity to study the properties of the $V - A$ structure of electroweak interaction, to analyze the properties of a bare quark, to constrain the magnitude of the CKM matrix element V_{tb}, and thus the possibility of a fourth generation, and to search for new physics.

In the following, each electroweak production mechanism will be described briefly and the corresponding predicted cross sections at different center-of-mass energies will be given.

s-channel

In s-channel production a time-like W boson is created through quark anti-quark fusion similar to Drell-Yan production of heavy vector bosons. It subsequently decays to a top quark and an anti-b quark. This production mode is strongly suppressed at the LHC since the anti-quark has to be created by gluon splitting. The LO diagram is shown in Fig. 1.7, the NLO contributions are shown in Fig. 1.8. The predicted cross sections for different center-of-mass energies are stated in Table 1.3.

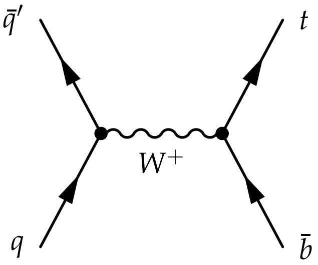

Figure 1.7.: LO Feynman diagram for single top quark s-channel production.

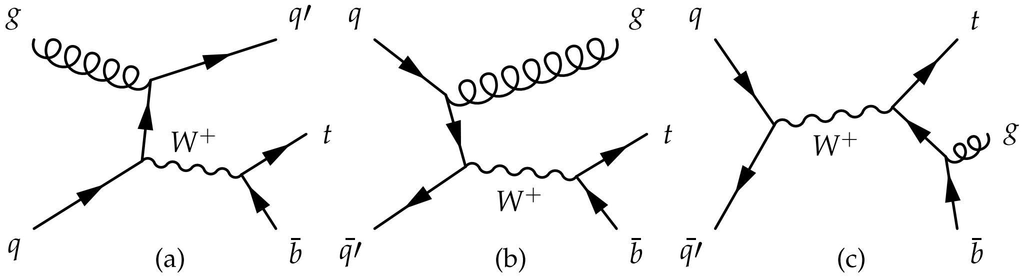

(a) (b) (c)

Figure 1.8.: NLO Feynman diagrams of single top quark production in the s-channel with initial state gluon splitting (a), gluon radiation in the initial (b) and final (c) state.

Table 1.3.: Predicted s-channel single top quark production cross sections for different center-of-mass energies relevant at the LHC. The calculations were performed at NLO+NNLL with the "MSTW2008" PDF set and a top quark mass of $m_t = 173$ GeV [40]. The quoted uncertainties include the uncertainty due to the PDF choice and due to variations in renormalization/factorization scales.

	Cross section σ [pb]		
Mode	7 TeV	8 TeV	13 TeV
top t	$3.19 \pm 0.06^{+0.13}_{-0.10}$	$3.79 \pm 0.07 \pm 0.13$	$7.20 \pm 0.13^{+0.29}_{-0.23}$
anti-top $\bar{t}$	$1.44 \pm 0.01^{+0.06}_{-0.07}$	$1.76 \pm 0.01 \pm 0.08$	$4.16 \pm 0.05^{+0.12}_{-0.23}$
combined $t + \bar{t}$	$4.63 \pm 0.07^{+0.19}_{-0.17}$	$5.55 \pm 0.08 \pm 0.21$	$11.36 \pm 0.18^{+0.40}_{-0.45}$

t-channel

The t-channel production mode is the most abundant at the Tevatron and LHC and the focus of this thesis. An incoming light quark scatters via a W boson exchange with a b quark and produces a top quark. Due to the gluon splitting needed to produce the incoming b quark an additional a anti-b quark is produced. This second or spectator b quark often has small transverse momentum p_T. Additionally the outgoing light quark q' is scattered preferably in forward region. Although suppressed by the weak interaction, it is kinematically enhanced and only a factor three smaller than $\mathrm{t\bar{t}}$ production. This is due to the fact that it scales with the W boson mass $1/M_W^2$ instead of $1/\hat{s}$ like in $\mathrm{t\bar{t}}$ or *s*-channel production. The $2 \rightarrow 2$ and $2 \rightarrow 3$ production diagrams are shown in Fig. 1.9. The $2 \rightarrow 3$ process is also known as W-gluon fusion. The NLO contributions to the $2 \rightarrow 2$ process are shown in Fig. 1.10. Comparing these to the *s*-channel NLO contributions in Fig. 1.8 one finds the same initial and final states, $gq \rightarrow q't\bar{b}$, which would lead to interference and make them not separable. However, due to the Wtb vertex in the *s*-channel diagram, the b quark and the top quark are created as color singlet since they stem from the W boson decay, whereas in the *t*-channel diagram they are created as color octect due to the color connection with the initial gluon. Therefore no interference occurs and the processes are separable.

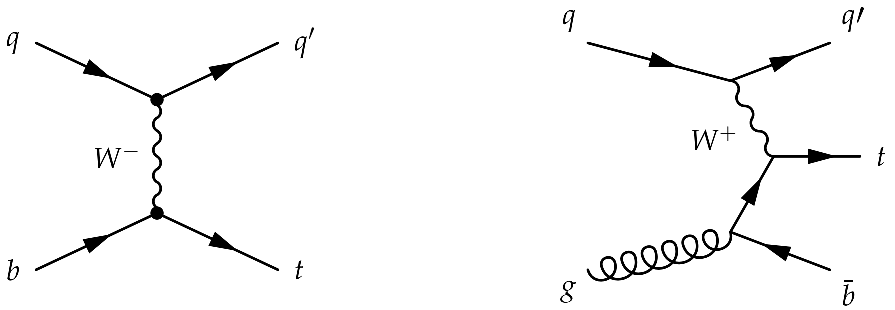

Figure 1.9.: Feynman diagram for single top quark *t*-channel production. Depicted is the $2 \rightarrow 2$ (left) and $2 \rightarrow 3$ (right) process where the second b quark originates from gluon splitting.

The predicted *t*-channel single top quark cross sections for pp collisions at different center-of-mass energies, given in Table 1.4, have been calculated for a top quark mass of 172.5 GeV at NLO in QCD with HATHOR v2.1 [41, 42]. The PDF and α_S uncertainties were calculated using the PDF4LHC prescription [43] with the MSTW2008 68% CL NLO [44, 45], CT10 NLO [30] and NNPDF2.3 [46] PDF sets, added in quadrature to the scale uncertainty.

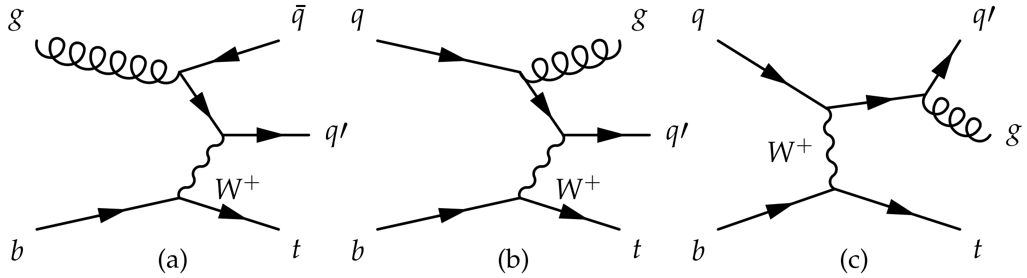

Figure 1.10.: NLO Feynman diagrams of single top quark production in the *t*-channel with initial state gluon splitting (a), gluon radiation in the initial (b) and final (c) state.

Recently, a first calculation at NNLO for the *t*-channel cross section was published [48].

Table 1.4.: Predicted single top quark t-channel production cross sections for different center-of-mass energies relevant at the LHC. The calculations were performed at NLO with Hathor v2.1 according to the "TopLHCWG" recommendations [47]. The given systematic uncertainties include renormalization and factorization scale uncertainties and combined PDF and α_S uncertainties.

	Cross section σ [pb]		
Mode	7 TeV	8 TeV	13 TeV
top t	$41.80^{+1.78}_{-1.52}$	$54.87^{+2.29}_{-1.94}$	$136.02^{+5.40}_{-4.57}$
anti-top $\bar{t}$	$22.02^{+1.27}_{-1.16}$	$29.74^{+1.67}_{-1.51}$	$80.95^{+4.06}_{-3.61}$
combined $t+\bar{t}$	$63.89^{+2.91}_{-2.52}$	$84.69^{+3.76}_{-3.23}$	$216.99^{+9.04}_{-7.71}$

The NNLO corrections are rather small, on the order of a few percent.

Associated tW production

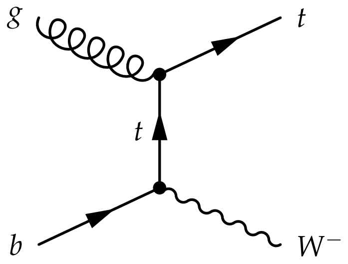

Figure 1.11.: Feynman diagram for associated single top quark production (tW).

In associated production (tW) the top quark is produced in association with a real or close to real W boson. This channel is the second most important channel at the LHC. One leading order Feynman diagram is shown in Fig. 1.11. Associated production was for the first time detected in 2012 at the LHC by the CMS experiment [49]. The predicted cross sections for associated production are given in Table 1.5.

The NLO Feynman diagrams for associated production are shown in Fig. 1.12. The final states of these NLO contributions are the same as in LO $t\bar{t}$ production which leads to interference and makes it hard to separate these two processes and define associated production as an independent process. The interference is largest in the phase space where the top quarks are close to the mass shell. The interference effect and suitable cuts to define tW as an independent process have been studied in Ref. [50]. There are two methods available to handle the interference terms in simulation, diagram removal and diagram subtraction. In the diagram removal method all diagrams in Fig. 1.12 are removed from the NLO cross section calculation, the diagram subtraction method introduces a subtraction term to cancel the contributions from $t\bar{t}$. Within the scale variations both methods lead to the same event rate and kinematic distributions.

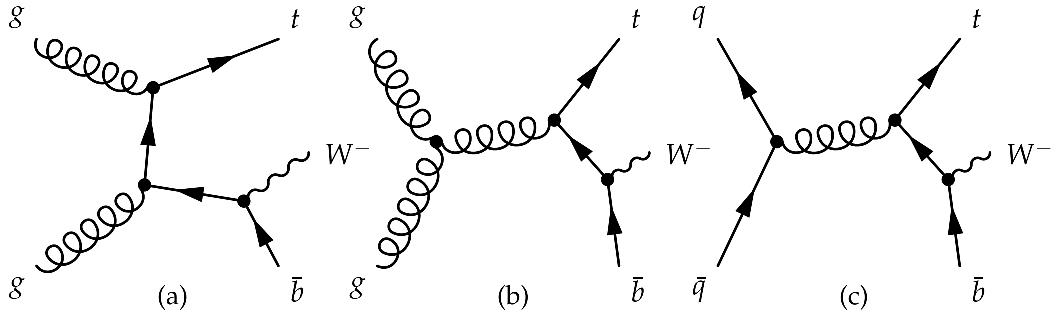

Figure 1.12.: NLO Feynman diagrams of associated single top quark production (tW).

Table 1.5.: Predicted associated (tW) single top quark production cross sections for different center-of-mass energies relevant at the LHC. The calculations were performed at NLO+NNLL with the "MSTW2008" PDF set and a top mass of $m_t = 173$ GeV [40]. The cross sections for tW$^+$ are identical to those of tW$^-$. The quoted uncertainties include the uncertainty due to the PDF choice and due to variations in renormalization/factorization scales.

	Cross section σ [pb]		
Mode	7 TeV	8 TeV	13 TeV
top t, anti-top $\bar{t}$	$7.87 \pm 0.20^{+0.55}_{-0.57}$	$11.1 \pm 0.3 \pm 0.7$	$35.6 \pm 0.9 \pm 1.7$
combined $t + \bar{t}$	$15.74 \pm 0.40^{+1.10}_{-1.14}$	$22.2 \pm 0.6 \pm 1.4$	$71.2 \pm 1.8 \pm 3.4$

New Physics in Single Top Quark Production

New physics like a potential fourth generation, vector-like quarks or anomalous top quark couplings can be detected in single top quark production.

Vector-like quarks will either show up as resonances in mass spectra or through a value of $|V_{tb}|$ different from one [51]. A fourth generation is ruled out by measurements of the CKM matrix elements, see Section 2.2, and constraints from the mass of the discovered Higgs boson [52, 53]. If there are anomalous top quark couplings, they will show up in the spin asymmetry of the top quark decay, see Section 2.4.

1.4. Top Quark Properties

1.4.1. Top Quark Mass

With a mass of 173.34 ± 0.27 (stat.) $\pm\, 0.71$ (syst.) GeV [14] the top quark is the heaviest known elementary particle. Since the top quark mass is close to the vacuum expectation value, $m_t \approx v/\sqrt{2}$, the Yukawa coupling to the Higgs boson is close to one, $\lambda_t \approx 1$. Since the mass of the top quark appears in calculations linked to the stability of the electroweak vacuum if one assumes validity of the SM up to the Planck scale, its precise value is deemed of high interest to the fate of the universe [54]. The current measurements of the Higgs boson and top quark mass and their uncertainties point to a meta stable vacuum.

1.4.2. Top Quark Decay

The top quark preferably decays to a b quark and a W boson, $t \to Wb$, due to the large value of $V_{tb} \approx 1$, see Eq. (1.8). Decays to charm or strange quarks are strongly suppressed. Neglecting higher-order electroweak corrections and quadratic terms, the width of the top quark in the SM at NLO is predicted as [55]:

$$\Gamma_t = \frac{G_F m_t^3}{8\pi\sqrt{2}} \left(1 - \frac{M_W^2}{m_t^2}\right) \left(1 + 2\frac{M_W^2}{m_t^2}\right) \left[1 - \frac{2\alpha_s}{3\pi}\left(\frac{2\pi^2}{3} - \frac{5}{2}\right)\right] , \tag{1.11}$$

where m_t is the top quark pole mass. The width for a top-quark mass of 173.3 GeV, assuming $\alpha_S(M_Z) = 0.118$), is

$$\Gamma_t \approx 1.35\,\mathrm{GeV} \tag{1.12}$$

which increases with larger masses. The large mass of the top quark leads to a very short lifetime of

$$\tau_{had} \propto \frac{1}{\Lambda_{QCD}} \approx 5 \cdot 10^{-24}\,\mathrm{s}\,. \tag{1.13}$$

Therefore the top quark decays before it can form top-flavored hadrons or $\mathrm{t\bar{t}}$-quarkonium bound states.

The combination of the top quark branching ratios from $\mathrm{t\bar{t}}$ measurements and the direct measurement of $|V_{tb}|$ in the single top-quark t-channel allows to measure the decay width of the top quark.

If one assumes that top quarks only decay to b quarks then the branching ratio is $\sum_q \mathcal{B}(t \to Wq) = 1$ and the decay ratio is $\mathcal{R} = \mathcal{B}(t \to Wb)$ and the top-quark decay width can be written as:

$$\Gamma_t = \frac{\sigma_{t-ch.}}{\mathcal{B}(t \to Wb)} \cdot \frac{\Gamma(t \to Wb)}{\sigma_{t-ch.}^{theor.}} , \tag{1.14}$$

where $\sigma_{t-ch.}$ ($\sigma_{t-ch.}^{theor.}$) is the measured (theoretical) t-channel single top-quark cross section and $\Gamma(t \to Wb)$ is the partial decay width to Wb. A recent measurement is described in Section 2.3. The subsequent decays of the W boson decay are listed in Table 1.6. It decays predominantly to pairs of quarks ($u\bar{d}, c\bar{s}$) or charged leptons and neutrinos. Whereas the τ lepton can further decay hadronically or to either an electron or muon and the corresponding neutrino.

In general W bosons from top quark decays can be produced with left-handed, right-handed or with longitudinal polarization. In the SM the helicity of the W boson from top quark decay has mostly longitudinal polarization or is left-handed. The NNLO

Table 1.6.: Decay modes of the W^+ boson [12].

Decay mode	Fraction (Γ_i/Γ)
Hadrons	67.41 ± 0.27
$\ell^+\nu$	10.86 ± 0.09
$e^+\nu$	10.71 ± 0.16
$\mu^+\nu$	10.63 ± 0.15
$\tau^+\nu$	11.83 ± 0.21

predictions for the W helicity fractions, with a top quark mass of $m_t = 172.8 \pm 1.3\,\text{GeV}$ and a b quark mass of $m_b = 4.8\,\text{GeV}$, are $F_L = 0.311 \pm 0.005$, $F_0 = 0.687 \pm 0.005$, and $F_R = 0.0017 \pm 0.0001$ [56], where F_L, F_R and F_0 are the left-handed, right-handed or longitudinally polarized fractions, respectively.

1.4.3. Top Quark Spin Polarization

Single top quark production offers a unique opportunity to study bare quarks since the top quark decays before it can hadronize and spin information is conserved, in contrast to $t\bar{t}$ production where only correlations can be measured.

The angular distribution (θ_X) of the decay product X (W, ℓ, ν, b) in the top-quark rest frame is

$$\frac{1}{\Gamma}\frac{d\Gamma}{d\cos\theta_X} = \frac{\Gamma}{2}(1 + P_t\alpha_x\cos\theta_X) = \frac{\Gamma}{2}(1 + A_X\cos\theta_X)\,, \tag{1.15}$$

where P_t is the polarization of the top quark (production vertex) along a given direction and α_X is the spin-analyzing power of the decay particle. Both parameters can be combined into a spin asymmetry A_X and can be affected by anomalous top quark couplings [57]. The spin analyzing power α_X describes the correlation between the decay products and the top quark. The different possible spin analyzing powers are depicted in Fig. 1.13, the lepton has the maximum spin analyzing power [57,58].

Several possible angles and bases are suitable to study spin polarization. In the analysis described in this thesis, the angle between the charged lepton from the top quark decay and the spectator basis of the second b quark measured in the top-quark rest frame is used.

A recent measurement of the top quark polarization in single top quark production is presented in Section 2.4.

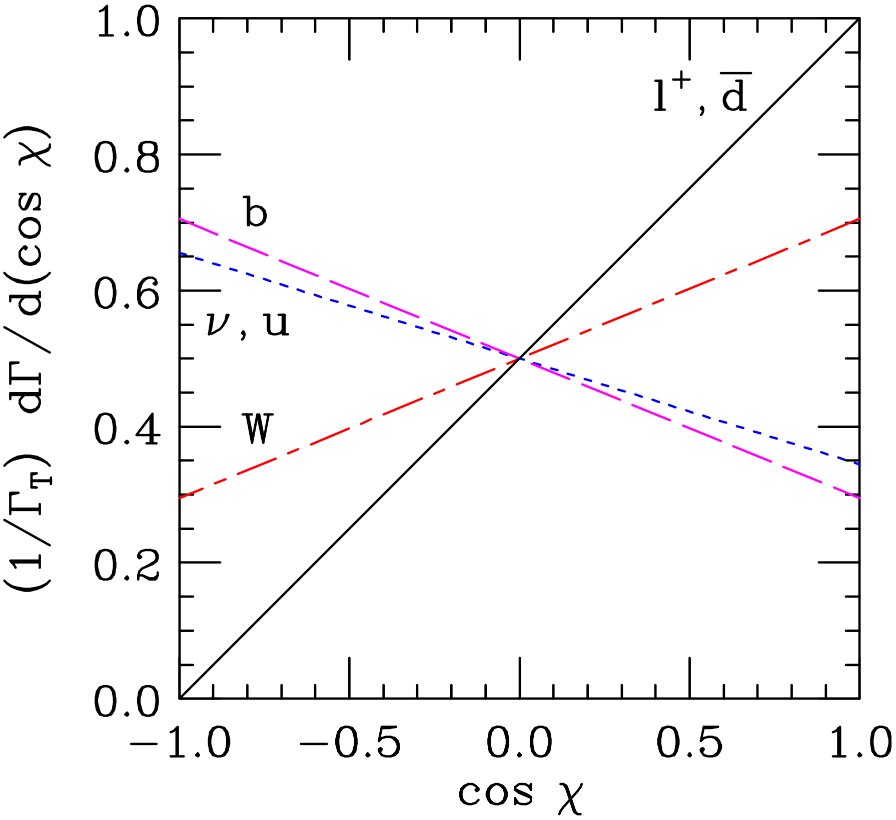

Figure 1.13.: Spin analyzing powers of top quark decay products [59]. The spin analyzing power describes the correlation between the decay product and the parent top quark. In this figure, the previously defined angle between the top quark and the decay product, $\cos\theta$, is called $\cos\chi$. The charged lepton (besides the down type quark) has the largest spin analyzing power of $\alpha_\ell \approx 1$.

2. Experimental Status of Single Top Quark Production

Since the discovery of single top quark production at the Tevatron in 2009 it only took two years for the first evidence to show up at the LHC [60, 61]. Nowadays the LHC produced a plethora of top quarks which enabled a detailed study of its properties.

In this chapter, several measurements of top quark properties in single top quark production performed by the CMS Collaboration are presented. Contributions to these results made as part of this thesis will be mentioned explicitly.

2.1. Cross Section Measurements

The single top quark production cross section in the t-channel has been measured at 7 and 8 TeV by the CMS Collaboration. The measurement at 7 TeV utilized a dataset of 1.17 fb^{-1} and 1.56 fb^{-1} in the electron and muon channel, respectively [62]. The measurement at $\sqrt{s} = 8$ TeV was performed with 19.7 fb^{-1} of data [63].

2.1.1. 7 TeV Measurement

For the 7 TeV measurement three different analyses were combined. Two of them used complementary multivariate analysis (MVA) techniques.

The first approach exploits that the light quark jet in single top quark t-channel events is preferably in the forward region and employs a robust fit to the distribution of the pseudorapidity of this jet, η_{lj}, shown in Fig. 2.1. The W+jets background is estimated in a data-driven way. The two MVAs exploit multiple input variables and define several different signal and background enriched regions. The different regions are defined according to the jet multiplicity and number of b-tagged jets and are used to constrain systematic uncertainties and get a handle on the background modeling. The employed techniques use a Boosted Decision Tree (BDT) and a neural network (NN) to combine several input variables and separate signal and background which are estimated by performing a fit on the discriminators in the different regions simultaneously. The NN analysis [64] has been developed as part of this thesis based on a first feasibility study [65]. The discriminator outputs for the neural network analysis in the muon channel are shown in Fig. 2.2. In all these analyses the QCD multijet background is estimated in a data-driven way in a sideband region defined by inverting the relative isolation and the $m_{\mathrm{T,W}}$ or $\not{E}_{\mathrm{T}}$ cuts. The η_{lj} fit analysis uses a maximum likelihood fit to estimate the signal and background fraction. Both of the MVAs utilize a Bayesian method.

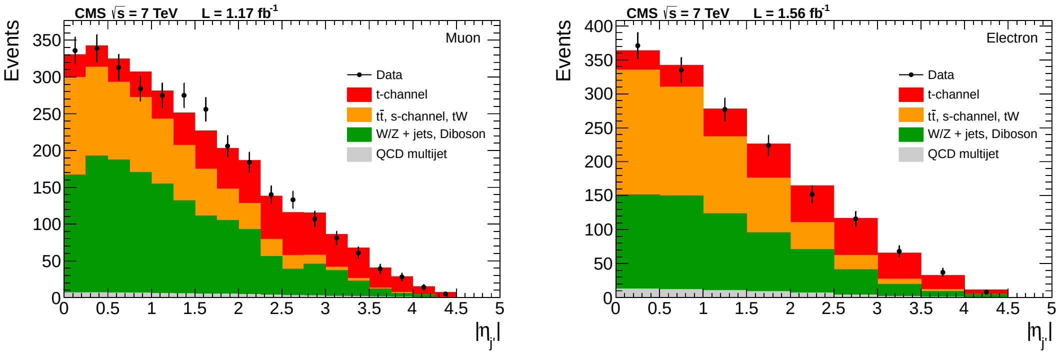

Figure 2.1.: Pseudorapidity of the light quark jet η_{lj} in the 7 TeV measurement. Result of a simultaneous fit to the pseudorapidity of the light quark jet η_{lj} in the muon (left) and electron (right) decay channels.

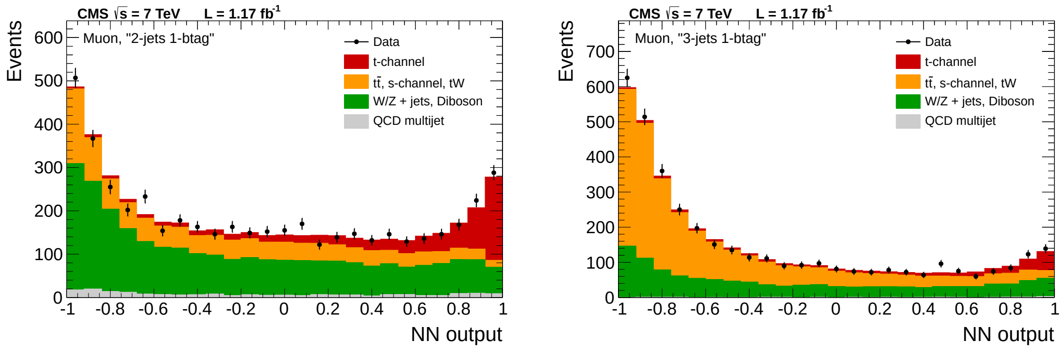

Figure 2.2.: Distributions of the NN discriminator output in the muon channel for the "2-jets 1-btag" (left) and "3-jets 1-btag" (right) categories. Simulated signal and background contributions are scaled to the best fit results.

The result of all three analyses is combined using the BLUE method [66], described in Appendix A.1. The combined result of the measured single-top-quark t-channel production cross section at $\sqrt{s} = 7$ TeV is

$$\sigma_{\mathrm{t-ch.}} = 67.2 \pm 3.7\,(\mathrm{stat.}) \pm 3.0\,(\mathrm{syst.}) \pm 3.5\,(\mathrm{theor.}) \pm 1.5\,(\mathrm{lum.})\ \mathrm{pb} = 67.2 \pm 6.1\ \mathrm{pb}\,. \tag{2.1}$$

2.1.2. 8 TeV Measurement

The 8 TeV measurement uses the same method as one of the 7 TeV measurements, a robust fit to the pseudorapidity η_{lj} of the light quark jet, shown in Fig. 2.3. The main backgrounds were estimated with data-driven techniques.

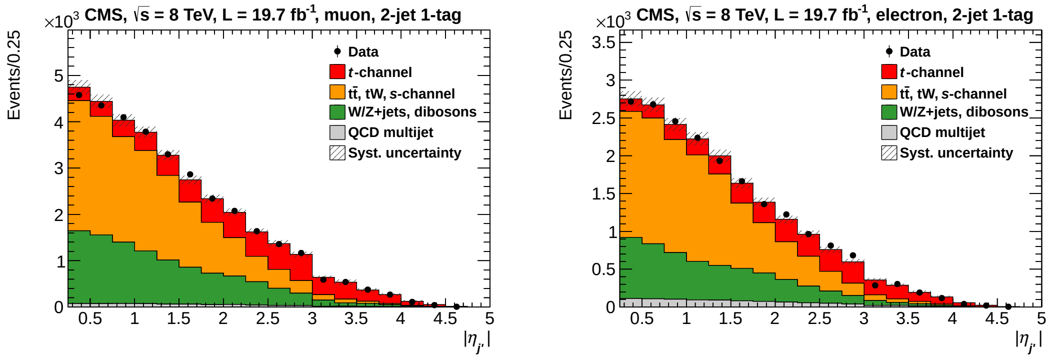

Figure 2.3.: Pseudorapidity of the light quark jet η_{lj} in the 8 TeV measurement. Fitted $|\eta_{lj}|$ distributions for muon (left) and electron (right) decay channels, normalized to the yields obtained from the combined total cross section fit. Systematic uncertainty bands include the shape uncertainties on the distributions.

The inclusive cross section was measured to be

$$\sigma_{\mathrm{t-ch.}} = 83.6 \pm 2.3(\mathrm{stat.}) \pm 7.4(\mathrm{syst.})\ \mathrm{pb}\,. \tag{2.2}$$

The measured inclusive cross sections agree very well with theoretical predictions [67, 68], as shown in Fig. 2.4.

The single t and $\bar{t}$ cross sections were measured to be

$$\sigma_{\mathrm{t-ch.}}(t) = 53.8 \pm 1.5(\mathrm{stat.}) \pm 4.4(\mathrm{syst.})\mathrm{pb}\,, \tag{2.3}$$

$$\sigma_{\mathrm{t-ch.}}(\bar{t}) = 27.6 \pm 1.3(\mathrm{stat.}) \pm 3.7(\mathrm{syst.})\mathrm{pb}\,. \tag{2.4}$$

The ratio of the top quark and anti-top quark cross sections was measured to be

$$R_{t-ch.} = \sigma_{\mathrm{t-ch.}}(t)/\sigma_{\mathrm{t-ch.}}(\bar{t}) = 1.95 \pm 0.10(\mathrm{stat.}) \pm 0.19(\mathrm{syst.})\,. \tag{2.5}$$

This ratio $R_{t-ch.}$ is thus sensitive to the PDF of the up and down quarks involved in the hard scattering process and can be used to constrain these contributions in a PDF fit if smaller uncertainties can be achieved. The measured charge ratio is compared with predictions made as part of this thesis with the most commonly used PDF sets, shown in Fig. 2.5. Currently all compared PDF sets agree within the estimated uncertainties.

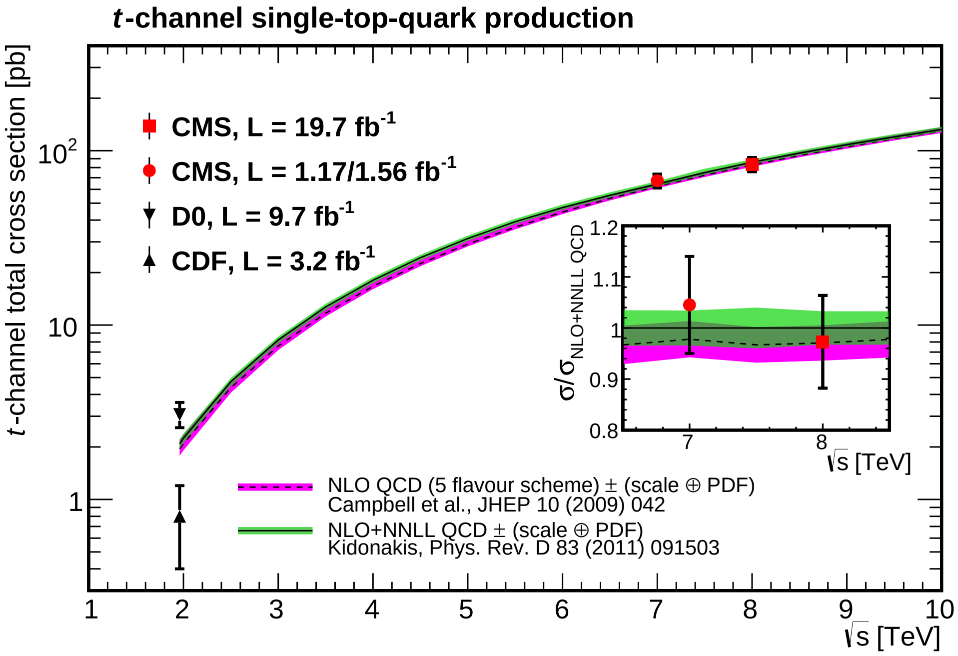

Figure 2.4.: Single top quark production cross sections vs. center-of-mass energy. The measured data agree well with theoretical predictions [67, 68].

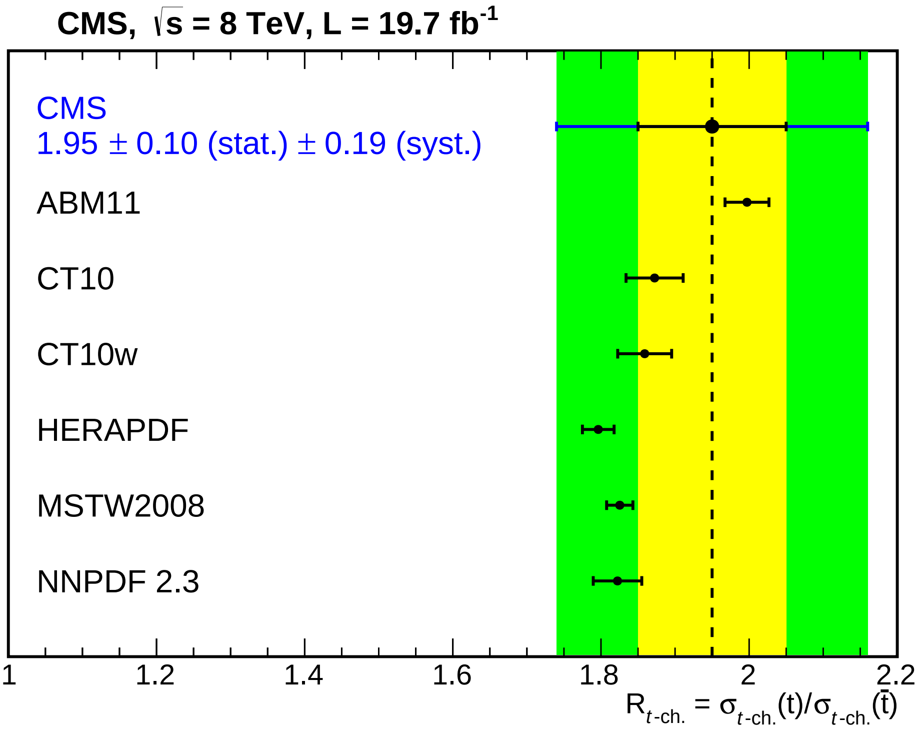

Figure 2.5.: Measured charge ratio compared to predictions calculated with different PDF sets. The measurement is compatible with all predictions within the statistical (yellow) and systematic uncertainty. The total uncertainty (statistical+systematic) is shown as a green band.

2.2. Determination of the CKM Matrix Element $|V_{tb}|$

The appearance of the Wtb vertex in single top quark production allows a direct measurement of the CKM matrix element V_{tb}, without being restricted to three generations like $\mathrm{t\bar{t}}$ measurements. Potential anomalous couplings can introduce anomalous form factors [69–71], which can be parametrized as f_{L_V} where L_V refers to the left-handedness of the coupling that would modify the interaction. Current measurements indicate that one can assume $|V_{td}|, |V_{ts}| \ll |V_{tb}|$, i.e. the branching ratio of $t \to Wb$ is almost one, and obtains $|f_{L_V} V_{tb}| = \sqrt{\sigma_{t-ch.}/\sigma^{theo.}_{t-ch.}}$. Several BSM scenarios predict a value of f_{L_V} different than one but only a mild modification of the branching ratio $\mathcal{B}$ [51].

The most stringent measurement [63], a combination of the $\sqrt{s} = 7$ TeV [62] and $\sqrt{s} = 8$ TeV [63] measurements of the CMS experiment, of $|V_{tb}|$ is

$$|V_{tb}| = 0.998 \pm 0.038(\text{exp.}) \pm 0.016(\text{theo.})\,. \tag{2.6}$$

Setting f_{L_V} to 1 and constraining $|V_{tb}|$ to the interval $[0, 1]$ by employing a unified Feldman-Cousins approach [72] yields a confidence interval of

$$0.92 < |V_{tb}| \leq 1 \quad \text{at 95\% C.L.}\,. \tag{2.7}$$

This measurement combined with constraints from recent Higgs boson measurements diminishes the possibility of a fourth generation [52, 53].

2.3. Top Quark Width

The total top quark decay width Γ_t can be extracted from the partial decay width, $\Gamma(t \to Wb)$, measured in single top quark t-channel production and the branching ratio $\mathcal{B}(t \to Wb)$ measured in dileptonic $\mathrm{t\bar{t}}$ events.

The branching ratio of the top quark decay to b quarks is defined as

$$\mathcal{R} = \mathcal{B}(t \to Wb)/\mathcal{B}(t \to Wq)\,. \tag{2.8}$$

By counting the number of b jets per event in the $\mathrm{t\bar{t}}$ dilepton channel an unconstrained value of

$$\mathcal{R} = 1.014 \pm 0.003(\text{stat.}) \pm 0.032(\text{syst.}) \tag{2.9}$$

is measured at $\sqrt{s} = 8$ TeV by the CMS collaboration.

Assuming the SM case with three generations and $|V_{tb}| = 1$ one can write the branching ratio as $\mathcal{R} = |V_{tb}|^2$. Further assuming $\sum_q \mathcal{B}(t \to Wq) = 1$, the branching ratio of top quark decays to W bosons and b quarks reduces to $\mathcal{R} = \mathcal{B}(t \to Wb)$ and the total top quark decay width can be written as

$$\Gamma_t = \frac{\sigma_{t-ch.}}{\mathcal{B}(t \to Wb)}\,. \tag{2.10}$$

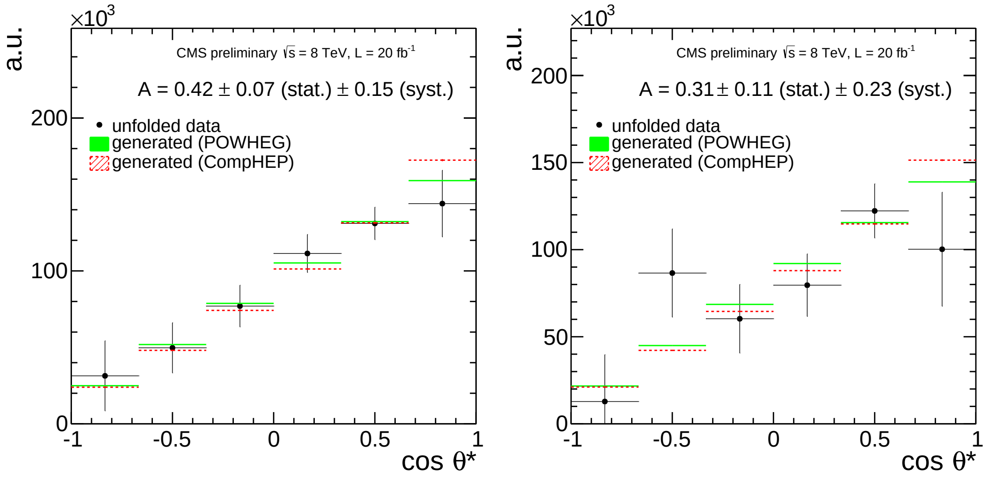

(a)

(b)

Figure 2.6.: Unfolded distributions of $\cos\theta_l^*$ in the muon (a) and electron (a) channel.

The most recent measurement by the DØ collaboration yields $\Gamma_t = 2.00^{+0.47}_{-0.43}$ GeV with an uncertainty of 24% [73].
The combination performed by the CMS collaboration [74] of the top quark decay ratio and t-channel cross section measurement at $\sqrt{s} = 7$ TeV [62], presented earlier in this thesis, yields a total width of

$$\Gamma_t = 1.36 \pm 0.02(\text{stat.})^{+0.14}_{-0.11}(\text{syst.})\text{GeV}, \tag{2.11}$$

which is in good agreement with the SM prediction given in Eq. (1.12).

2.4. Top Quark Polarization

A first measurement of the top quark polarization in single top quark events was attempted by the CDF collaboration [75]. However, the available amount of data was not enough and the precision of the measurement was not sufficient to exclude the hypothesis of unpolarized or oppositely polarized top quarks. In the following, a first measurement of the top quark polarization by the CMS experiment will be described. A detailed description of this analysis can be found in Ref. [76]. The measured quantity is the difference between forward and backward going leptons in the rest frame of the top quark after unfolding

$$A_\ell = \frac{1}{2} \cdot P_t \cdot \alpha_\ell = \frac{N(\uparrow) - N(\downarrow)}{N(\uparrow) + N(\downarrow)}, \tag{2.12}$$

where P_t is the top quark polarization to be measured, α_ℓ is the spin analyzing power of charged leptons. $N(\uparrow)$ and $N(\downarrow)$ are the number of charged leptons aligned or counter aligned with the direction of the light quark recoiling against the top quark in the top quark rest frame. The analysis is based on 19.7 fb^{-1} of data taken at a center-of-mass energy of $\sqrt{s} = 8$ TeV. Events with top quark decays $t \to bW \to b\ell\nu$ are selected, where ℓ is either a muon or electron. The signal MC sample is simulated with the NLO generator POWHEG [77–79] interfaced to PYTHIA 6.4 [80] for the parton shower. The decays of τ leptons are modeled with TAUOLA [81]. The generator COMPHEP [82] is used as an alternative to estimate the dependence on the signal modeling with approximative full NLO properties [83].

Signal events are required to have exactly one isolated lepton and missing transverse energy ($\not{E}_{\mathrm{T}}$), stemming from the leptonic W boson decay, one central b jet from the top quark decay and an additional light quark jet from the hard scattering process, preferably produced in the forward region. The spectator b jet is often not detected due to its soft p_{T} spectrum. The analysis uses an event selection similar to the $\sqrt{s} = 7$ TeV cross section measurement in the same channel [62].

In order to further reduce the amount of background contributions and obtain a signal enriched region a Boosted Decision Tree (BDT) is trained and a cut on the discriminator is applied. The BDT is trained for each lepton channel separately with 9 input variables. The BDT discriminator outputs, including a zoom into the signal enriched region and the distribution of $\cos\theta_l^*$ in this region, are shown in Fig. 2.7.

After the number of background events has been estimated with a likelihood fit to the BDT discriminator and subtracted from data, the signal enriched sample has to be corrected for detector resolution and selection efficiency effects. This unfolding is performed with a smearing matrix obtained from simulated events and a generalized matrix inversion method based on the TUNFOLD package [84] which has been implemented as part of this thesis. The unfolding procedure is explained in detail in Chapter 7. The unfolded distributions yield asymmetries of

$$A_\ell^\mu = 0.42 \pm 0.07(\text{stat.}) \pm 0.15(\text{syst.})\,, \tag{2.13}$$
$$A_\ell^e = 0.31 \pm 0.11(\text{stat.}) \pm 0.23(\text{syst.})\,. \tag{2.14}$$

which are in good agreement with the standard model prediction of 0.5. A combination of both lepton channels with the BLUE method [1] yields

$$A_\ell = 0.41 \pm 0.06(\text{stat.}) \pm 0.16(\text{syst.})\,. \tag{2.15}$$

All systematic uncertainties except the lepton efficiencies and QCD modeling, which are assumed to be uncorrelated, are considered as 100% correlated across both channels, including the signal and background normalizations from the fit to the BDT discriminator output. With a BLUE coefficient [85] of 96% the combination is strongly dominated by the muon channel.

Under the assumption that the spin analyzing power of a charged lepton is 100% the resulting top quark polarization is

$$P_t = 0.82 \pm 0.12(\text{stat.}) \pm 0.32(\text{syst.})\,. \tag{2.16}$$

---

[1] See Appendix A.1 for more details on the BLUE method and utilized implementation.

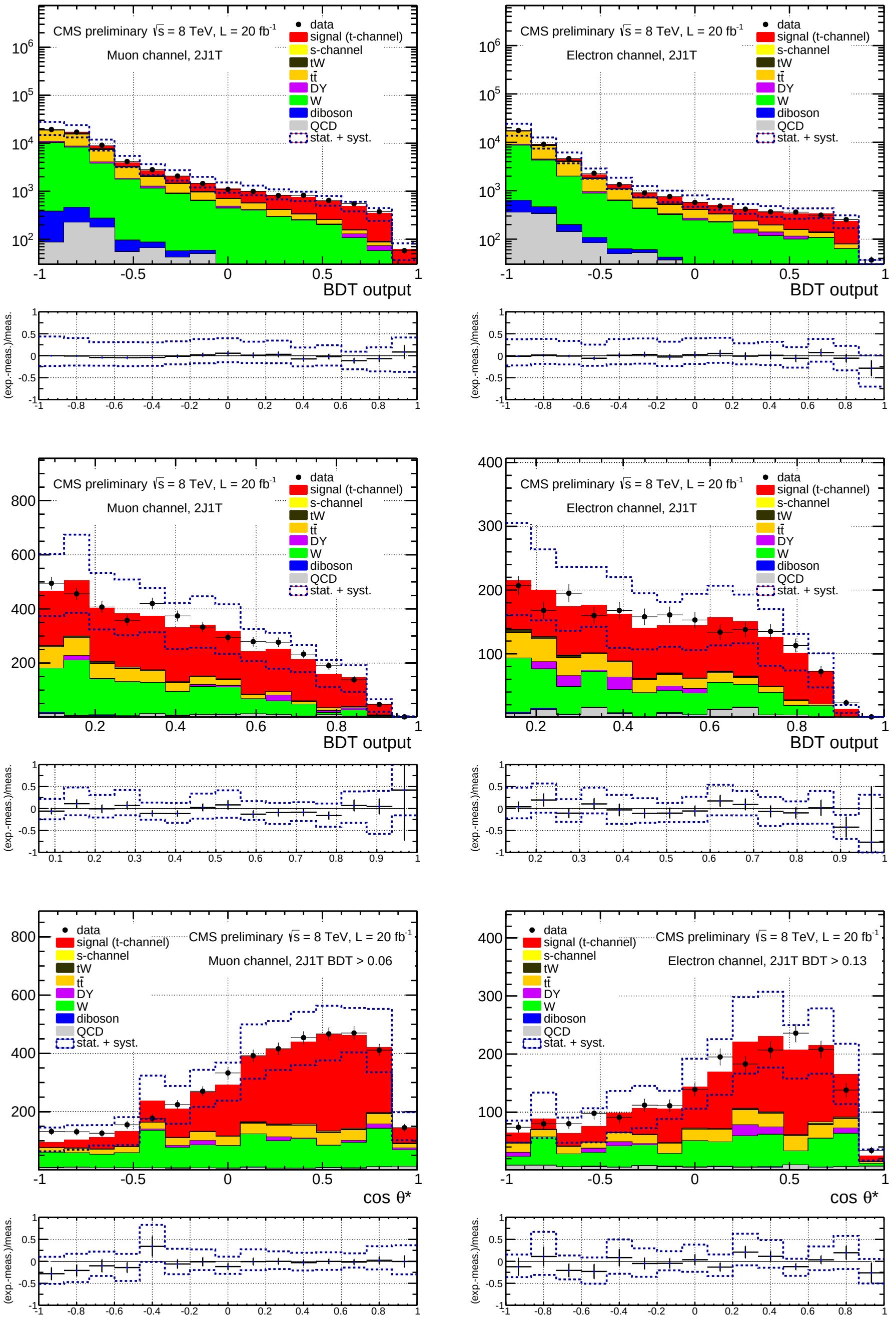

Figure 2.7.: Top row: BDT discriminator output in the muon (left) and electron (right) channel. Middle row: Enriched signal region zoom. Bottom row: $\cos\theta_l^*$ distribution in the signal enriched region. All processes are normalized to the outcome of the maximum likelihood fit. The depicted uncertainties on the MC templates, dashed lines, include statistical and systematic uncertainties.

This result is in good agreement with the standard model prediction of $P_t \approx 1$.

3. The Large Hadron Collider and CMS Detector

Matter on earth consists mostly of particles of the first generation in form of quarks, bound in protons and neutrons, which together with electrons form atoms. Cosmic radiation which is constantly hitting the atmosphere creates particle showers with many decay products also from other generations. In order to study particles of the second and third generation in detail these particles have to be created through accelerators and colliders. Through the infamous relation between energy and mass, $E = mc^2$, it is possible that particles can be created by providing collisions with large enough energy. The energy has to be at least as large as the mass of the newly created particle. The number of particles produced by a collider depends on the interaction rate $\dot{N}$ of a process.

This chapter will describe the experimental setup employed for this thesis consisting of the Large Hadron Collider, described in Section 3.1, and the CMS detector, described in Section 3.2.

3.1. The Large Hadron Collider

The Large Hadron Collider (LHC) is the world's largest and most powerful particle collider. It was built from 1998 to 2008 in the already existing 26.7 km long tunnel of the Large Electron-Positron (LEP) collider. The tunnel is located between 45 and 170 m underground near Geneva and has an internal diameter of 3.7 m. Due to its small size the two required beam pipes needed to be combined into one common cryostat. The design luminosity of the LHC is $10^{34}\text{cm}^{-2}s^{-1}$ with a center-of-mass energy of $\sqrt{s} = 14$ TeV. The LHC can also collide heavy ions (Pb) with an energy of 2.8 TeV per nucleon and a peak luminosity of $10^{27}\text{cm}^{-2}s^{-1}$.

An overview of the LHC complex is shown in Fig. 3.1. The ring of the LHC is not a perfect circle but an octant structure with eight arcs and eight straight sections, each with an access point labeled from 1 to 8. Experiments and utility services are installed along these eight points. All in all, seven experiments are installed along the LHC tunnel. The largest are the two general purpose detectors, ATLAS [87] and CMS [88]. Besides that, two special purpose detectors LHCb [89] and ALICE [90] study b quark physics and QCD in heavy ion collisions, respectively. Three smaller detectors have special purposes and focus on the total cross section, forward physics and the search for monopoles. The data in this thesis was recorded with the CMS detector, which will be described in the following Section 3.2.

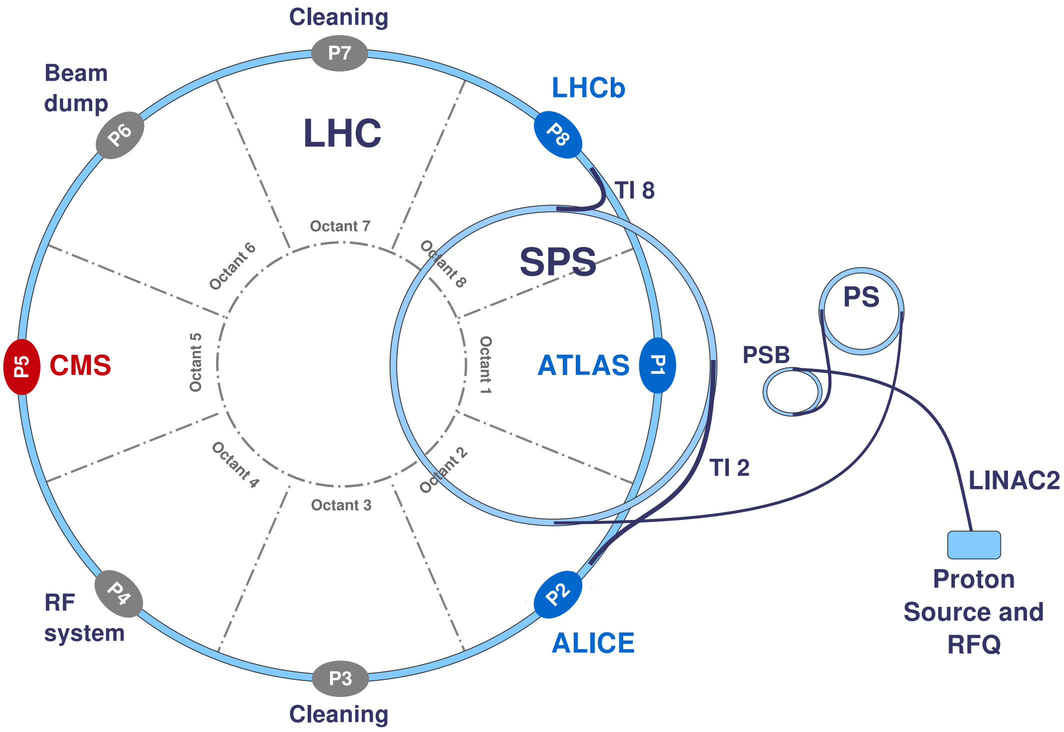

Figure 3.1.: Schematic layout of the LHC and CERN accelerator complex [86]. The accelerator chain for the protons released from the source consists of the Radio Frequency Quadrupole (RFQ), the linear accelerator LINAC2, the Proton Synchrotron (PS), the Proton Synchrotron Booster (PSB), and the Super Proton Synchrotron (SPS). After the SPS, the proton bunches are injected as two counter-rotating beams in the LHC via the transfer lines TI 2 and TI 8. The LHC is depicted with the superimposed octant structure of eight arcs and eight straight sections used for utility services or experiments. Two sections are used for cleaning the beams, one for the beam dump system and one for the RF systems. The two general purpose detectors, ATLAS and CMS, are located at P1 and P5, the special purpose detectors LHCb and ALICE are located at P8 and P2, respectively.

Before protons can be accelerated in the main LHC ring they have to pass a complex chain of accelerators [91]. All protons are produced by the ionization of hydrogen gas with high energy electrons from a pulsed duoplasmatron. The protons are extracted from the plasmatron by applying a voltage of 90 kV and send to a radio frequency quadrupole (RFQ). The RFQ accelerates the beam of protons to 750 keV while focusing and dividing the beam into separate bunches. These bunches are accelerated to 50 MeV by the linear accelerator LINAC2. After that the proton bunches are further accelerated by the Proton Synchrotron Booster (PSB) and the Proton Synchrotron (PS) to 1.4 GeV and 25 GeV respectively. The last station before the LHC main ring is the Super Proton

Synchrotron (SPS). This 6.9 km long synchrotron increases the beam energy to 450 GeV. Finally, the beam is split up and injected via the two transfer lines as counter-rotating beams into the LHC main ring.

The proton beams are accelerated in two beam pipes surrounded by one common cryostat. The beams are kept on track by 1232 superconducting dipole magnets, 392 quadrupole magnets are used to focus the beams. The magnets are arranged according to the focusing-defocusing (FODO) principle. The Niobium-Titanium (NbTi) magnets have a maximum field strength of 8.33 Tesla at the design beam energy of 7 TeV and are cooled down to a temperature of 1.9 K through superfluid helium. Cooling down helium below temperatures of 2.2 K has the benefit that it is superfluid and can flow without friction. The large thermal conductivity of superfluid helium allows efficient cooling of the LHC.

The number of events $\dot{N}$ generated in the LHC collisions per second is given by

$$\dot{N} = L\sigma\,, \tag{3.1}$$

where L is is the instantaneous luminosity and σ is the cross section for the investigated process. The luminosity for two colliding bunches a and b consisting of N_a and N_b particles is

$$L = f \cdot \frac{N_a N_b}{4\pi\sigma_x\sigma_y}\,, \tag{3.2}$$

were f is the collision frequency and σ_x and σ_y are the transverse sizes of the Gauss shaped bunches [12]. The total integrated luminosity per day provided by the LHC and recorded by the CMS experiment is shown in Fig. 3.2.

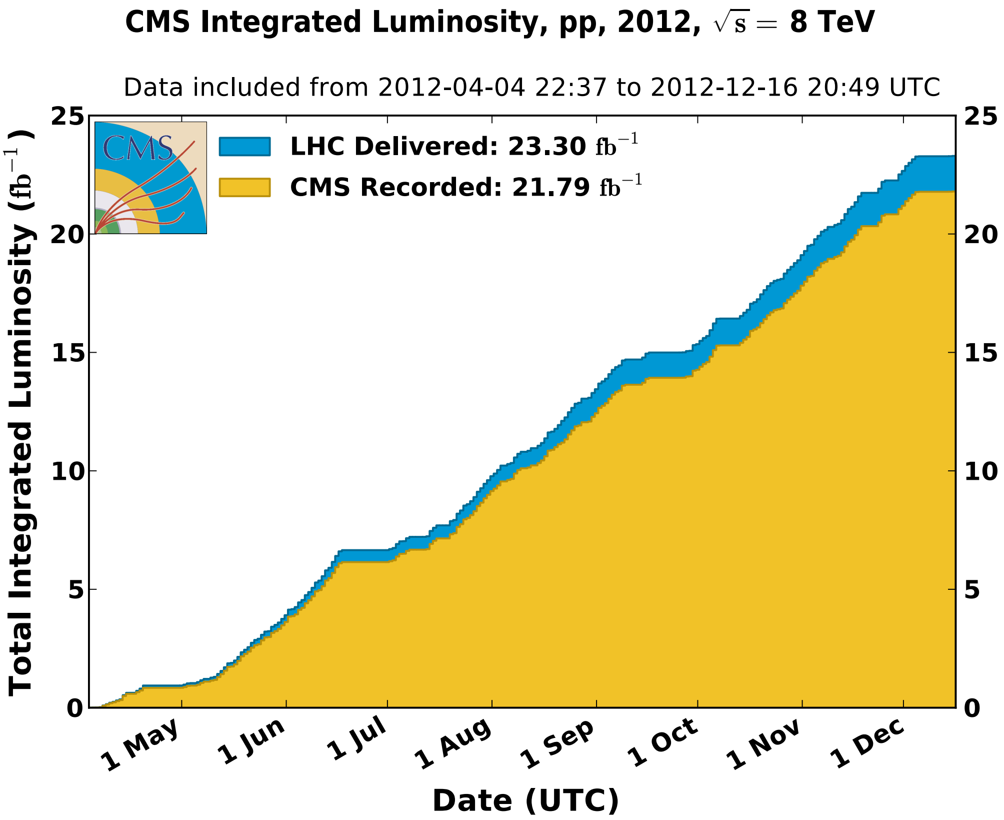

Figure 3.2.: Total integrated luminosity per day provided by the LHC (blue) and recorded by the CMS experiment (orange) in 2012 [92].

3.2. The Compact Muon Solenoid Detector

The Compact Muon Solenoid (CMS) detector [88] is a multipurpose detector located 100 m below ground at Point 5 near Cessy, France. It is designed to study proton-proton collisions as well as heavy ion collisions. The CMS detector has a total length of 28.7 m, a diameter of 15.0 m and a total weight of 14000 t, with the steel return yoke alone weighting 12500 t. An overview of the CMS detector and its detector parts is shown in Fig. 3.3. It has twice the mass and half the volume of ATLAS and can be referred to as *compact*. This compactness allows to fit the tracker and most calorimeter systems in the *solenoid*. The design of the CMS detector was driven by the aim to discover the Higgs boson and to search for supersymmetric particles. The most promising channels before and now validated during the Higgs boson discovery either have leptons ($H \to ZZ^* \to \mu\mu\mu\mu$) or photons ($H \to \gamma\gamma$) in the final states. For this reason the CMS detector was built to be able to precisely measure isolated leptons, especially *muons*, and photons. The high angular coverage and hermetic design of the detector allows to measure missing transverse energy which is an important indicator for supersymmetric processes.

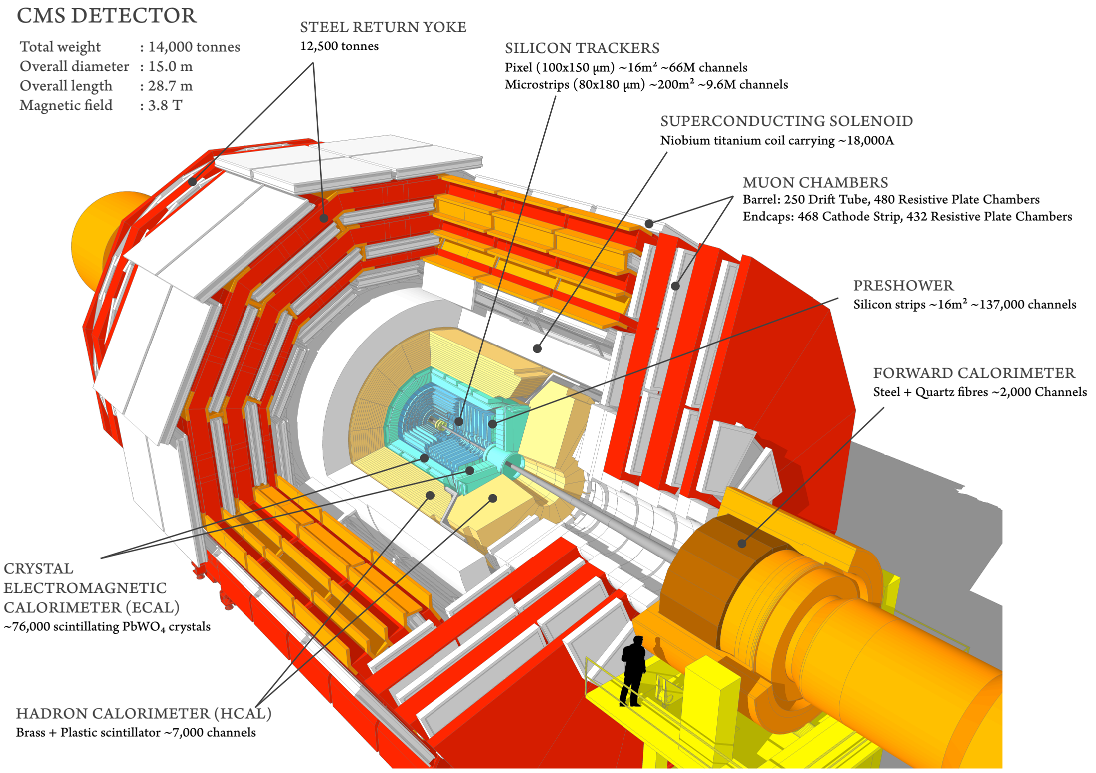

Figure 3.3.: Schematic overview of the CMS detector [93]. The cutaway view shows all relevant parts of the detector and a description. A humanoid figure is shown as scale reference.

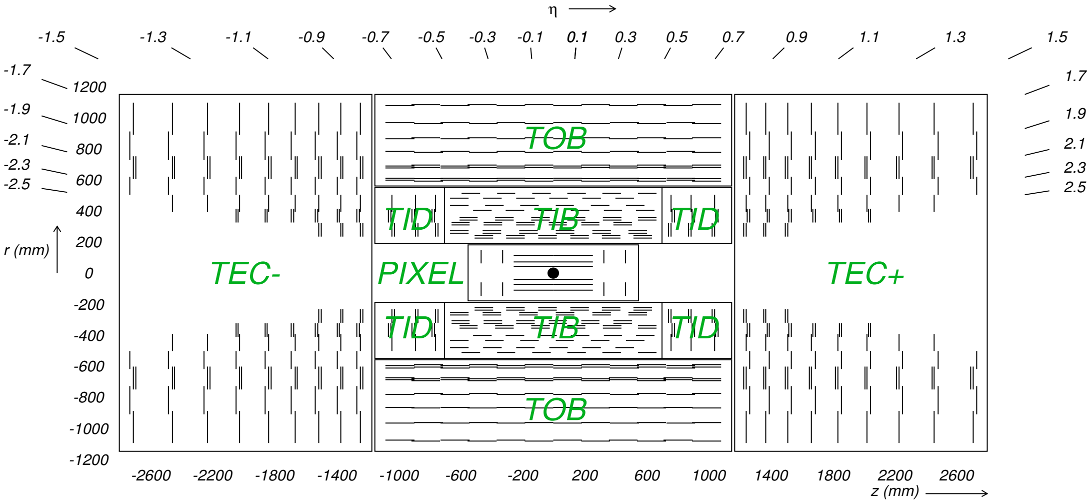

Figure 3.4.: Schematic overview of the CMS tracking system [88]. The pixel detector surrounds the interaction point (black dot). The strip detector consists of tracker inner barrel (TIB), tracker outer barrel (TOB), tracker inner disc (TID) and tracker endcaps (TEC). Detector modules are depicted as single lines, stereo modules as double lines.

Coordinate System

The coordinate system employed by the CMS Collaboration has its origin at the nominal collision point, with the y-axis pointing upward and the x-axis pointing radially towards the LHC center. The z-axis points along the beam direction towards the Jura mountains. The azimuthal angle ϕ is defined in the x-y plane measured from the x-axis. The polar angle θ is measured from the z-axis. The pseudorapidity is defined as $\eta = -\ln \tan(\theta/2)$.

Tracking system

The tracking system [94,95] provides precise measurements of tracks, impact parameters and secondary vertices of charged particles. The tracking system is 5.8 m long, has a diameter of 2.5 m and is embedded into a support tube cooled down to $-20\,^{\circ}$C. The active material of all silicon detectors is 200 m^2, approximately the size of a tennis court. The charge and momentum of a particle passing trough the tracker can be inferred by the curvature of the track caused by the applied magnetic field of 3.8 T produced by the solenoid. The tracker needs to have a fast response time and high granularity to register the on average 1000 particles traversing the tracker during each bunch crossing at the LHC design luminosity. An overview of the tracking system is shown in Fig. 3.4.

Silicon Pixel Detector

The silicon pixel detector encloses the beam pipe with 1440 modules arranged in three barrel layers with a total length of 53 cm and two endcaps extending from 6 cm to 15 cm in radius. It has an area of 1 m^2 and 66 million pixels. Each pixel has an area of 100 x 500 $\mu\mathrm{m}^2$. The expected single point resolution is 10 μm in the $r - \phi$ direction and 15 μm in the z direction. The pseudorapidity range covered is $|\eta| < 2.5$.

Silicon Strip Detector

The silicon strip detector surrounds the pixel detector. It consists of 15148 silicon strip detector modules with 9.6 million silicon strips in different subsystems: tracker inner barrel (TIB), tracker outer barrel (TOB), tracker inner discs (TID) and tracker endcaps (TEC). The TIB consists of four layers of silicon sensors, has a thickness of 320 μm and uses sensors with a strip pitch between 80 and 120 μm. The first two of these layers from the interaction point consists of stereo modules. The TOB consists of six layers with a thickness of 500 μm and a strip pitch from 120 μm to 180 μm. In $r - \phi$ the single hit resolution is $23 - 25$ μm in the TIB and $35 - 53$ μm in the TOB. The z resolution varies between 230 and 530 μm. For muons with a transverse momentum on the order of 100 GeV the expected transverse momentum resolution is around 1.5%.

Electromagnetic Calorimeter

The electromagnetic calorimeter (ECAL) surrounds the tracking system and contains 75848 lead tungstate crystals ($PbWO_4$) which are completely transparent although made of 86% metal. The electromagnet barrel contains 61200 crystals and each of the electromagnetic endcaps (EE) contain 7324 crystals. The high energy density of 8.28g/cm^3 and a short radiation length $X_0 = 0.89$ cm of lead tungstate allow the ECAL to be a homogeneous calorimeter where the absorbing material is the same as the sensitive material. About 80% of the scintillating photons are emitted within the 25 ns of the nominal LHC bunch crossing time. These photons are detected by silicon avalanche photodiodes (APD) in the barrel region and vacuum phototriodes in (VPTs) in the endcap region. The performance of the electromagnetic calorimeter has been estimated with electron beam measurements (20 -250 GeV) [96] as

$$\frac{\sigma_E}{E} = \frac{2.8\%}{\sqrt{E}} \oplus \frac{12\%}{E} \oplus 0.3\%\,, \tag{3.3}$$

where the three terms correspond to a stochastic, noise and constant term. The energy resolution of the ECAL has been further calibrated with collision data taken at $\sqrt{s} =$ 7 TeV to excellent precision [97].

Hadron Calorimeter

The hadron calorimeter (HCAL) is a sampling calorimeter. The absorber material consists of non-magnetic brass which has a radiation length of $X_0 = 1.5$ cm and a short nuclear interaction length of 16.42 cm due to its high density. The HCAL consists of the hadron barrel (HB), hadron endcap (HE), hadron outer (HO) and hadron forward (HF) calorimeters shown in Fig. 3.5. The HB consists of 36 wedge shaped flat brass absorber plates aligned parallel to the beam axis. Sandwiched between them are 17 active plastic scintillators. The inner- and outermost layers are made of stainless steel to have the necessary structural strength. The pseudorapidity range covered by the HB is $|\eta| \leq 1.3$. Next to it is the HE which covers the pseudorapidity range $1.3 < |\eta| < 3.0$. The ECAL is surrounded by both the HB and HE. The HO covers the pseudorapidity range of $|\eta| \leq 1.26$ and is located outside the solenoid. It consists of two scintillator tiles mounted on the outside of the vacuum tank of the solenoid. Using the solenoid as additional absorber material it improves the tails of the energy resolution function and missing transverse energy measurement. The forward region is covered by the HF with a pseudorapidity range of $3.0 < |\eta| < 5.0$. It is made of quartz fibers embedded in cylindrical steel absorbers. The Cherenkov light emitted by particle showers in the quartz fibers is amplified by fast photomultipliers, enabling real time luminosity measurements. The large η coverage of the HF enables the detection of forward jets which are an important signature of the single top quark t-channel process.

Superconducting Solenoid

With a diameter of 6 m, a length of 13 m, and a mass of 220 t, the superconducting solenoid is the largest ever built today. The solenoid coil was designed to be large enough so that all calorimeter system fit inside it which avoids scattering, absorption and showering in the solenoid material. The maximum magnet field supplied is 4 Tesla. At $\sqrt{s} = 8$ TeV it was operated at 3.8 Tesla. The magnetic flux of this field is returned via the iron return yoke. With a weight of 11400 t the return yoke is the heaviest part of the CMS detector.

Muon System

The muon system is the outermost part of CMS since usually only muons travel that far in the detector. It is integrated into the return yoke in a magnetic field of 2 T and is used to identify muons and to provide a secondary measurement of their transverse momenta besides the tracking system. Depending on the used detector part, identified muons are classified into standalone, tracker or global muons. The layout of the muon system is shown in Fig. 3.6. The CMS muon system consists of three different gaseous muon detectors: Aluminium drift tube (DT) chambers are arranged in four layers and are used to identify muons in the barrel region with $|\eta| < 1.6$. In contrast to the endcap regions the muon rate and neutron-induced background is low enough for DTs. Cathode strip chambers (CSC) measure the position of muons in the endcaps and are used to match tracks within the silicon detectors. Each endcap has four stations of CSCs which cover a η region of $0.9 < |\eta| < 2.4$. Resistive plate chambers (RPC) identify muons in the central barrel and endcap region with very high time resolution that aid in the identification

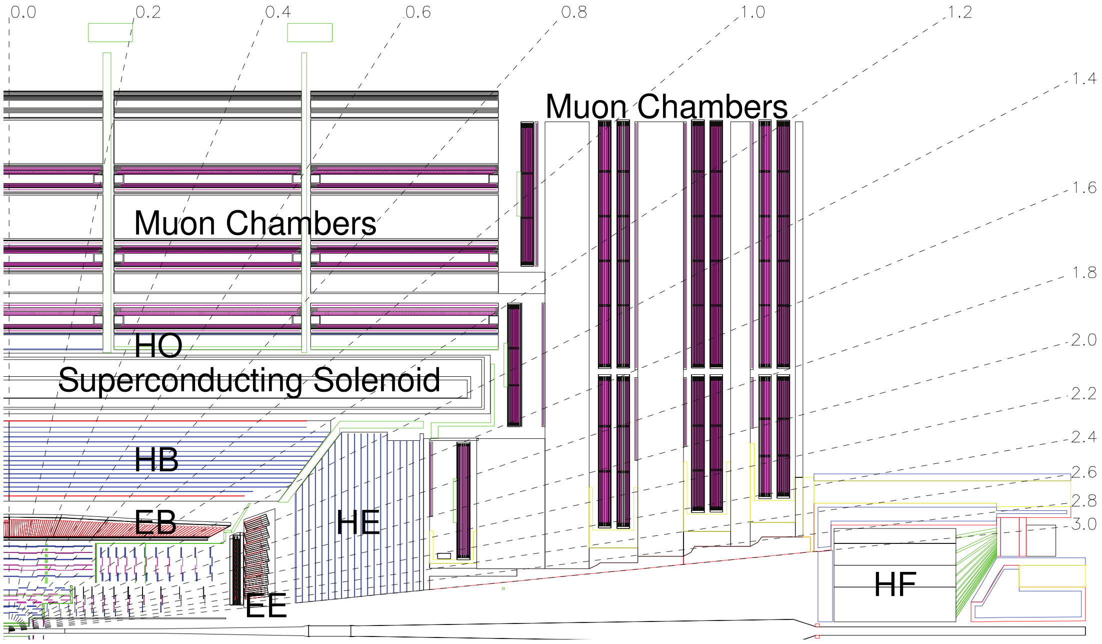

Figure 3.5.: Longitudinal view of one quarter of the CMS detector [88]. Shown is the tracking system together with the ECAL and HCAL surrounded by the superconducting solenoid with the exception of the Hadron Outer (HO) and Hadron Forward (HF) calorimeters. The central part is equipped with the Electromagnetic Barrel (EB) and Hadron Barrel (HB). The Electromagnetic Endcap (EE) and Hadronic Endcap (HE) are installed at the endcaps. The muon chambers are installed in the iron return yoke.

of the collision by providing fast trigger information in the $|\eta| < 1.6$ region. A more detailed description of the muon system can be found in Ref. [99].

Data acquisition and Trigger System

The bunch crossing interval at the nominal LHC design luminosity is 25 ns. This corresponds to a crossing frequency of 40 MHz with approximately 20 simultaneous proton-proton collisions every crossing. The enormous amount of data (100 TB/s) resulting from all these collisions is impossible to store and process in real-time. In order to reduce this rate a trigger system selects only a subset of these events relevant for physics analyses. This reduction is performed in two steps with the Level-1 (L1)trigger and subsequently the High-Level Trigger (HLT). The L1 trigger consists of programmable hardware like FPGAs and ASICs, allowing a low latency of 3.2 μs, which use coarse information from the calorimeters and muon system to reduce the event rate to less than 100 kHz. The HLT consists of a cluster of around thousand computers which run software similar to the offline analysis framework. The HLT has access to the full detector readout and can run on more detailed information with sophisticated algorithms to enable a full

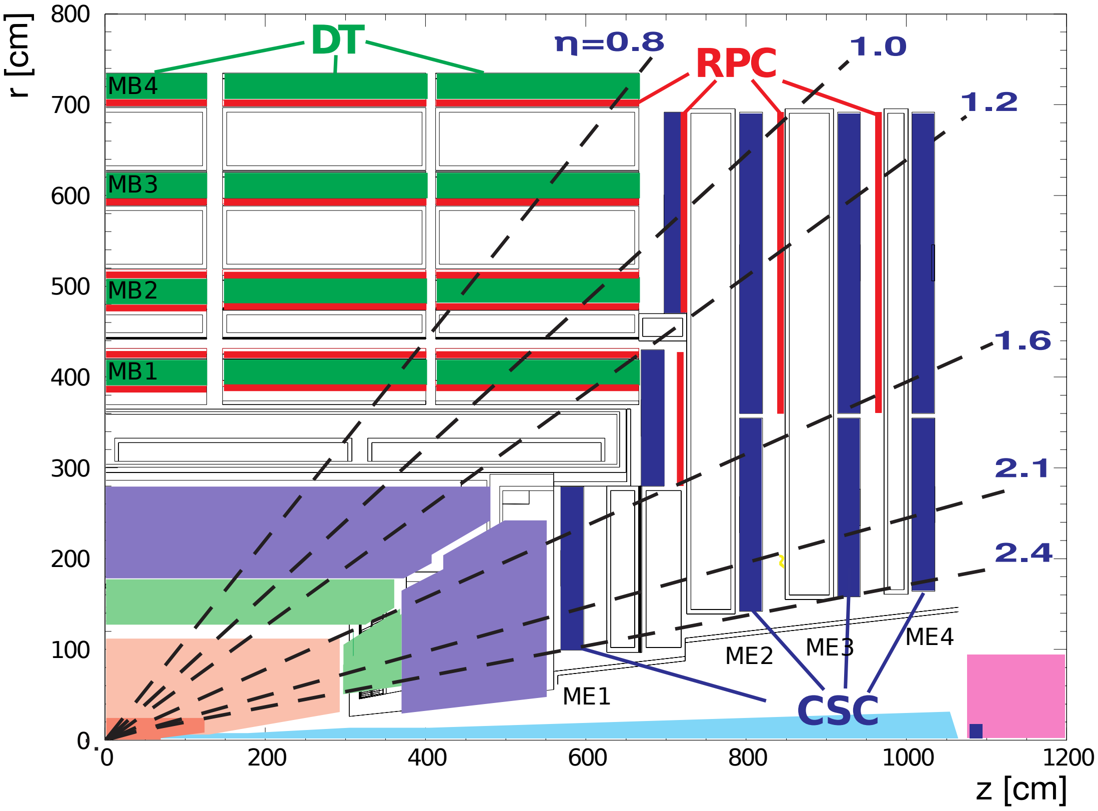

Figure 3.6.: Longitudinal view of one quarter of the CMS muon system [98]. Muons are detected by DT chambers (green) in the barrel region and by CSCs (blue) in the endcap region. Both regions are covered by RPCs (red).

reconstruction which further reduces the event rate to 100 Hz. This allows the storage of the raw detector data of these events for further processing. An overview of the architecture of the CMS Data Acquisition system is shown in Fig. 3.7.

3.3. Computing Infrastructure

The computing infrastructure is a vital part of the experimental setup. Even after the reduction of several orders of magnitudes by trigger systems the experiments at the LHC produce many petabytes each year which have to be processed, archived and distributed to the different computing centers in order to be reachable for the end users to be analyzed. The Worldwide LHC Computing Grid (WLCG) [101] was launched in 2002 to process and store the massive amount of data produced by the LHC experiments. The computing services are integrated into a single service, called the grid. An overview of the CMS computing grid [102] is shown in Fig. 3.8 [100]. The raw data is read out from the detector and stored at the Tier-0 site at CERN. After a first processing step

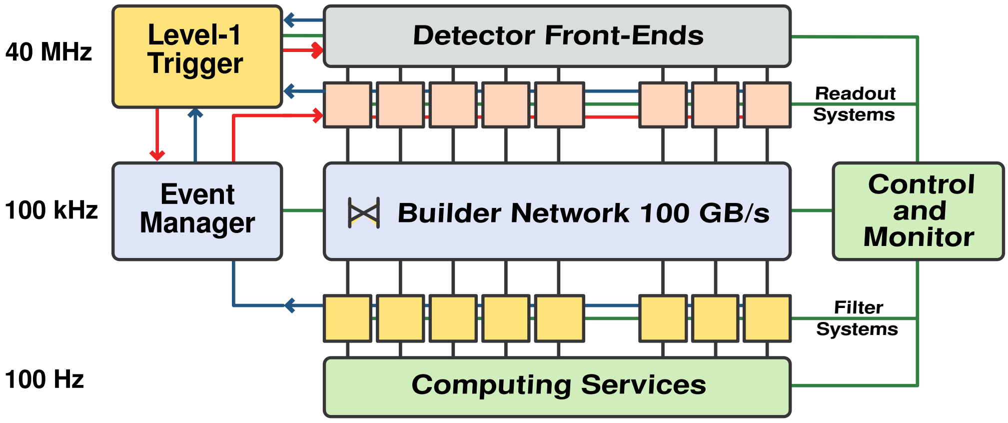

Figure 3.7.: Architecture of the CMS Data Acquisition System [88]. The complete detector read-out data of an event is first buffered in a pipeline. After receiving a L1 trigger signal the detector information is forwarded to the readout systems. The event manager controls the data flow. The builder network processes and defragments the information and passes it to the filter system of the HLT. All steps are controlled and monitored by the control and monitor system.

it is forwarded to various Tier-1 centers around the world. At least two independent sites archive a dataset. Tier-1 centers also provide custodial storage for simulated data. The smaller Tier-2 centers store copies of MC samples and datasets needed for analyses. Analysis jobs submitted by a user to the grid are sent to clusters provided by Tier-2 sites. Local analyses are performed at Tier-3 sites which provide computing and storage services to the end users.

As the functionality of a grid site is one of the most important factors for analyses to be successful it is crucial to actively monitor a grid site in order to prevent computing outtakes or data loss. Grid sites provide their services through the interplay of heterogeneous software. Each service has to be monitored individually and often comes with its own monitoring solution providing unstructured data. Correlation between error sources becomes difficult as each monitoring solution provides different output and has a distinct graphical interface. To gather all relevant information one has to check multiple monitoring systems and change their specific visualization settings. Additionally, most available monitoring solutions are difficult to use for non-experts and often have high latency due to their database backends. All this unnecessarily increases the amount of time required for people on shift monitoring the site.

During the service work part of this thesis a new version of an existing monitor framework was developed and extended in order to facilitate the administration of the local grid site. The HappyFace project [103, 104] is a meta-monitoring software developed in order to monitor the GridKa Tier-1 center at the Karlsruhe Institute of Technology for the CMS Collaboration. HappyFace provides a modular framework to gather information from different monitoring sources, process this information and provide an overview of all relevant information. It allows real-time site monitoring

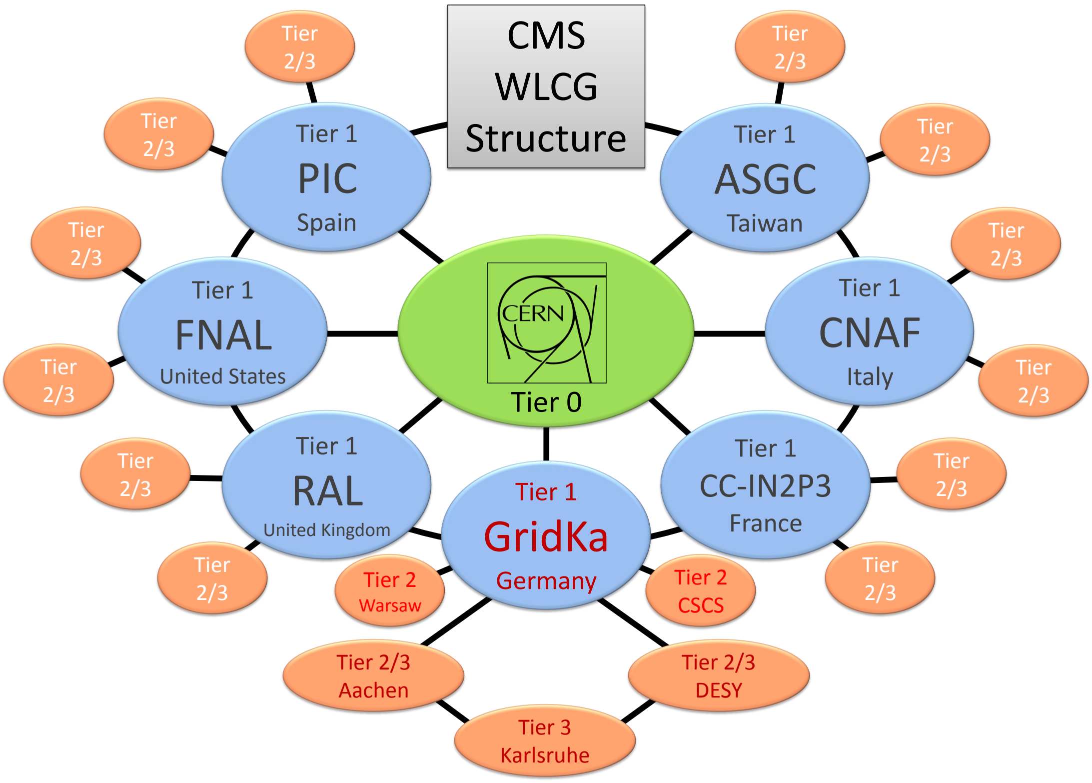

Figure 3.8.: Schematic overview of the CMS computing grid [100]. The Tier-0 site at CERN processes and distributes all raw data collected by the detector. This data is transferred to Tier-1 centers all over the world for custodial storage. Selected data and MC samples are distributed to Tier-2 sites, where they are made available for processing. The final analysis is performed on Tier-3 sites. Remark: The Tier-1 site in Taiwan has been recently replaced by a new site in Russia.

for shifters and experts. All relevant information from different sources is fetched in a defined time interval and processed. The processed information is displayed graphically with a powerful rating system.

3.4. Reconstruction of Detector Objects

In order to reconstruct physical objects the raw data from the detector has to be processed. Within the CMS experiment this is performed with the CMSSW software framework. As a first step, tracks of charged particles, calorimeter deposits and muon track segments are reconstructed. The reconstruction of these objects is described briefly in the following and in detail in Ref. [98].

3.4.1. Particle Flow Reconstruction

The Particle Flow (PF) algorithm [105–107] tries to correctly identify and reconstruct all collision particles by taking into account information from different subsystems of the detector. This approach results in a much better direction resolution and energy calibration compared with older approaches of jet and missing transverse energy reconstruction that only take the energy deposits in the electromagnetic and hadron calorimeter into account. The PF algorithm clusters objects into five different categories: photons, electrons, muons, charged hadrons and neutral hadrons. In each step the identified particle is removed from the list of input objects and all energy deposits are recalculated to avoid double-counting and ensure that the energy is only associated with one particle. The PF approach starts with the reconstruction of muons since they can be easily identified by their tracks in the muon system. Tracks associated with energy deposits mostly in the ECAL are classified as electrons whereas the corresponding energy is estimated with a multivariate regression technique. Remaining tracks with energy deposits in the HCAL are identified as charged hadrons. Photons and neutral hadrons are distinguished by their energy deposits. The result is a set of PF candidates and missing transverse momentum from which neutrinos can be reconstructed. In the following the basic reconstruction of PF input candidates is described briefly.

3.4.2. Tracks

Charged particles traversing the tracker generate hits in the different tracking layers. The trajectories of these particles can be reconstructed by combining these to tracks. Tracks are reconstructed using an iterative tracking method [108]. The demands set by physic goals [98, 109] of the CMS collaboration requires good momentum resolution of transverse momenta up to 1 TeV and at the same time efficient reconstruction of tracks with p_{T} on the order of 100 MeV for optimal jet energy resolution. The first step of track reconstruction is called *local reconstruction*. It consists of the clustering of signals above a certain threshold in the pixel and strip channels into hits. Track reconstruction at CMS uses these hits from the local reconstruction in order to reconstruct tracks in several steps with the Combinatorial Track Finder (CTF), an extended Kalman filter track finder [110]. The CTF algorithm is iterative, i.e it is passed in multiple sequences. Each of the six sequences consists of four steps. First, initial track candidates are found using track seeds with initially two or three hits. This defines the initial trajectory and its uncertainty. The subsequent track finding is based on a Kalman filter, extrapolating the charged particles path of flight along the tracks seeds to find further hits. Track fitting is used to provide the best possible estimate of the trajectory parameters using a smoother and Kalman filter. At last, tracks failing certain quality criteria are discarded.

3.4.3. Vertices

Vertex reconstruction is based on reconstructed tracks and consists of two parts, vertex finding and vertex fitting. During the vertex finding tracks are grouped into vertex candidates, depending on the use case different algorithms are applied. For the HLT where speed is an important requirement and high efficiency is negligible a fast algorithm is used. Hits which are found in three consecutive layers in the pixel detector are clustered into triplets while taking only the z-coordinates closest to the beam line into account in order to reduce the problem to a one-dimensional search. These clusters are then used as input for the vertex fit. Primary vertex candidates are reconstructed using Adaptive Vertex fitting, a method based on a Kalman filter. The vertex with the highest sum of p_{T}^2 of the associated tracks is tagged as primary vertex (PV). Since the PV is the point where the hard interaction took place the knowledge of the PV is crucial for the reconstruction of an event. Higher accuracy can be achieved by using a full reconstruction of the tracks. For this the tracks have to pass a set of quality criteria. There must be at least two hits in the pixel detector, seven hits in the silicon strip detector and the χ^2-value of the fit divided by the number of degrees of freedom n_{DOF} must be smaller than five, $\chi^2/n_{\mathrm{DOF}} < 5.0$.

3.4.4. Muons

The reconstruction and identifications of muons with the CMS detector is described in Ref. [98,111]. Muons can be reconstructed in several ways. Depending on the subsystems used for reconstruction they are either classified as standalone, tracker or global muons. Standalone muons are reconstructed with information from the detectors of the muon system: DT, CSC, or RPC. The reconstruction is similar to the previously described track reconstruction. A local reconstruction is performed with hits from the muon chambers taken as seeds. These hits are then clustered to track segments. Tracks are propagated from layer to layer using a Kalman filter method while taking energy loss, multiple scattering and the non-uniform magnetic field into account. When no track segment can be found the track is nevertheless propagated to the next layer. A cut on the χ^2-value of the fit is performed to reject bad hits due to showering and pair production. Pairs of tracks sharing a large fraction of hits are cleaned. After the outer layer is reached, the Kalman filter is applied backwards and the track is extrapolated to the nominal interaction point. In the end a vertex-constrained fit on the track hits is performed to estimate the track parameters. Tracker muons are reconstructed without information from the muon chambers and therefore can be used to reconstruct muons with low transverse momentum that only leave a small number of hits in the muon chambers. Tracks reconstructed in the tracker are propagated through the detector to the muon chambers and muons are reconstructed by looking for compatible hits in the muon chambers. Global muons are reconstructed using information from the muon system and the silicon pixel and strip detector. Tracks from the tracker are combined with standalone muon tracks. In order to limit the number of possible combinations a subset of tracks from the tracker is chosen with corresponding momentum and position in the standalone muon tracks. More stringent matching criteria are applied iteratively to further reduce this subset. A global fit is performed in the end on the remaining combinations and the track with the best χ^2-value is chosen as global muon track.

Muon Identification

Additional steps are performed in order to identify muons stemming from the hard interaction. Muons originating from the decay of B mesons or kaons and pions can also be reconstructed as global muons. Hadrons with high enough energy can traverse the HCAL and reach the muon chambers which leads to punch-through hadrons misidentified as muons. These non-prompt muons all have hadronic activity in common which leads to energy deposited in a cone around the muon. Energy deposits in the ECAL and HCAL are used to calculate a scalar sum of energy deposits in a cone with radius $R = 0.3$ in the $\eta - \phi$ plane around the muon track. Energy deposits inside a veto cone are excluded to account for the energy deposited by the muon. The radius of the veto cone is $R = 0.07$ in the ECAL and $R = 0.1$ in the HCAL. The muon identification algorithms [111] furthermore use additional information from the tracker such as the number of hits of the muon candidates, the χ^2-values of the track fits and the number of invalid hits.

3.4.5. Electrons

The reconstruction of electrons [112] is more difficult than the one of muons since electrons have to be reconstructed with the tracking system and ECAL depositions and are hard to separate from fake electrons stemming from jets or photons. Recent improvements in electron reconstruction and identification at CMS are described in Ref. [113]. The energy measurement in the calorimeter is complicated by the radiation of bremsstrahlung by electrons interacting with the tracker material. The amount of bremsstrahlung depends on the tracker material traversed by the electrons. The radiation length of the tracker material varies with the pseudorapidity η and ranges from 0.4 radiation lengths at the central η region up to 1.6 radiation lengths at $\eta \approx 1.6$. The magnetic field leads to the fact that electrons radiate bremsstrahlung photons along their helical trajectories which leads to a spread of the deposited ECAL energy in the ϕ direction. This spread is taken into account by the combination of several clusters into a supercluster (SC). At first, SCs with an energy larger than 1 GeV are used as starting points to find seeds in the pixel detector. Seeds require electron tracks with two hits in the pixel detector. Tracks matched to a SC with a pseudorapidity $|\eta| < 2.5$ and a transverse momentum $p_\mathrm{T} \geq 2.5\,\mathrm{GeV}$ are classified as primary electron candidates. The track finding is performed with a nonlinear Gaussian Sum Filter (GFS) [114, 115]. Here a GSF is used because in comparison with a KF the GSF can cope with the nonlinear effects in the propagation of electrons caused by bremsstrahlung. Similar to muon reconstruction a backward fit is performed in the end. This method works best for high energetic electrons. Electrons with low transverse momentum inside a jet are better reconstructed with a tracker based approach. This approach uses a multivariate technique to identify electron candidates with low transverse momentum inside jets [116].

Electron Identification

In order to distinguish electrons and objects with similar signatures such as charged hadrons more sophisticated algorithms are employed which utilize variables sensitive to bremsstrahlung and electromagnetic showering in the tracker. Transverse energy of the supercluster or the ratio of energy deposited in the ECAL and HCAL are further variables used to identify electrons. For the best performance an electron ID is defined by combining all these variables in a multivariate technique. Depending on the analysis a suitable cut on the discriminator can be chosen with the required purity of electron candidates.

3.4.6. Jets

Colored quarks and gluons cannot exist alone due to color confinement, they hadronize and form clusters of hadrons, detected as jets in the detector. Jets are reconstructed from tracks and grouped into jet objects according to different jet clustering algorithms.

Jet algorithms can take any object with four-momentum as input, e.g. simulated partons, generated stable particles after hadronization and decay or detector objects such as calorimeter hits. Jet algorithms have to satisfy two important requirements, infrared an collinear safety. Infrared safety means that for a given input additional radiation does not lead to a different number of jets. The large probability of soft gluon emissions in a hadron shower, soft contributions from the underlying event or calorimeter noise make this an important requirement. Collinear safety means that a splitting of one particle into two particles with the same four-momentum should not change the output of the jet algorithm. This requirement is important because collinear splitting of one gluon into two gluons and two quarks often occurs in the showering process.

Jet Clustering

Jets are reconstructed with cone algorithms or sequential clustering algorithms. Cone algorithms cluster all particles in a cone with fixed radius R in the $\eta - \phi$ plane. Sequential clustering algorithms have the advantage of not depending on a particular shape. In the following sequential clustering algorithms will be discussed. For each input particle i the distance $d_{i,j}$ to a particle j is defined as $d_{i,j} = \min(p_{\mathrm{T},i}^{2n}, p_{\mathrm{T},j}^{2n}) \cdot \Delta R_{i,j}^2$, where R is defined as the distance in the $\eta - \phi$ plane $R = \sqrt{\Delta\eta^2 + \Delta\phi^2}$. The distance of a particle to the beam is defined as $d_{i,\mathrm{beam}} = p_{\mathrm{T},i}^{2n} \cdot D^2$.

Depending on the choice of the parameter n the algorithms are classified as

- $n = 1$ k_T algorithm [117,118]
- $n = 0$ Cambridge/Aachen algorithm [119]
- anti-k_T algorithm [120]

All of these algorithms and several others are implemented in the FASTJET package [121, 122]. The current default algorithm used by the CMS experiment is the anti-k_T algorithm with a resolution parameter of 0.5.

Jet Energy Corrections

Jet energy correction (JEC) tries to correct the energy measurement of jets from multiple sources of distortion in a sequence of multiple factorized correction steps. These correction levels, defined in Ref. [123] are:

- *Level 1:* The energy offset stemming from pile-up is corrected by subtracting the average pile-up density per unit area depending on the area of the jet.
- *Level 2:* Relative corrections depending on the pseudorapidity η are applied to correct for the non-compensating behavior of the calorimeter and uninstrumented regions of the detector. Correction factors as a function of the pseudorapidity η are calculated to equalize the jet response to the level of the central region $|\eta| < 1.6$.
- *Level 3:* Absolute corrections based on the transverse momentum p_T are applied to correct for non-compensating effects and to make the jet response uniform in p_T.

The corrections in Level 1-3 take all instrumental effects into account. In addition, the *L2L3 residual corrections* correct for the fact that the *L2* and *L3* corrections are determined only from MC samples. Further optional corrections are available in Level 4-7 to estimate the momentum and energy of the underlying partons but are not used in this analysis. The jet energy corrections have been validated in data at $\sqrt{s} = 7$ TeV with dijet and γ/Z events [124]. In addition, the difference between the resolution of jet energy in data and MC simulations is corrected by smearing the jet energy resolution in MC samples [125].

Identification of b-quark jets

Top quark decays lead to jets produced by b-quark hadronization. In order to decimate backgrounds it is crucial to correctly identify these jets. This procedure is known as b tagging. The CMS Collaboration uses several algorithms to accomplish this [126]. Different approaches from simple but robust methods to complex multivariate algorithms are available.

Hadrons with b quarks decay primarily via the weak interaction and therefore have long lifetimes. Jets which originate from a b quark can be distinguished from light quark or gluon jets by the long lifetimes and large masses of B hadrons and relatively high fractions of semileptonic decays which lead to the presence of a soft charged lepton in the jet. The longer lifetimes of B hadrons lead to a displaced secondary vertex. The distance between the track and the PV at closest approach is called impact parameter (IP). A schematic view of a B hadron decay with PV, SV and IP is depicted in Fig. 3.9. The typical

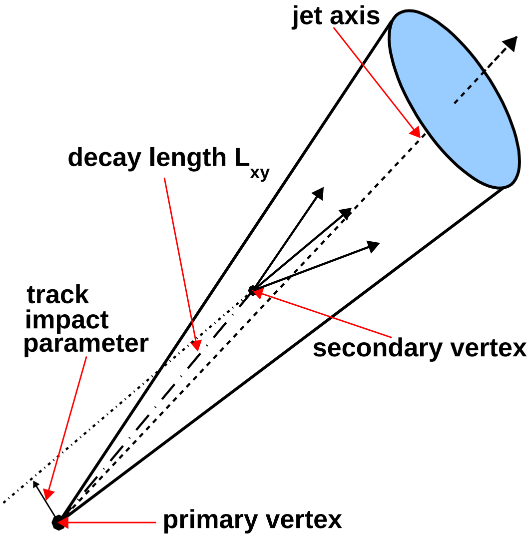

Figure 3.9.: Schematic view of a B hadron decay inside a jet [127]. The decay leads to a secondary vertex displaced with a decay length of L_{xy} from the primary vertex. The impact parameter of a track is the distance between the track and the PV at closest approach.

scale of the IP for B hadrons is defined by their lifetime, $c\tau \approx 480\,\mu$m. The scalar product of the IP segment with the jet direction yields the sign of the IP. Mis-measured tracks can lead to a difference between the reconstructed jet axis with the flight direction of the B hadron which yields a wrong sign of the IP. Decays with a short lifetime have a signed IP significance centered around zero while the one of B hadrons is mostly positive. The main ingredients to identify b jets are charged tracks and lepton identification. In order to compare different algorithms, the efficiency to correctly identify jets from b quarks and the misidentification probability of identifying jets from light quark jets as b quark jets are needed. In general, these are dependent on the transverse momentum p_T and pseudorapidity η of a jet. Since it is difficult to model all b-tagging parameters correctly, the performance has to be corrected with measurements from b quark jet enriched data.

This analysis uses the *Combined Secondary Vertex* (CSV) algorithm which exploits multiple variables to distinguish b quark jets from non-b quark jets. Information such as the IP, the SV and jet kinematics are combined into a likelihood ratio to calculate a b-tag discriminator. Soft lepton information is not included. The probability to falsely classify a light quark or gluon jet as b quark jet is the mistag rate. According to the mistag rate several working points are defined by the minimum threshold of the discriminator. The working points are named *loose* (L), *medium* (M) and *tight* (T) with a misidentification probability for light parton jets around 10%, 1% and 0.1%, respectively, at an average jet p_T of about 80 GeV.

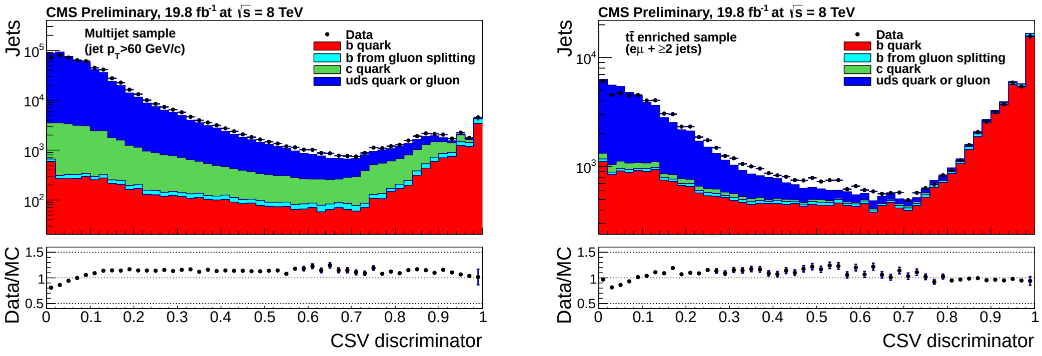

(a) (b)

Figure 3.10.: Discriminator values for the CSV algorithm in an inclusive QCD multijet (a) and in a $\mathrm{t\bar{t}}$ enriched (b) sample [128].

3.4.7. Missing Transverse Energy

Since the colliding particles at the LHC only have longitudinal momentum the transverse momentum must be conserved due to momentum conservation. However, particles like the neutrino or proposed supersymmetric neutralinos do not interact with the detector material and lead to an imbalance in the transverse energy measured in the calorimeters. Missing transverse momentum ($\vec{\not{E}}_\mathrm{T}$) is defined as the vectorial sum of all transverse momenta deposits in the calorimetry system [129]:

$$\vec{\not{E}}_\mathrm{T} = -\sum_{n=1}^{N} \left(E_n \sin\theta_n \cos\phi_n \hat{x} + E_n \sin\theta_n \sin\phi_n \hat{y} \right) , \tag{3.4}$$

where the index n runs over all calorimeter input objects and $\hat{x}$ and $\hat{y}$ denote the unit vectors in the x and y direction, respectively. The magnitude of $\vec{\not{E}}_\mathrm{T}$ is called missing transverse energy, $\not{E}_\mathrm{T}$ or MET. In the case of Particle Flow MET (PFMet) [105] the missing transverse energy is calculated with PF objects instead of using calorimeter information. In order to accurately estimate the amount of missing transverse energy one has to take pile-up effects and mis-reconstruction into account. Particles too close to the beam line can escape the detector without being reconstructed. Detector malfunction and dead sensors or poorly instrumented regions have to be considered as well. If the number of affected channels is small, the event can be cleaned. Events with large anomalous signals in the calorimeter system are tagged as nonphysical and filtered out. The impact of multiple interactions per bunch crossing, pile up, leads to the degradation of missing transverse energy resolution. The nonlinearity of the calorimeter response for neutral and charged hadrons due to its non-compensating nature, neutrinos from semileptonic particle decays or minimum energy thresholds of the calorimeters and inefficiencies in the tracker can lead to an underestimation of $\not{E}_{\mathrm{T}}$.

Jets are an important ingredient for the calculation of missing transverse energy. The Type-I corrections propagate the jet energy corrections (JEC), introduced in the previous section, to $\not{E}_{\mathrm{T}}$. Type-0 correction mitigates the effect of pile-up on $\not{E}_{\mathrm{T}}$. Charged hadron subtraction (CHS) removes charged hadrons originating from pile-up vertices from the $\not{E}_{\mathrm{T}}$ estimation. In addition to CHS, an integral part of type-0 corrections is the removal of neutral pile-up contributions. This is performed by removing an estimated amount of neutral pile-up contributions from $\not{E}_{\mathrm{T}}$. Only removing the charged contribution would lead to a worse estimate of $\not{E}_{\mathrm{T}}$. The missing transverse energy used for the analysis in this thesis can be written as

$$\vec{\not{E}}_{\mathrm{T}} = \vec{\not{E}}_{\mathrm{T}}^{\mathrm{raw}} + \vec{C}^{\text{type-0}} + \vec{C}^{\text{type-I}} \tag{3.5}$$

where $\vec{C}^{\text{type-0}}$ and $\vec{C}^{\text{type-0}}$ are the type-0 and type-I corrections for $\vec{\not{E}}_{\mathrm{T}}$.

4. Simulation of Single Top Quark Production

The first step of a particle physics analysis is the simulation of the physical processes in order to study kinematic distributions and selection efficiencies. Both signal and background processes have to be studied in order to define a suitable selection with a sufficient signal-to-background ratio. The simulation of physical processes is performed with the help of Monte Carlo (MC) methods [130], stochastic methods based on random sampling. The hard interaction of a process is simulated by randomly producing events according to the matrix elements of the process and the probability density of the according phase space. In order to be able to compare measurements on data with simulations, the simulated events have to be reconstructed with a detector simulation. In the following chapter the main ingredients of such a simulation are described, the available generators and the different modeling techniques for single top quark production are introduced and a brief overview of the detector simulation is given.

4.1. Monte Carlo Simulation

A full proton-proton collision can be factorized in several different steps of the interaction. An illustration of this factorization is shown in Fig. 4.1. In the following, the different steps will be described briefly.

Hard Scattering and Parton Distributions

The momentum fractions of each parton flavor in a proton at a given momentum transfer Q^2 are described by a set of parton distribution functions. (PDFs). A brief introduction was already given in Section 1.2. In a proton-proton collision one parton from each proton takes part in the hard scattering process. Since the strong coupling constant α_S is small at large Q^2 the cross section of a hard scattering process can be calculated with perturbation theory.

Parton Shower

A parton shower (PS) simulates the radiation of gluons and quarks in the initial and final state of a hard process. Initial state showers are produced by an incoming parton radiating a gluon. Final state showers are produced by a gluon radiated from quark the final state. Gluon radiations are described by branchings which are calculated with the help of the DGLAP QCD evolution functions, see Section 1.2, where the probability of

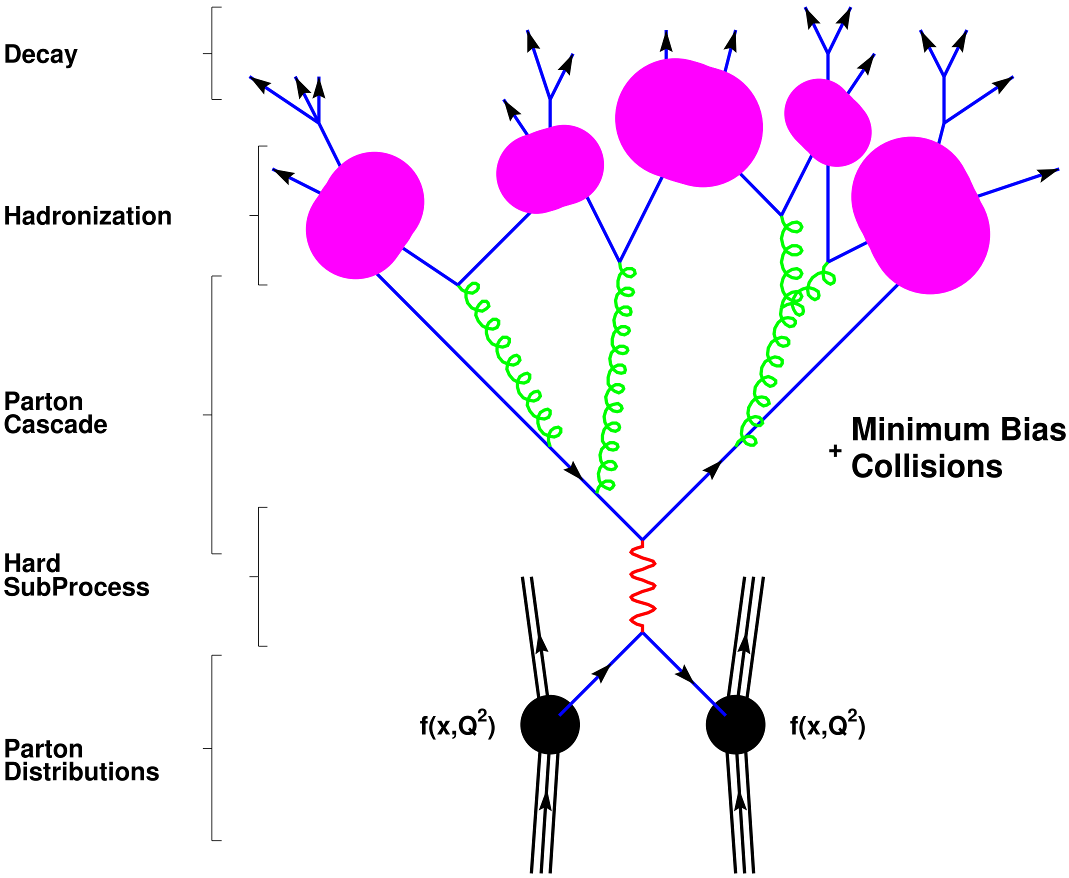

Figure 4.1.: Schematic illustration of the factorization of a proton-proton collision [131].

radiating a gluon is calculated with the Altarelli-Parisi splitting functions. Initial state PS are approximated as space-like showers where the scale is increased backwards in time until the initial parton of the shower is found. Final state PS are instead approximated by time-like showers starting from the final state partons of the hard scattering. The scale is decreased along the positive time axis. A lower cutoff scale is introduced in order to avoid singularities from soft and collinear gluon emissions.

Hadronization

Perturbation theory is only valid when the couplings are small enough, therefore perturbative QCD is only valid at short distances where the strong coupling constant is small. In nature colored partons can not be directly observed since they are bound in hadrons. The transformation of colored partons into bound states of colorless hadrons is called hadronization. There are only phenomenological models and no analytical explanations available for this confinement. One phenomenological model of hadronization is the

Lund string model [132] used by PYTHIA. The color field between the separating quarks and anti-quarks in the finale state is modeled as a color flux string. When the separation is large enough, the potential energy between these strings is large enough to create new quark anti-quark pairs with color and anti-color. These newly created quark anti-quark pairs lead to the production of colorless hadrons.

Underlying Event and Pileup

Apart from the hard scattering process there is a color charged proton remnant from the proton collision which interacts with particles in the hard interaction. This underlying event has to be taken into account in the MC simulation for a correct modeling of the proton-proton collision.

During the same bunch crossing multiple interactions can occur at high luminosities. The number of additional collisions in an event is called pileup (PU) rate. The average pileup rate at $\sqrt{s} = 8$ TeV was around 23 additional collisions with in extreme cases well over 40 pileup events [133]. The correct simulation of pileup is an important ingredient for a correct MC simulation of proton-proton collisions.

Detector Simulation

In order to be able to compare events reconstructed from data with generated events, the interaction of the generated particles with the detector material, the applied magnetic field and the response of the different detector subsystems have to be calculated. Physical effects like energy loss by ionization, multiple scattering, bremsstrahlung and electromagnetic and hadronic interactions have to be considered. All simulated events used in this analysis pass a full detector simulation with the GEANT4 [134, 135] toolkit using a detailed model of the CMS detector.

4.2. Parton Showers and Monte Carlo Generators

In the following, the parton showers and MC generators used in this thesis are presented. A detailed overview of MC generators available for hadron colliders can be found in Ref. [136]. The generated events are stored in the Les Houches event format (LHE) [51], a standardized XML-like format which can be passed on to parton shower programs.

Pythia

PYTHIA [80] is a multi-purpose MC event generator for particle collisions at high energies. It includes theories and models for hard and soft interactions, parton distributions, initial- and final-state parton showers, multiple interactions, fragmentation and decay. Hadronization is described by the Lund string model explained in Section 4.1.

In this thesis PYTHIA 6 is used for the modeling of QCD multijet and diboson background events and for the showering and hadronization of events generated with different MC generators listed in the following.

MadGraph

MADGRAPH [137] is a program which can generate matrix elements at tree-level for any Lagrangian based model implemented in FEYNRULES [138] and produce the amplitudes and information for the phase space integration for a given process. MADEVENT [139] uses this information to produce standalone code in order to calculate cross sections and generate events.

aMC@NLO

Recent versions of MADGRAPH since version 5 include the AMC@NLO package [140] which enables the automatic computation of LO and NLO amplitudes for arbitrary processes and their matching to parton shower simulations according to the MC@NLO formalism [141].

POWHEG

The POWHEG method [79,142] (Positive Weight Hardest Emission Generator) is a method for interfacing parton showers with fixed NLO QCD calculations. It is designed to remove a potential overlap between the parton shower and the NLO hard process and to only produce events with positive weight. This method is used by the framework POWHEG BOX [77] to produce events with NLO precision. Several SM processes are available. The *s*- and *t*-channel [78] and tW [143] events used in this analysis have been produced with POWHEG BOX. Although not used in this analysis it can also be used to simulate $t\bar{t}$ events [144]. POWHEG BOX can be either interfaced to PYTHIA 6 or Herwig for the parton shower modeling.

CompHEP

COMPHEP [82] is an automated package for the evaluation of Feynman diagrams and generation of events. It can be interfaced to PYTHIA for the showering and hadronization and is used in this thesis for the production of an alternative single top quark *t*-channel sample [83].

Tauola

The TAUOLA library [81] was designed to correctly simulate the decay of τ leptons, especially the spin correlation effects important for the correct modeling of the top quark polarization are taken into account. The library can be interfaced to other MC generators to simulate the decay. It is used here for the simulation of the decay of the single top quark and diboson events.

4.3. Simulation of t-channel Single Top Quark Physics

The initial b quark needed for t-channel single top quark production can be simulated in two distinct flavor schemes (FS), either in the 4FS with four, or in the 5FS with five different quark flavors in the initial state. The Feynman diagrams of the $2 \to 2$ process used at Born level in the 5FS and the $2 \to 3$ process used at Born level in the 4FS are shown in Fig. 4.2.

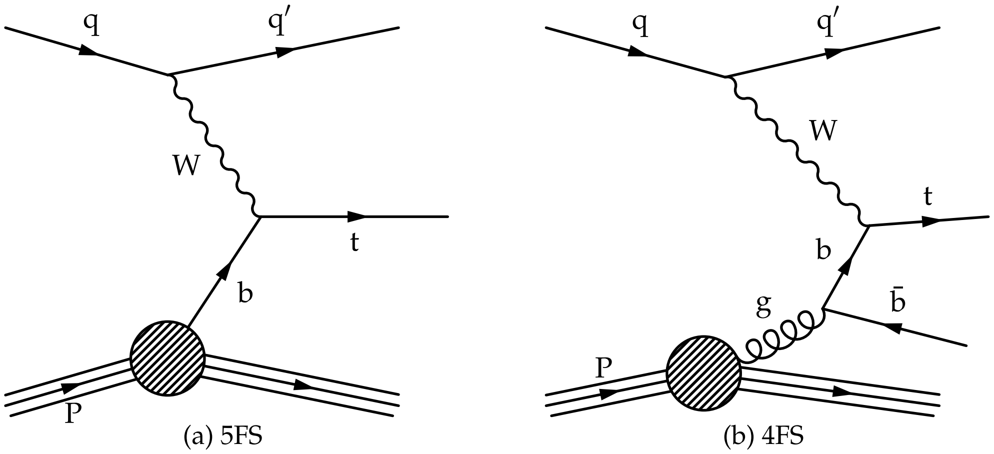

(a) 5FS (b) 4FS

Figure 4.2.: Single top quark t-channel production in the 4- and 5-flavor scheme. The $2 \to 2$ process is shown in (a), where the b quark originates from the proton PDF. The second b quark is simulated through the parton shower. The $2 \to 3$ process is shown in (b), where the b quark originates from gluon splitting. Here the second b quark is simulated directly and therefore more accurately modeled than with a parton shower.

The $2 \to 2$ process is shown in Fig. 4.2 (a). Here the initial state b quark originates from the proton PDF, the logarithms related to the initial state gluon splitting are resummed in the b quark PDF. The second b quark only enters via NLO corrections and is simulated through the parton shower, describing it effectively only at LO. In order that the factorization of matrix element and parton shower is valid, the mass of the b quark has to be neglected in the matrix elements of the 5FS, $m_b = 0$, and only enters through some higher order corrections.

The $2 \to 3$ process is shown in Fig. 4.2 (b), where the b quark originates from a gluon splitting into a $b\bar{b}$ pair. In the 4FS the b quark is part of the matrix element and massive, the second b quark is also simulated directly and massive. Although the calculation is much more complicated, the modeling of the kinematic distributions is more accurate. The difference in the resulting kinematic distributions of these two flavor schemes has been studied in detail at NLO in Ref. [67].

The kinematic distributions of the top quark resulting from the POWHEG BOX 4FS modeling are very similar to the ones obtained with AMC@NLO [144].

The parton level distribution of the top quark transverse momentum p_T generated with AMC@NLO in the 4FS and 5FS is shown in Fig. 4.3. The distributions agree within

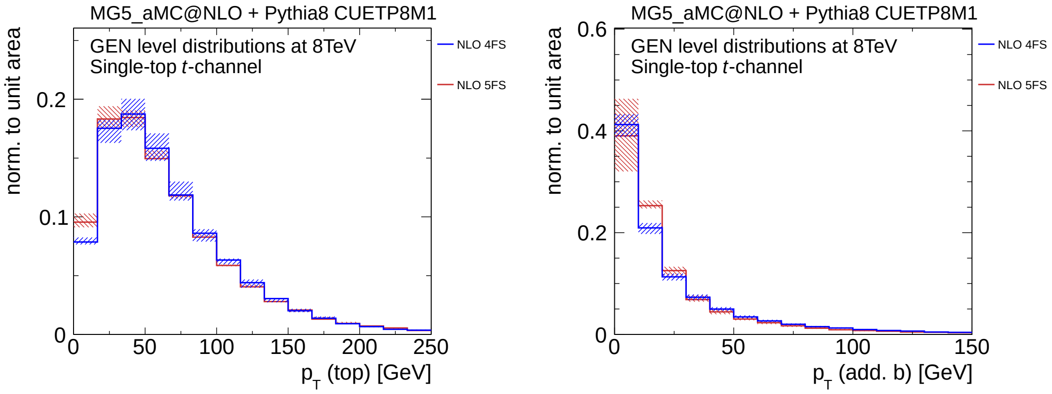

(a)

(b)

Figure 4.3.: Transverse momentum p_{T} of the top quark (a) and second b quark (b) generated with aMC@NLO at NLO in the 4FS and 5FS [145].

the uncertainties indicated by the shaded areas. Small differences are seen only in the low p_{T} area [145].

A different approach is used by the CompHEP generator. In order to get an approximative NLO modeling, the contributions of the $2 \rightarrow 2$ and $2 \rightarrow 3$ processes are merged according to a matching in the distribution of the second b quark transverse momentum p_{T}.

5. Event Selection and Signal Event Reconstruction

As shown before in Fig. 1.3 the single top quark t-channel cross section is around 11 orders of magnitude smaller than the total inelastic proton-proton cross section. An event selection has to be defined where only events with signal-like final state are selected. However, many background processes have the same final state as t-channel single top quark production. With the help of MC simulations suitable cuts are defined that reject most of the background events without rejecting too many signal events. The selection used in this analysis selects for events where the top quark decays to a W boson and b quark with a subsequent decay of the W boson to either a muon or electron and the corresponding neutrino, $t \rightarrow Wb$, with $W \rightarrow \mu\nu\ (e\nu)$. The hadronic decay mode of the top quark is neglected as it is too similar to the QCD multijet background.

5.1. Utilized Data Samples

The data used for the analysis in this thesis consists of an integrated luminosity of 19.7 fb^{-1} collected during 2012 at $\sqrt{s} = 8$ TeV with single lepton triggers.

The following data samples have been used:

- /SingleElectron/Run2012A-22Jan2013-v1/AOD
- /SingleElectron/Run2012B-22Jan2013-v1/AOD
- /SingleElectron/Run2012C-22Jan2013-v1/AOD
- /SingleElectron/Run2012D-22Jan2013-v1/AOD
- /SingleMu/Run2012A-22Jan2013-v1/AOD
- /SingleMu/Run2012B-22Jan2013-v1/AOD
- /SingleMu/Run2012C-22Jan2013-v1/AOD
- /SingleMu/Run2012D-22Jan2013-v1/AOD

Only events where the CMS detector was fully operational have been used for this thesis. The luminosity sections marked bad by the Detector Performance Group (DPG) have been excluded. The certified `JSON` file, containing all good runs, `Cert_190456-208686_8TeV_22Jan2013ReReco_Collisions12_JSON.txt` has been used to exclude these events.

The MC samples used in this thesis are listed in Table 5.1. Listed are the sample name, the amount of generated events and the cross section times the branching ratio (BR). All samples are from the `Summer12` cycle of the CMS MC production and have been processed with the `5_3_11` release of the `CMSSW` package. The QCD Multijet contribution has been estimated with a data driven technique described in Section 5.4.

5.2. Background Processes

Several other processes have the same signature as single top-quark production in the detector and have to be considered in the analysis as background. In the following the background processes relevant for this analysis will be described.

5.2.1. Top Quark Production

Top quark pair production is one of the most important background processes for single top quark production. The production of $\mathrm{t\bar{t}}$ pairs is described in in Section 1.3.1. The main contribution stems from the semileptonic decay mode, where one top quark decays hadronically, producing two jets from the W boson and one b quark jet, and the other leptonically, producing a b quark and a charged lepton and neutrino. Two of these jets are not reconstructed due to either low transverse momentum p_{T} or blind regions in the detector. Other top quark production backgrounds are *s*-channel and tW single top quark production.

5.2.2. Vector Boson Production

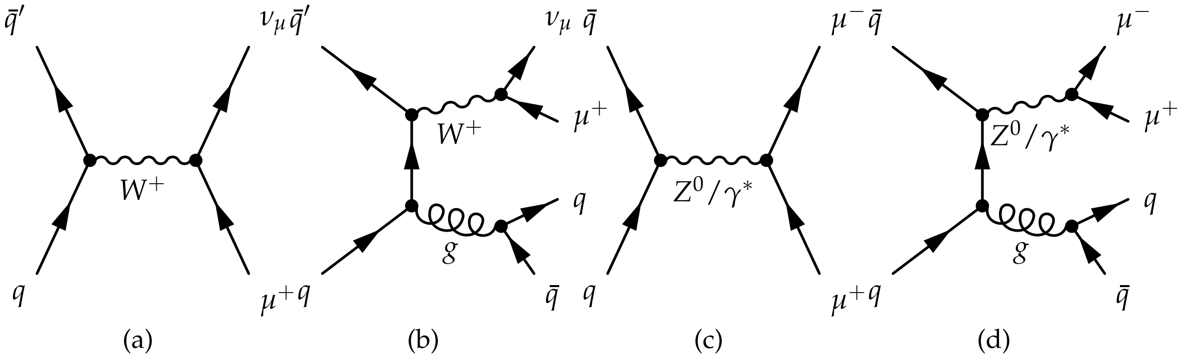

Figure 5.1.: Vector boson production. LO diagrams for the production of W bosons (a) and Z bosons (c) decaying with decays to muons. Exemplary higher order contributions are shown in (b) and (d). Additional jets can lead to similar final states as in *t*-channel single top quark production.

The production of vector bosons, depicted in Fig. 5.1 in addition with gluons, light quarks or heavy quarks is an important background contribution for this analysis.

Table 5.1.: List of utilized Monte Carlo samples. The listed cross sections [146] are given at NNLO precision, except for Diboson production which is given at NLO precision. The first column lists the abbreviated name for the process which is used in the following.

Process	Dataset name	# Events	$\sigma\times$ BR[pb]
t-channel(t)	/TToLeptons_t-channel_8TeV-powheg-tauola/Summer12_DR53X-PU_S10_START53_V7A-v1/AODSIM	3914913	56.4×0.324
t-channel($\bar{t}$)	/TBarToLeptons_t-channel_8TeV-powheg-tauola/Summer12_DR53X-PU_S10_START53_V7A-v1/AODSIM	1711095	30.7×0.324
s-channel(t)	/T_s-channel_TuneZ2star_8TeV-powheg-tauola/Summer12_DR53X-PU_S10_START53_V7A-v1/AODSIM	3932002	3.79×0.324
s-channel($\bar{t}$)	/Tbar_s-channel_TuneZ2star_8TeV-powheg-tauola/Summer12_DR53X-PU_S10_START53_V7A-v1/AODSIM	1999326	1.76×0.324
tW(t)	/T_tW-channel-DR_TuneZ2star_8TeV-powheg-tauola/Summer12_DR53X-PU_S10_START53_V7A-v1/AODSIM	497569	11.1
tW($\bar{t}$)	/Tbar_tW-channel-DR_TuneZ2star_8TeV-powheg-tauola/Summer12_DR53X-PU_S10_START53_V7A-v1/AODSIM	493382	11.1
$t\bar{t}$ semileptonic	/TTJets_SemiLeptMGDecays_8TeV-madgraph/Summer12_DR53X-PU_S10_START53_V7A_ext-v1/AODSIM	86798454	245.8×0.438
$t\bar{t}$ fully leptonic	/TTJets_FullLeptMGDecays_8TeV-madgraph/Summer12_DR53X-PU_S10_START53_V7A-v2/AODSIM	12009320	245.8×0.104
$t\bar{t}$ hadronic	/TTJets_HadronicMGDecays_8TeV-madgraph/Summer12_DR53X-PU_S10_START53_V7A-v1/AODSIM	10515175	245.8×0.456
W+2jets	/W2JetsToLNu_TuneZ2Star_8TeV-madgraph/Summer12_DR53X-PU_S10_START53_V7A-v1/AODSIM	34040035	2159.20
W+3jets	/W2JetsToLNu_TuneZ2Star_8TeV-madgraph/Summer12_DR53X-PU_S10_START53_V7A-v1/AODSIM	15537065	640.40
W+4jets	/W2JetsToLNu_TuneZ2Star_8TeV-madgraph/Summer12_DR53X-PU_S10_START53_V7A-v1/AODSIM	13380573	264.00
Z+jets	/DYJetsToLL_M-50_TuneZ2Star_8TeV-madgraph-tarball/Summer12_DR53X-PU_S10_START53_V7A-v1/AODSIM	30455398	3503.71
Diboson (WW)	/WW_TuneZ2star_8TeV_pythia6_tauola/Summer12_DR53X-PU_S10_START53_V7A-v1/AODSIM	9998866	54.83
Diboson (WZ)	/WZ_TuneZ2star_8TeV_pythia6_tauola/Summer12_DR53X-PU_S10_START53_V7A-v1/AODSIM	9998663	33.21
Diboson (ZZ)	/ZZ_TuneZ2star_8TeV_pythia6_tauola/Summer12_DR53X-PU_S10_START53_V7A-v1/AODSIM	9798339	8.05

The production of W bosons in association with jets is the second most important background process. Events where the W boson decays to $W \to \mu\nu$ or $W \to e\nu$ and is produced in association with a c quark or $b\bar{b}$, $c\bar{c}$ quark pairs can easily be misidentified with single top quark t-channel production. Also W boson production in association with light quark jets can be misidentified since the production cross section times the mistag probability is still larger than the t-channel cross section. LO samples simulated with MADGRAPH are produced separately with different additional parton multiplicities combined to obtain a sample with higher jet multiplicities. Despite correctly describing the process kinematics the heavy flavor component is underestimated by the MADGRAPH simulation as seen by different analyses.

Another, though smaller, background contribution stems from the production of Z bosons in association with jets. In order to have a signal-like final state one of the charged leptons has to be mis-reconstructed which reduces the probability to pass the event selection.

5.2.3. Diboson Production

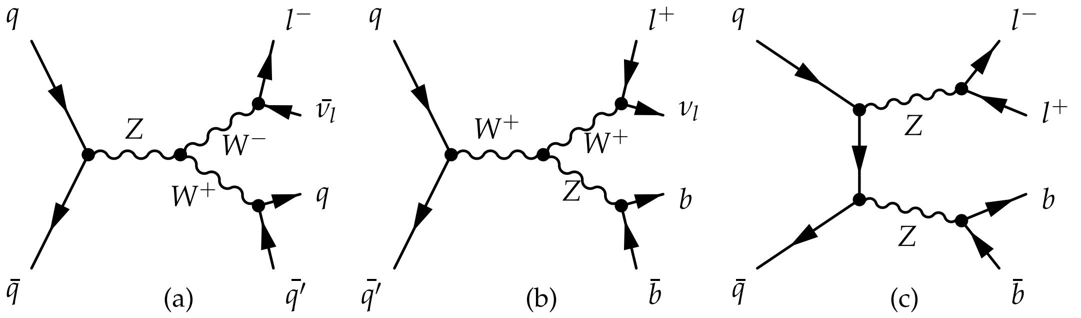

(a) (b) (c)

Figure 5.2.: Diboson production in the WW (a), WZ (b) and ZZ (c) production modes.

Diboson production can occur in the WW, WZ and ZZ modes. The WW and WZ production modes have a charged lepton, neutrino and heavy quarks in the final state. ZZ production can contribute to the background when one charged lepton is not detected. The diboson processes, including all decay channels, are modeled with PYTHIA. Overall, the contribution is nearly negligible.

5.2.4. QCD Multijet Production

The background process with the largest production cross section is the production of multijet events via the strong interaction.

Heavy flavor decay or in-flight decay of pions and kaons can lead to the production of charged leptons. Hadrons reaching the muon chambers are detected as punch-through muons. The available QCD multijet sample simulated with PYTHIA contains too few events after the event selection. Therefore the contribution of this background is estimated from a sideband region in data, see Section 5.4.

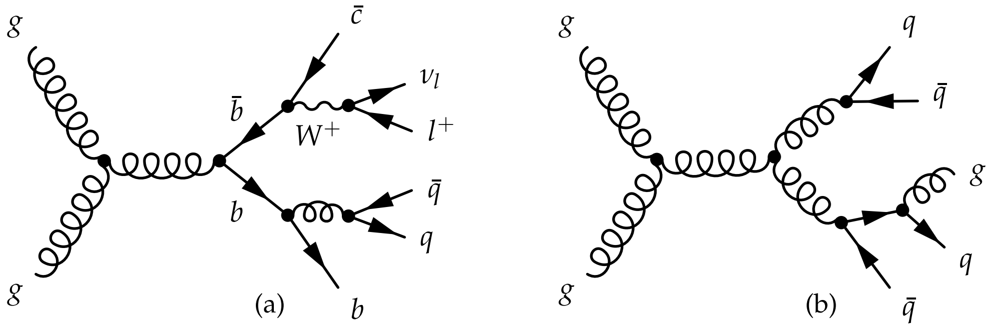

Figure 5.3.: QCD multijet production with same final state as single top t-channel events (a) and with a high energetic jet which can be reconstructed as a fake muon (b).

5.3. Event Selection

The final state of single top t-channel events consist of exactly one charged lepton (muon or electron), missing transverse energy from the W boson decay neutrino, one b-tagged jet stemming from the top-quark decay, as well as a light quark jet produced in forward region. The following event selection implementing the CMS Single Top Quark Group recommendations is applied to both simulated samples and data. The following event selection reduces the number of background events significantly. However, the fraction of background events is still estimated to be 86% (87%) in the muon (electron) channel based on simulation studies. In order to further reduce the number of background events a multivariate approach is chosen as described in Chapter 6.

Event Cleaning

Events with high energetic noise in the HCAL barrel or end caps are rejected with the `HBENoiseFilter` module [147] using pulse shape, hit multiplicity and timing information. Another filter is used to reject beam scraping events.

Trigger Requirements

Events with muons are selected using the High Level Trigger (HLT) path `HLT_IsoMu24_eta2p1` which requires muon candidates with $p_{\mathrm{T}} > 24$ GeV and $|\eta| < 2.1$ during online reconstruction. Reference efficiencies, obtained with "tag&probe" in Z boson decays [148], are applied η-dependent on simulated events to scale the event yield [149]. Electron events are selected using the HLT path `HLT_Ele27_WP80` which requires electron candidates with $E_{\mathrm{T}} > 27$ GeV and tracking identification criteria. The selection efficiency is estimated at 80%.

Primary vertex

Primary vertices are required to be reconstructed with at least four tracks where the track fit has to have at least five degrees of freedom, $n_{DOF} \geq 5$, and a z-distance to the primary vertex of 24 cm, $|z_{PV}| < 24\,\text{cm}$.

Lepton Requirements

Several lepton requirements are applied in order to select real leptons stemming from the W boson decay and not fake leptons produced in QCD multijet events.

Muons

Selected muons are required to have a transverse momentum $p_{\mathrm{T}} > 26\,\text{GeV}$, be within the trigger acceptance range ($|\eta| < 2.1$) and must pass the muon ID. The muon candidates have to fulfill the criteria of "global muons" with an additional set of requirements called *tight muon ID* [111,150].

The Particle Flow relative isolation I_{rel} with "$\Delta\beta$" corrections is defined as follows

$$I_{rel}^{\Delta\beta} = \frac{I^{ch.h} + \max\left((I^{\gamma} + I^{n.h} - I^{PU}), 0\right)}{p_{\mathrm{T}}}, \tag{5.1}$$

where $I^{ch.h}$, I^{γ} and $I^{n.h}$ are the sum of transverse energy deposited by the charged hadrons, photons and neutral hadrons in a cone size of $\Delta R = \sqrt{(\Delta\eta)^2 + (\Delta\phi)^2} = 0.4$ around the direction of the muon. I^{PU} is the sum of transverse momenta of tracks associated with non-leading vertices. A multiplicative factor of 0.5 is applied to take the neutral-to-charged particles ratio expected from isospin invariance into account. Tight muons are required to have a relative isolation of $I_{rel}^{\Delta\beta} < 0.12$.

Electrons

Electrons are required to lie within the tracker acceptance region of $|\eta| < 2.5$ and have transverse energy E_{T} larger than 30 GeV. Electrons with superclusters within the endcap-barrel transition region $1.4442 < \eta_{\mathrm{SC}} < 1.5660$ are rejected. The relative isolation is calculated *Effective area* corrections

$$I_{rel}^{\rho-corr.} = \frac{I^{ch.h} + \max\left((I^{\gamma} + I^{n.h} - \rho \times A), 0\right)}{p_{\mathrm{T}}}, \tag{5.2}$$

where ρ is the average energy of particles not used for the jet reconstruction and A is the area of the jet cone in the $\eta - \phi$ plane. The average energy ρ is calculated with jets reconstructed with the k_{T} algorithm and a distance parameter of 0.6. The relative isolation is required to be $I_{rel}^{\rho-corr.} < 0.1$. Electrons are classified with a multivariate method [151]taking into account variables based on calorimetry and tracking information as well as the pseudorapidity and transverse momentum. The discriminator of this MVA ID is required to be larger than 0.9

A conversion rejection method [152] is applied in order to remove electrons stemming from the conversion of high energetic photons into pairs of electrons.

Loose Lepton Veto

Background processes like the $t\bar{t}$ dilepton channel or Drell-Yan production often have one or more loose leptons not included in the above definitions.

Loose muons need to have a transverse momentum of $p_{\mathrm{T}} > 10\,\mathrm{GeV}$ within the full muon acceptance range $|\eta| < 2.5$, be flagged as global or tracker muons and have a relative isolation of $I_{rel} < 0.2$. The loose electron definition requires a PF electron with $E_{\mathrm{T}} > 20\,\mathrm{GeV}$, $|\eta| < 2.5$ and $I_{rel} < 0.15$ which passes the cut-based veto ID. Events with one or more loose leptons are discarded.

Transverse W boson Momentum and Missing Transverse Energy Requirements

The reconstructed transverse momentum of the W boson is defined as

$$m_{\mathrm{T,W}} = \sqrt{(p_{T,\ell} + p_{T,\nu})^2 - (p_{x,\ell} + p_{x,\nu})^2 - (p_{y,\ell} + p_{y,\nu})^2}\,, \tag{5.3}$$

where $p_{T,\ell}$ and $p_{T,\nu}$ are the transverse momenta of the charged lepton and neutrino which is approximated by $\vec{\not{E}}_{\mathrm{T}}$, respectively. In events with a W boson, the shape of $m_{\mathrm{T,W}}$ is a Jacobian peak at the W boson mass of 80.4 GeV, while in contrast the value of $m_{\mathrm{T,W}}$ in QCD multijet events is distributed along small values. In the muon channel the QCD contribution in the signal region is rejected by requiring $m_{\mathrm{T,W}} > 50$ GeV. In the electron channel the events are required to have $\not{E}_{\mathrm{T}} > 45$ GeV in order to suppress events from QCD multijet production. Studies performed for a different analysis [64] have shown that this variable performs better in the electron channel.

Jet and b-tagging Requirements

Jets are required to have transverse momentum $p_{\mathrm{T}} > 40$ GeV and pseudorapidity $|\eta| < 4.5$. Jet energy corrections are applied like described in Section 3.4.6. PF jets must have more than one constituent, neutral hadronic and neutral electromagnetic energy fractions smaller than 99% and if in the central region a charged electromagnetic fraction smaller than 99% and nonzero charged energy fraction and charged particle multiplicity.

Since the top quark decays to a W boson and b quark, it is crucial to identify those jets stemming from the b quark as described in Section 3.4.6. In this analysis b tagging is performed using the Combined Secondary Vertex (CSV) algorithm at its tight working point ($d_{CSV} > 0.898$) with a defined mistag rate of 0.1%. Two jets with exactly one b-tagged jet are required in the signal region. The $t\bar{t}$ control region requires three jets where exactly two need to be b tagged.

The average number of b quark jets in simulated samples is different than the one observed in data. The b-tagging efficiency ϵ_{data} or ϵ_{MC} is defined as $\epsilon = N_{\text{b-tagged}}/N_{\mathrm{total}}$, where $N_{\text{b-tagged}}$ and N_{total} is the number of b-tagged jets and total number of jets, respectively. In order to correct for this difference the b-tagging object working group provides scale factors for correction of light and heavy flavor jet tagging efficiencies $\mathrm{SF} = \epsilon_{\text{data}}/\epsilon_{\text{MC}}$. These scale factors are applied to simulated samples using a reweighting method [153]. The probability for a given configuration of jets in a simulated sample is

$$P_{\text{MC}} = \prod_{i=\text{tagged}} \epsilon_i \prod_{j=\text{not-tagged}} (1 - \epsilon_j)\,, \tag{5.4}$$

similar for data where the probability is defined as

$$P_{\text{data}} = \prod_{i=\text{tagged}} SF_i \epsilon_i \prod_{j=\text{not-tagged}} (1 - \mathrm{SF}_j \cdot \epsilon_j)\,, \tag{5.5}$$

where ϵ_i is b-tagging efficiency in simulation and SF_i the scale factor, both as functions of the jet flavor (light or heavy flavor), jet-p_{T} and jet-η. The flavor of the jet is determined using tools provided in the software framework. The event weight obtained with these probabilities, $w = P_{\text{Data}}/P_{\text{MC}}$, is used to reweight simulated events.

Signal Event Reconstruction

The top quark decays immediately due to its short lifetime and has to be reconstructed from the decay products. Multiple choices in the reconstruction lead to several possible top quark candidates. In the following the reconstruction of the top quark is described and the probabilities for a correct assignment obtained from simulated data are given.

In order to reconstruct the top quark first the W boson has to be reconstructed which in the scope of this analysis decays to a charged lepton, muon or electron, and the corresponding (anti)-neutrino. Assuming a signal-like final state the transverse components of $\vec{\not{E}}_{\mathrm{T}}$ must stem from the neutrino. The longitudinal momentum of the neutrino, $p_{z,\nu}$, is reconstructed from $\not{E}_{\mathrm{T}}$ and the charged lepton using a W boson mass constraint.

$$M_{\mathrm{W}}^2 = (E_\mu + \sqrt{\vec{\not{E}}_{\mathrm{T}}^{\,2} + p_{z,\nu}^2})^2 - (\mathbf{p}_{\mathrm{T},\mu} + \vec{\not{E}}_{\mathrm{T}})^2 - (p_{z,\mu} + p_{z,\nu})^2\,. \tag{5.6}$$

Solving this equation for $p_{z,\nu}$ leads to two general solutions

$$p_{z,\nu} = \Lambda \frac{p_{z,\ell}}{p_{T,\ell}^2} \pm \frac{1}{p_{T,\ell}^2} \sqrt{\Lambda^2 p_{z,\ell}^2 - p_{T,\ell}^2 (E_\ell^2 \not{E}_{\mathrm{T}}^2 - \Lambda^2)}\,, \tag{5.7}$$

with

$$\Lambda = \frac{m_{\mathrm{W}}^2}{2} p_{\vec{T},\ell} \cdot \vec{\not{p}}_{\mathrm{T}}\,. \tag{5.8}$$

In the case with two real solutions for $p_{z,\nu}$, which happens in 72% of the cases, the solution with the smallest absolute value is chosen. If the discriminant in Eq. (5.8) is negative, which happens in 28% of the cases when the transverse mass m_T is larger than the W boson mass m_W, the solution has an imaginary component. The main cause for this is the finite $\not\!\!E_{\mathrm{T}}$ resolution. Lepton momentum resolution or the finite intrinsic width of the W boson only contribute negligibly. In order to eliminate the imaginary component the neutrino transverse components are modified while the E_{T} vector is kept fixed under the W boson mass constraint of Eq. (5.6). Setting the determinant in Eq. (5.7) to zero yields a quadratic equation in $p_{x,\nu}$ and $p_{y,\nu}$. Setting the W boson mass to the measured mass of 80.4 GeV allows $\vec{\not\!\!E}_{\mathrm{T}}$ to be modified. Assuming that the transverse energy measurement is approximated correctly one can minimize the distance δ between the reconstructed transverse momentum of the neutrino and the missing transverse energy with respect to the solutions $p_{y_{1,2},\nu}$

$$\delta_{1,2}((p_{x,\nu}) = \sqrt{(p_{x,\nu} - (\vec{\not\!\!E}_{\mathrm{T}})_x)^2 + (p_{y_{1,2},\nu} \cdot p_{x,\nu} - (\vec{\not\!\!E}_{\mathrm{T}})_y)^2} \tag{5.9}$$

The smallest solution of $\delta_{1,2}$ is chosen in order to minimize the distance. The new values obtained from this minimization are used to calculate a new value of $p_{z,\nu}$.

The signal event reconstruction has been studied in simulated data in order to estimate the probabilities of matching the correct jets to the required generator level partons. The result are shown in Table 5.2. In the signal region around 84% of the jets can be correctly matched to the top quark.

Table 5.2.: Matching of the reconstructed b-tagged and untagged jets to the underlying final state parton in selected signal events in the muon channel. For the matching, the jet and parton must have a distance $\Delta R < 0.3$.

Assignment	Fraction	2j1t	3j1t
b tagged jet is b-quark jet from top quark		84.04%	64.69%
b tagged jet is spectator b-quark jet		10.58%	21.92%
b tagged jet is the recoiling light quark jet		3.36%	5.65%
b tagged jet is none of the above		2.01%	11.45%
untagged jet is b-quark jet from top quark		7.59%	6.67%
untagged jet is spectator b quark jet		5.07%	9.94%
untagged jet is the recoiling light quark jet		81.2%	62.48%
untagged jet is none of the above		6.18%	21.49%

5.4. Data-driven Estimation of QCD Multijet Background

All processes except QCD multijet production are modeled using simulated samples. The available simulated QCD multijet sample is generated for general usage and a large phase space, only few events pass the event selection described previously. The large cross section allow to model QCD multijet production directly from data. This is accomplished with a modified event selection which enriches the selected sample with QCD multijet events. This enriched dataset is then used to estimate the fraction and modeling of QCD multijet events of the signal region.

Templates for QCD multijet distributions are obtained in the QCD enriched sidebands separately for the *2j1t* and *3j2t* regions by inverting the isolation criteria for muons and electrons. The relative isolation of leptons is required to lie between $0.3 < I_{rel} < 0.5$. In order not to bias the modeling of variables a good separation between jets and leptons is required and only jets with a distance of $\Delta R(\text{jet}, \ell) > 0.3$ from leptons are selected. The estimation of the number of QCD multijet events is performed in two sensitive variables, $m_{\mathrm{T,W}}$ in the muon channel and $\not{E}_{\mathrm{T}}$ in the electron channel. The contamination from non-QCD multijet events in the anti-isolated regions is estimated with simulated samples and is below 1.5% in the *2j1t* region for both channels before the cuts on $m_{\mathrm{T,W}}$ and $\not{E}_{\mathrm{T}}$. The purity of the sideband selection in the signal region is shown in Fig. 5.4. The contamination in the $\mathrm{t\bar{t}}$ control region is higher, however QCD multijet events are negligible in this region due to two required b-tagged jets. In general the distribution F of a kinematic variable x can be parametrized as

$$F(x) = a \cdot S(x) + b \cdot B_1(x) + c \cdot B_2(x)\,, \tag{5.10}$$

where $S(x)$ and $B_{1,2}(x)$ are the expected distributions of signal and background processes and x is either the transverse mass of the W boson $m_{\mathrm{T,W}}$ in the muon channel or the missing transverse energy in the electron channel. In this case $S(x)$ refers to the amount of QCD events derived from data as described above. Backgrounds containing a real W boson in the hard interaction are added up to the template $B_1(x)$, whereas the template $B_2(x)$ consists of Z boson events in association with jets. Due to the similarity with QCD events this background contribution is fixed to prediction. The normalization constants a and b are determined by a fit of $F(x)$. The fit is performed in the region of $m_{\mathrm{T,W}}$ ($\not{E}_{\mathrm{T}}$) defined by $m_{\mathrm{T,W}} < 50\,\mathrm{GeV}$ in the muon channel and $\not{E}_{\mathrm{T}} < 45\,\mathrm{GeV}$ in the electron channel and extrapolated to the signal region. The data-driven templates for QCD multijet events and the simulated samples used in the fit are shown in Fig. 5.5 for the signal region and in Fig. 5.6 for the $\mathrm{t\bar{t}}$ control region. The number of QCD multijet events estimated with the fit are given in Table 5.3.

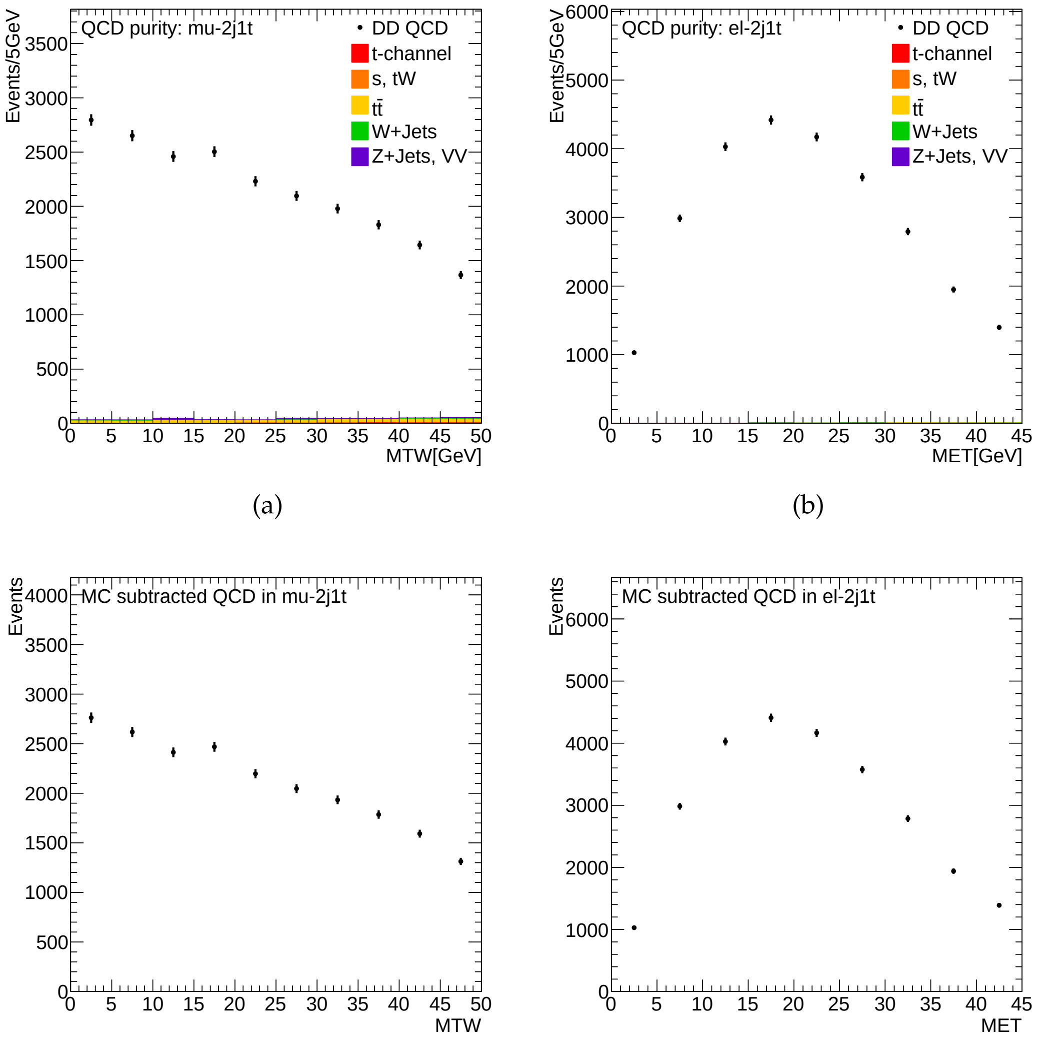

(a) (b)

(c) (d)

Figure 5.4.: Purity of the QCD multijet sideband selection in muon (a) and electron (b) channel. Non-QCD processes are simulated and normalized to their predicted cross section and the assumed luminosity. Due to the small amount of no visible difference is observed in templates with subtracted non-QCD processes in the muon (c) and electron (d) channel.

Table 5.3.: Estimation of QCD multijet events in the signal and $t\bar{t}$ control region for the muon and the electron channel. The quoted uncertainties are statistical uncertainties.

Muon Channel	Events	Electron channel	Events
2j1t region			
$m_{\mathrm{T,W}} < 50\,\mathrm{GeV}$	21554±614	$\not\!\!E_{\mathrm{T}} < 45\,\mathrm{GeV}$	26359±551
$m_{\mathrm{T,W}} > 50\,\mathrm{GeV}$	5448±173	$\not\!\!E_{\mathrm{T}} > 45\,\mathrm{GeV}$	2793±93
3j2t region			
$m_{\mathrm{T,W}} < 50\,\mathrm{GeV}$	133±228	$\not\!\!E_{\mathrm{T}} < 45\,\mathrm{GeV}$	580±14
$m_{\mathrm{T,W}} > 50\,\mathrm{GeV}$	160±273	$\not\!\!E_{\mathrm{T}} > 45\,\mathrm{GeV}$	117±41

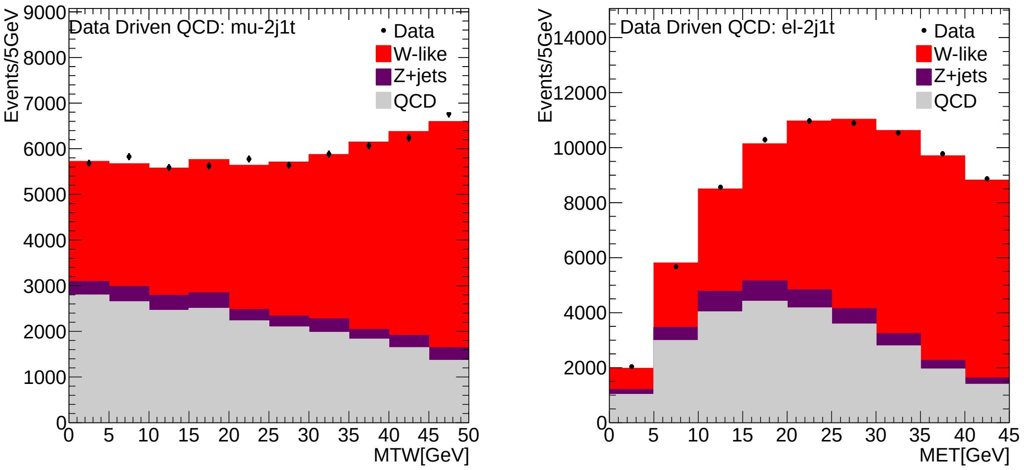

(a) (b)

Figure 5.5.: QCD multijet sideband and non-QCD templates, normalized to the fit results, for the 2j1t region.

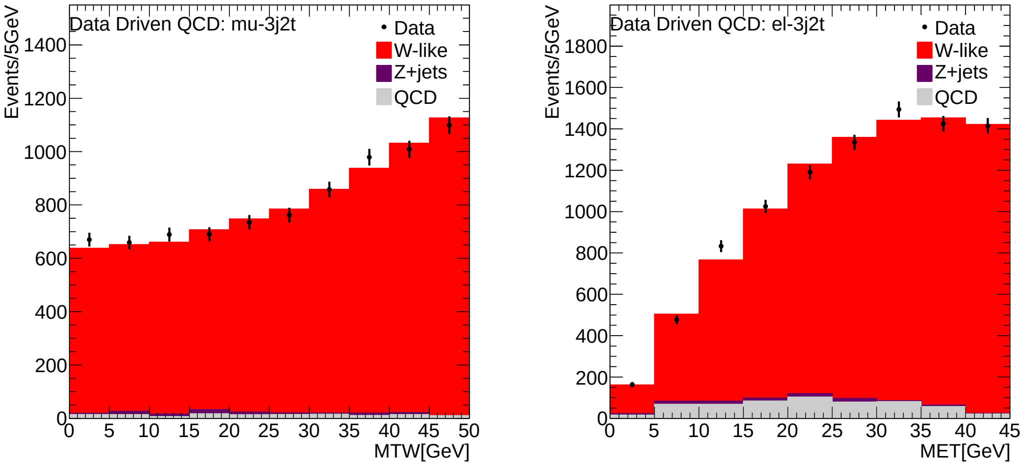

(a)

(b)

Figure 5.6.: QCD multijet sideband non-QCD templates, normalized to the fit results, for the 3j2t region.

6. Multivariate Neural Network Analysis

After applying the event selection described in Chapter 5 the dataset is still dominated by background events and the signal to background ratio is much lower than in a comparable $t\bar{t}$ analysis. In order to further enrich the signal, a multivariate analysis (MVA) method is utilized. The most common MVA methods usually employed in particle physics are artificial neural networks (NN), boosted decision trees (BDT) or likelihood functions (LF). This analysis uses an NN implemented with the NeuroBayes package [154, 155].

6.1. Theory of Neural Networks

Artificial neural networks are mathematical models for pattern recognition inspired by neural pathways in the central nervous systems of animals [156]. The nodes of a neural network, analog to neurons, are ordered in different layers and are connected to each other by weighted connections, similar to synapses. Neural networks are nonlinear functions of linear input functions, making them powerful statistical tools for regression and classification when some precautions are taken. A comprehensive introduction to neural networks can be found in Ref. [157].

The first presented and most simple of these models, the perceptron [158], was not very powerful and could not approximate the XOR function [159]. Multilayer perceptrons overcome this limitation by introducing one or more additional layers, the hidden layers, and non-linear activation functions. Usually these networks are feed-forward, i.e with connections in one layer only connecting in one direction to the next layer. These networks can be trained with historical or simulated data by adapting the weights according to the difference between predicted and true value. If the weight between two nodes becomes too small the connection can be pruned. Through supervised learning, these networks can learn almost any non-linear dependence. Feed-forward networks with at least one hidden layer and a suitable activation function, e.g. a sigmoid (shown in Fig. 6.1), can approximate any continuous function with arbitrary precision as shown by the universal approximation theorem [160, 161]. A neural network can be imagined as a mapping from k input units to l output units, $\mathbb{R}^k \rightarrow \mathbb{R}^l$. A representation of a feed-forward neural network, without bias nodes, is shown in Fig. 6.2.

The first layer consists of the input nodes which take the values of the individual preprocessed input variables. The input for a node j in the hidden layer is a biased weighted sum of the values of the input nodes:

$$h_j(x) = \sum_i w_{ij} x_i + \mu_{0,j} \,, \tag{6.1}$$

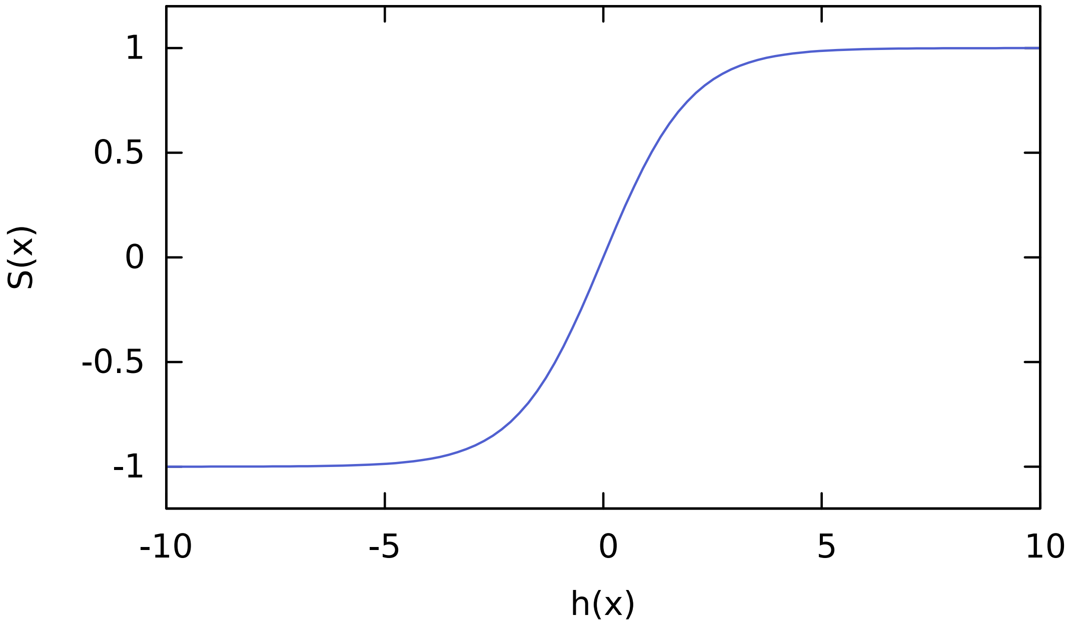

Figure 6.1.: Logistic sigmoid function, Eq. (6.2), in the interval $[-10, 10]$.

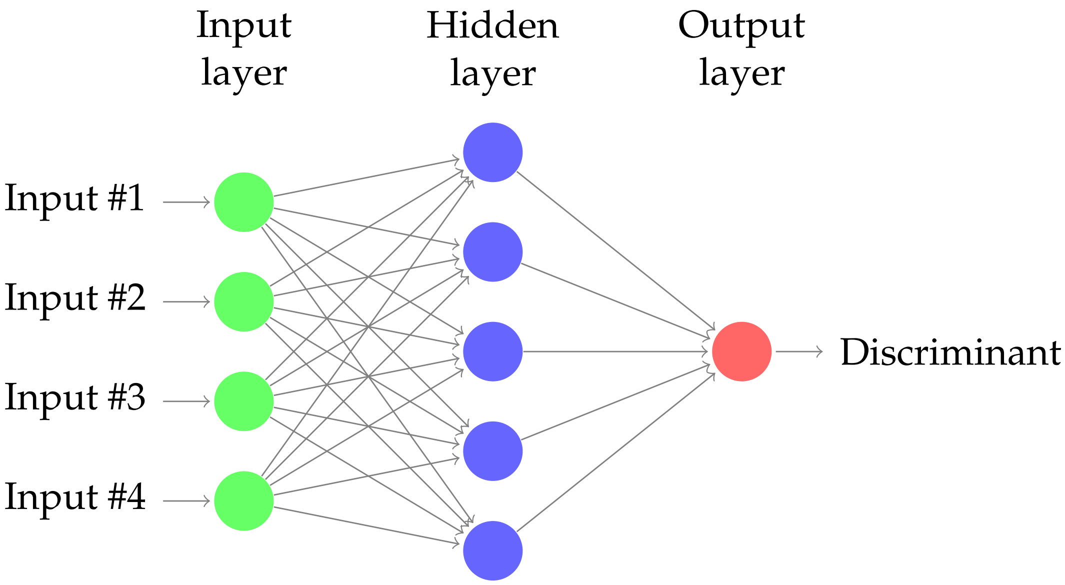

Figure 6.2.: Representation of a feed-forward neural network with three layers and one output node. Nodes in one layer are only connected to the next layer. The bias nodes are not depicted.

where x_i is the input data of node i, w_{ij} the weight between the nodes i and j, and $\mu_{0,j}$ the weight between the node j and the bias node in the input layer which acts as a threshold of the node j. Visualized geometrically, the weights span a decision boundary separating signal and background in an n-dimensional hyperplane with an offset from the bias nodes.

A transfer function $S(x)$ maps the output from $(-\infty, \infty)$ to the interval $[-1, 1]$.

$$S(x) = \frac{2}{1 + e^{-h(x)}} - 1. \tag{6.2}$$

The logistic sigmoid function given in Eq. (6.2) is depicted in Fig. 6.1. This function is only sensitive in a small region around zero, for very large or small values it reaches saturation. Therefore the weighted sum of input values $\sum_i w_{ij} x_i$ is shifted to the linear region of the transfer function by the weight of the bias node.

The final output of the neural network is thus calculated as follows

$$o = S\left(\sum_j^M \omega_j \cdot S(\sum_i^N \omega_{ij} x_i + \mu_0)\right) . \tag{6.3}$$

In order to train the network, a cost or *error function* is defined for the network output comparing the current output o_i to the expected output T_i. The most commonly used error function for regression is the quadratic error function

$$E_D = \frac{1}{2N} \sum_i^N (o_i - T_i)^2 . \tag{6.4}$$

In some cases, like classification which is used in the following, it is more common to use the entropy error function, which is defined as

$$E_D = \frac{1}{N} \sum_i^N \log\left(\frac{1}{2}(1 + T_i \cdot o_i + \epsilon)\right) , \tag{6.5}$$

where N is the number of training events and T_i is a binary target value used to classify an event i as either signal or background. The regularization constant ϵ is introduced to avoid numerical problems at the start of the training. A small value is chosen at the beginning which is reduced in each training iteration until it reaches zero after the first few iterations.

The minimization of the error problem is non-trivial since the global minimum in a multi-dimensional space has to be found without getting stuck in local minima. Usually, a gradient descent method is used where the change of each weight ω_{ij} is proportional to the gradient of the error function $\delta\omega_{ij} = -\eta \frac{\partial E_D}{\partial \delta\omega_{ij}}$. The step width η is varied individually for each weight during the training. NeuroBayes has the option to use the Broyden-Fletcher-Goldfarb-Shanno (BFGS) [162–165] algorithm which converges much faster than a simple gradient descent. The BFGS algorithm is a Quasi-Newton method which approximates the Hessian matrix used in the gradient descent, consisting of the second partial derivatives, by iteratively approximating it with the gradient and rank-one updates.

The change of each weight is calculated through backpropagation in [166]. The aim of backpropagation is to calculate the partial derivative recursively. The error for each weight is propagated back to the hidden layer from the output node and to the input layer from the hidden layer by applying the chain rule of the partial derivative. One assumption for backpropagation is, that the total error function is the average of individual training samples. This allows to calculate the individual partial average for one sample by using the partial derivative of the average error function. A pedagogical description of backpropagation is available in [167].

Preprocessing and Regularization

Since the various different input variable distributions have different scales the input variables have to be preprocessed before being fed to the neural network. NeuroBayes automatically preprocesses the input training and uses several techniques like spline fits and Bayesian regularization to prevent the network from learning statistical fluctuations and overtraining. Overtraining can occur if too many hidden nodes are used and the network starts to learn random noise in the used training sample and does not generalize. This can be checked by splitting the input sample into a training and validation sample. An illustration of an overtrained network is shown in Fig. 6.3.

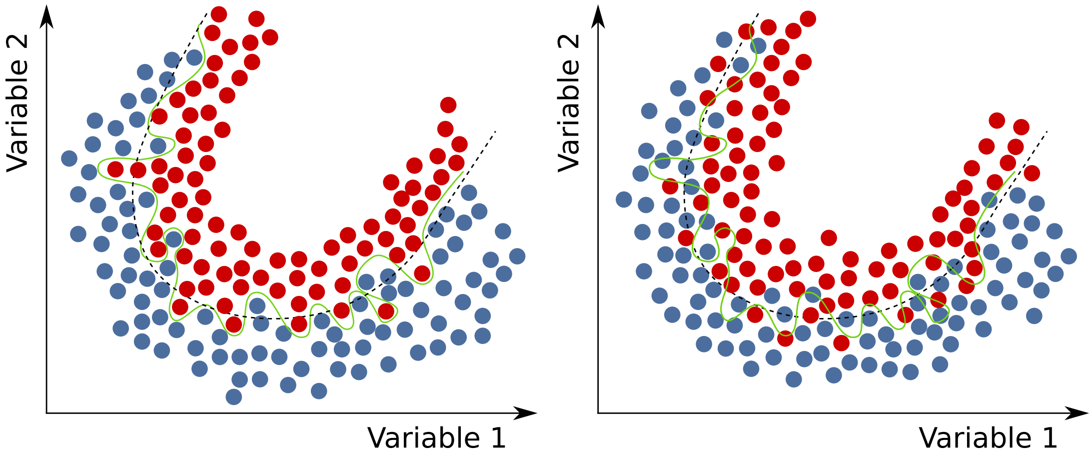

Figure 6.3.: Visualization of overtraining. Two-dimensional representation of signal (red) and background (blue) events. The dashed line represents the optimal decision boundary for both the training and validation data. The green line shows the overtrained decision boundary. The diagram on the left shows an overtrained network on the training data. If this network is applied on the validation sample (right), background events within the green line would be wrongly classified as signal [168].

Before the training, the input variables are preprocessed to facilitate an optimal network training. The input variables are first flattened into bins with equal bin content in the interval $[-1, 1]$ in order to reduce the effect of outliers. All input variables can then be transformed, e.g. to follow a normal distribution with mean zero and width one so that all inputs to the hidden layer nodes have the same scale and the output of the hidden layer is not saturated. Another option is to use a spline fit in order to smoothen the distribution.

After the transformation, the variables are decorrelated by diagonalizing the covariance matrix of the transformed variables through iterative Jacobian rotations. During the training, the weights are regularized by a Bayesian regularization method. Three regularization classes are used for the weights of the input layer, hidden layer and the output layer [169].

6.2. Selection of Input Variables

Many possible variables, some of them already successfully used for the single top quark observation at CDF [170], have been tested for their separation power. In addition, their data to simulation agreement in the W+light enriched sideband region has been checked. Out of these variables, 21 were found to be suitable for the NN training. The training has been performed separately for the muon and electron channel.

The input variables used for the NN training are:

1. Pseudorapidity of the light quark jet, η_{lq}: The pseudorapidity η of the light quark jet is the most discriminating variable in the training. For the single top t-channel process, the light quark jet is mostly detected in the forward region, while for all background processes it is detected in the central region of the detector.

2. Transverse momentum of light quark, $p_{\mathrm{T,lq}}$: The transverse momentum of the jet assigned to the light quark.

3. Mass of light quark, m_{lq}: The invariant mass of the jet assigned to the quark recoiling against the intermediate W boson produced in the t-channel.

4. Mass of first leading jet, m_{jet1}: The invariant mass of the jet with the highest transverse momentum p_{T}.

5. Mass of second leading jet, m_{jet2}: The mass of the second leading (ordered in terms of decreasing transverse momentum) jet present in the event.

6. Invariant di-jet mass, $m_{\mathrm{jet1,jet2}}$: The invariant mass of the two selected jets can discriminate between signal and background due to the longer tail of the signal. In case of more than two jets, the two leading jets, ordered in decreasing jet-p_{T}, are used for the calculation of this variable.

7. Reconstructed top quark mass, $m_{\ell\nu\mathrm{b}}$: The invariant mass of the top quark reconstructed from the four-vectors of the charged lepton, the neutrino, and the jet assigned to the b quark from the top-quark decay. The peak around 173 GeV is

a clear indication for the production of top quarks. The peak is broadened for $t\bar{t}$ production compared to single top t-channel production. The reason for this is, that in half of the cases, the selected b quark is not coming from the same top quark as the selected muon. Also, if the two W bosons decay leptonically, there are two neutrinos which contribute to the missing transverse energy. Contributions from W bosons and light or heavy flavor jets do not peak at the top-quark mass and have a longer tail.

8. Mass of the b quark from the top-quark decay, $m_{b_{top}}$: The invariant mass of the jet assigned to the b quark from the top-quark decay.
9. Transverse mass of the W boson, $m_{\mathrm{T,W}}$: The transverse mass of the W boson obtained from the isolated charged lepton and the missing transverse energy.
10. Missing transverse energy, $\not{E}_{\mathrm{T}}$: The energy associated to the undetected neutrino present in the final state of single-top-quark production.
11. Lepton charge, Q_{ℓ}: The charge of the selected isolated lepton in the event.
12. Pseudorapidity of the W boson, η_{W}: The pseudorapidity of the W boson stemming from the decay of the top quark.
13. Difference in ϕ between the lepton and the light jet, $\Delta\phi[\ell, lq]$: $\Delta\phi[l, lq]$ is defined as the difference of the azimuthal angle between the four vector of the isolated lepton and the four-vector of the light quark jet.
14. Difference in ϕ between the second leading jet and the charged lepton, $\Delta\phi[jet2, \ell]$: Difference of the azimuthal angle of the four vector of the second leading jet and the four vector of the lepton.
15. Azimuthal angle of $\vec{\not{E}}_{\mathrm{T}}$, $\phi_{\not{E}_{\mathrm{T}}}$: The azimuthal angle of the $\not{E}_{\mathrm{T}}$ vector.
16. Difference in ϕ between the leading jet and $\vec{\not{E}}_{\mathrm{T}}$, $\Delta\phi[jet1, \not{E}_{\mathrm{T}}]$: The difference in the azimuthal angle between the four-vector of the leading jet and $\vec{\not{E}}_{\mathrm{T}}$.
17. Difference in ϕ between the second leading jet and $\vec{\not{E}}_{\mathrm{T}}$, $\Delta\phi[jet2, \not{E}_{\mathrm{T}}]$: The difference between the azimuthal angle of second leading jet and $\vec{\not{E}}_{\mathrm{T}}$.
18. Angular separation of first jet and $\vec{\not{E}}_{\mathrm{T}}$, $\Delta R[jet1, \not{E}_{\mathrm{T}}]$: The angular separation between the four-vector of the first jet and $\vec{\not{E}}_{\mathrm{T}}$.
19. Event shape variable, C: The C-parameter is derived from the eigenvalues λ_i of the momentum tensor:

$$C = 3 \times (\lambda_1\lambda_2 + \lambda_2\lambda_3 + \lambda_3\lambda_1)$$

20. Event shape variable, D: The D-parameter is defined by the eigenvalues λ_i of the momentum tensor:

$$D = 27(\lambda_1\lambda_2\lambda_3)$$

21. Event shape variable, A: The aplanarity A is calculated from the third largest eigenvalue of the momentum tensor:

$$A = \tfrac{3}{2}(\lambda_3)$$

See Appendix B for a more detailed description of the event shape variables.

As an example, the two most important variables in the network training, the light quark jet pseudorapidity η_{lq} and the reconstructed top quark mass $m_{\ell\nu\mathrm{b}}$, are shown in the "2j1t" category for both the muon channel, see Fig. 6.4, and electron channel, see Fig. 6.5. The distributions for all input variables can be found in Appendix C.

6.3. Neural Network Training

The NN is trained in the "2j1t" category separately for the muon and electron channel and applied to both the signal and control regions. The discriminator outputs in the control regions are used to check the modeling of the backgrounds and validity of the training. The $\mathrm{t\bar{t}}$ control region is later used in the fit to constrain the $\mathrm{t\bar{t}}$ contribution in the signal region. The training of the neural network is performed with a limited memory implementation of the BFGS algorithm [171], a quasi-Newton method which iteratively approximates the Hessian matrix of the second derivatives in order to minimize the error function. With this option the training converges after a few iterations.

During the training, connections with insignificant weights are removed. Pruning avoids learning unimportant information and thus helps against overtraining.

The training sample consists of the signal t-channel sample and the most important MC samples, $\mathrm{t\bar{t}}$ and W+jets. 70% of the events are used for the training, the rest is used as a test sample to check for overtraining.

After the variables have been preprocessed the correlation matrix of the N input variables and the total correlation to the signal target are calculated. One variable after another is removed and the correlation to the target is computed again. The variable with the least loss of correlation is removed and the procedure is repeated until the most significant variable remains. The ranking is given in terms of significance, which is equal to the loss of correlation multiplied by $\sqrt{n}$, where n is the sample size. The ranking of the input variables in the NN training is listed in Table 6.1 for the muon channel and in Table 6.2 for the electron channel. The training is only taking variables into account with an additional significance larger than 3σ. Variables with less than 3σ have not been considered and do not affect the NN training. The linear correlation (Pearson [172]) between the input variables themselves and the target variable is shown in Fig. 6.6 for the muon and electron channel, separately.

After the training a good separation between background and signal is achieved, as can be seen in Fig. 6.7. Backgrounds peak at low discriminator values near -1, while the signal peaks at high discriminator values near $+1$.

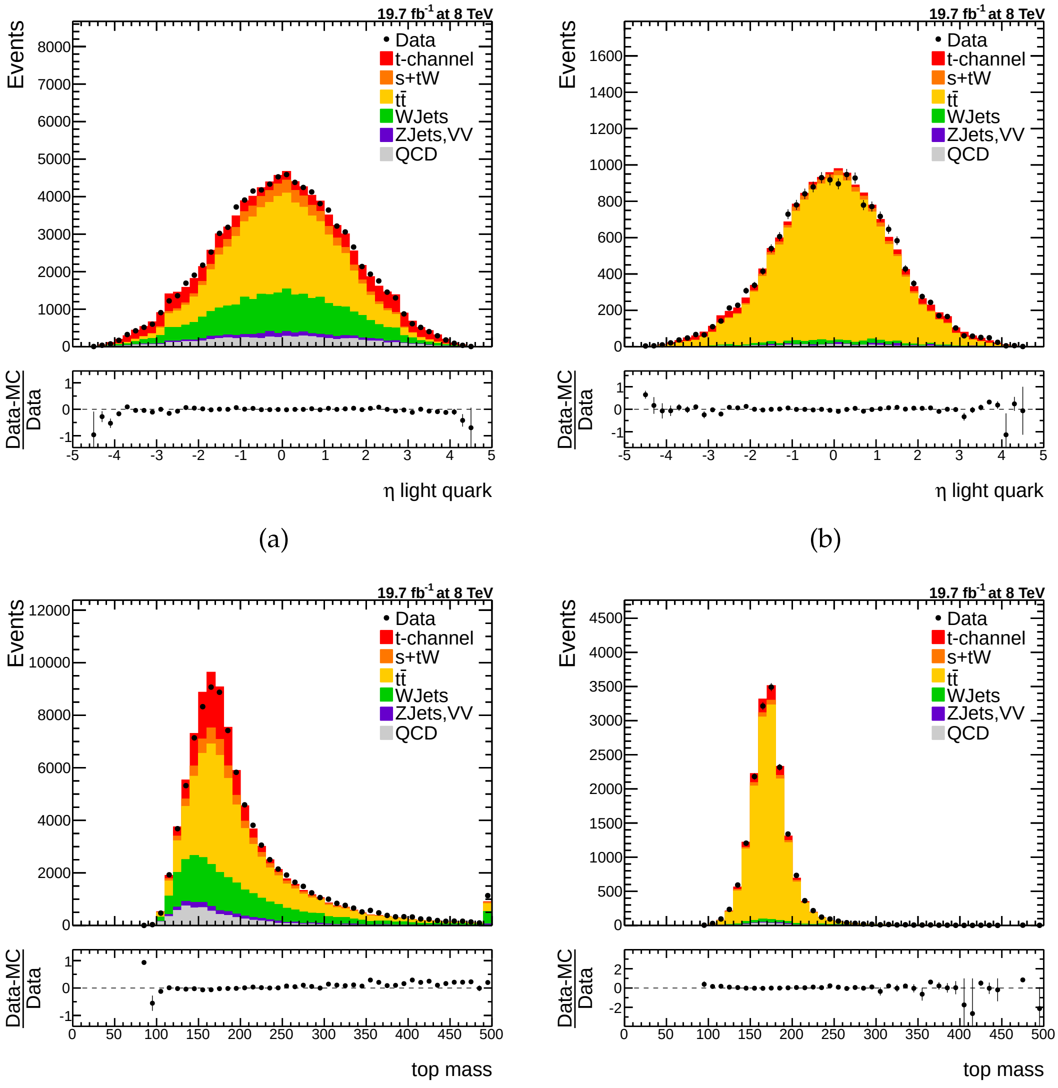

(a) (b)

(c) (d)

Figure 6.4.: Two of the most important input variables for the network training in the muon channel signal region (left), η_{lq} (a) and $m_{\ell\nu\mathrm{b}}$ (c), and $\mathrm{t\bar{t}}$ control region (right), η_{lq} (b) and $m_{\ell\nu\mathrm{b}}$ (d).

The purity of a network output o is defined as

$$P(o) = \frac{N_{sig}}{N_{sig} + N_{bkg}}\,, \tag{6.6}$$

where N_{sig} and N_{bkg} are the number of signal and background events. The network output should be proportional to the purity P, which can be seen in Fig. 6.8. The signal

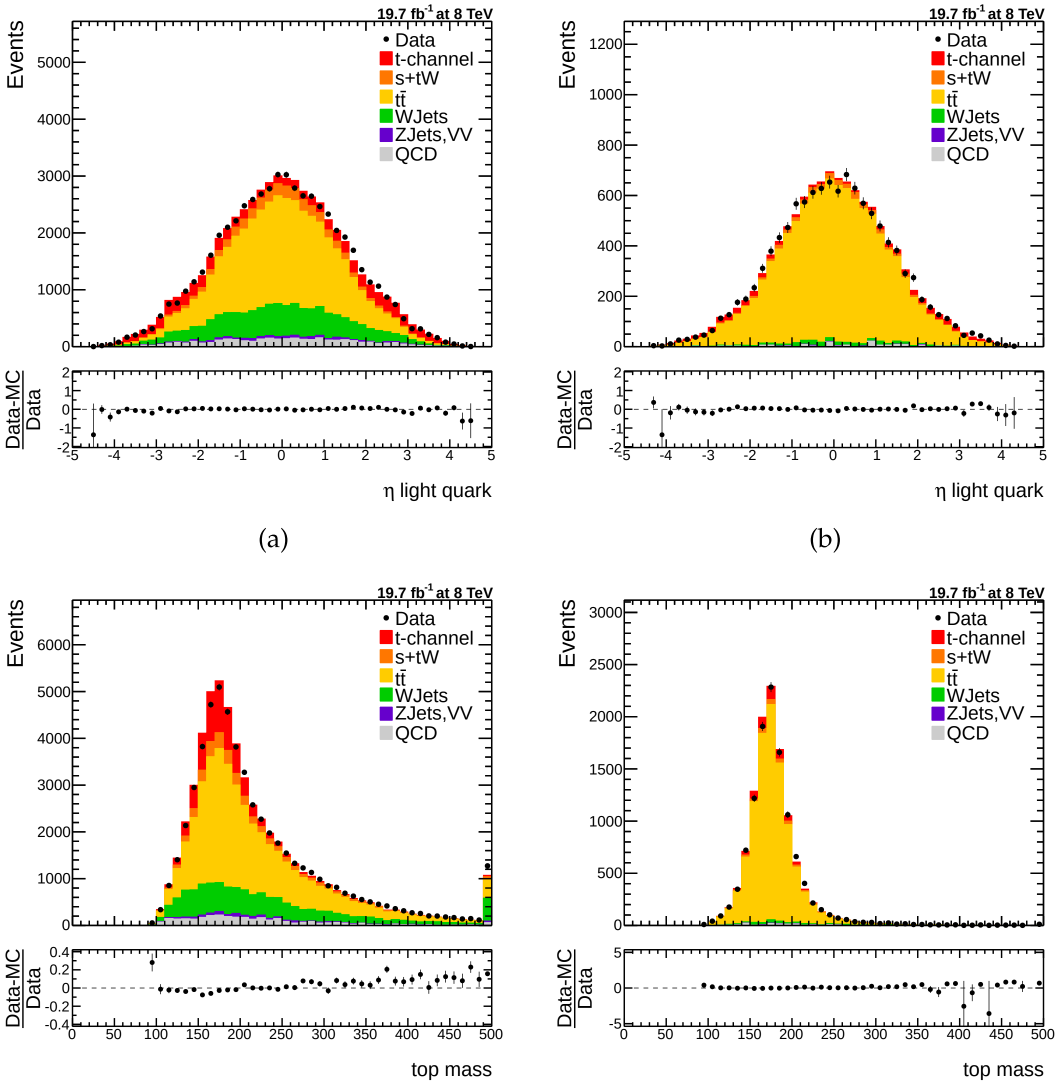

(a) (b)

(c) (d)

Figure 6.5.: Two of the most important input variables for the network training in the electron channel signal region (left), η_{lq} (a) and $m_{\ell\nu\mathrm{b}}$ (c), and $t\bar{t}$ control region (right), η_{lq} (b) and $m_{\ell\nu\mathrm{b}}$ (d).

purity versus the signal efficiency is shown in Fig. 6.9 for several discriminator cut values. The upper curve depicts the purity-efficiency above a certain cut, the lower curve for values below a certain cut value. The resulting neural network discriminator output is shown in Fig. 6.10 for the "2j1t" region and in Fig. 6.11 for the "3j2t" $t\bar{t}$ control region for both muon and electron channel.

Table 6.1.: Input variables ranked by relevance for the neural network discriminator performance in the muon channel.

Rank	Add. sig	This var.	loss-removed	Global corr. to others [%]	Variable
1	195.30	195.30	52.32	84.8	η_{lq}
2	103.59	133.41	91.84	40.8	$m_{\ell\nu\mathrm{b}}$
3	82.07	157.99	66.42	74.8	$m_{\mathrm{jet1,jet2}}$
4	64.09	83.69	54.36	28.7	$m_{\mathrm{T,W}}$
5	31.64	56.13	31.21	11.6	Q_{ℓ}
6	27.26	19.62	14.84	82.9	m_{lq}
7	22.95	13.32	23.72	29.1	η_{W}
8	20.51	43.73	23.03	32.3	$\Delta\phi[\ell, lq]$
9	20.81	50.54	6.24	78.9	$m_{b_{top}}$
10	17.24	12.00	13.63	65.7	$\Delta\phi[jet1, \not{E}_{\mathrm{T}}]$
11	14.05	180.49	10.43	97.9	C
12	11.32	15.91	13.66	77.0	$p_{T,lq}$
13	9.02	163.61	4.90	99.3	D
14	8.81	43.55	9.30	85.3	m_{jet1}
15	7.05	52.46	8.39	45.5	$\not{E}_{\mathrm{T}}$
16	6.82	15.45	6.74	55.6	$\Delta\phi[jet2, \not{E}_{\mathrm{T}}]$
17	5.85	15.47	5.58	70.2	m_{jet2}
18	5.03	105.89	5.11	68.2	$\Delta R[jet1, \not{E}_{\mathrm{T}}]$
19	1.80	131.98	1.82	97.7	Aplanarity A
20	1.29	1.38	1.29	0.9	$\phi_{\not{E}_{\mathrm{T}}}$
21	0.58	9.70	0.58	45.7	$\Delta\phi[jet2, \ell]$

Table 6.2.: Input variables ranked by relevance for the neural network discriminator performance in the electron channel.

Rank	Add sig.	This var.	loss-removed	Global.corr to others [%]	Variable
1	158.23	158.23	40.82	84.1	η_{lq}
2	90.63	116.65	71.27	51.8	$m_{\ell\nu\mathrm{b}}$
3	68.35	127.98	57.64	74.6	$m_{\mathrm{jet1,jet2}}$
4	59.65	79.12	52.73	30.2	$m_{\mathrm{T,W}}$
5	25.99	43.00	12.33	86.6	m_{jet1}
6	24.65	44.64	24.03	11.7	Q_{ℓ}
7	22.60	5.38	22.15	33.4	η_{W}
8	14.04	18.89	8.52	76.5	m_{jet2}
9	13.81	21.51	17.10	74.3	$p_{T,lq}$
10	10.39	1.30	12.65	48.4	$\Delta\phi[jet2,\ell]$
11	12.21	23.94	12.44	45.9	$\Delta\phi[\ell,lq]$
12	9.93	146.40	10.06	97.6	C
13	6.92	10.42	7.51	83.1	m_{lq}
14	6.38	52.21	8.09	49.7	$\not{E}_{\mathrm{T}}$
15	6.44	101.17	6.48	68.7	$\Delta R[jet1,\not{E}_{\mathrm{T}}]$
16	6.57	22.92	6.70	49.1	$\Delta\phi[jet2,\not{E}_{\mathrm{T}}]$
17	4.18	131.13	7.47	99.1	D
18	6.37	103.81	6.17	97.2	Aplanarity A
19	2.80	7.03	2.82	36.4	$\Delta\phi[jet1,\not{E}_{\mathrm{T}}]$
20	2.22	54.44	2.22	84.0	$m_{b_{top}}$
21	0.87	3.55	0.87	1.7	$\phi\not{E}_{\mathrm{T}}$

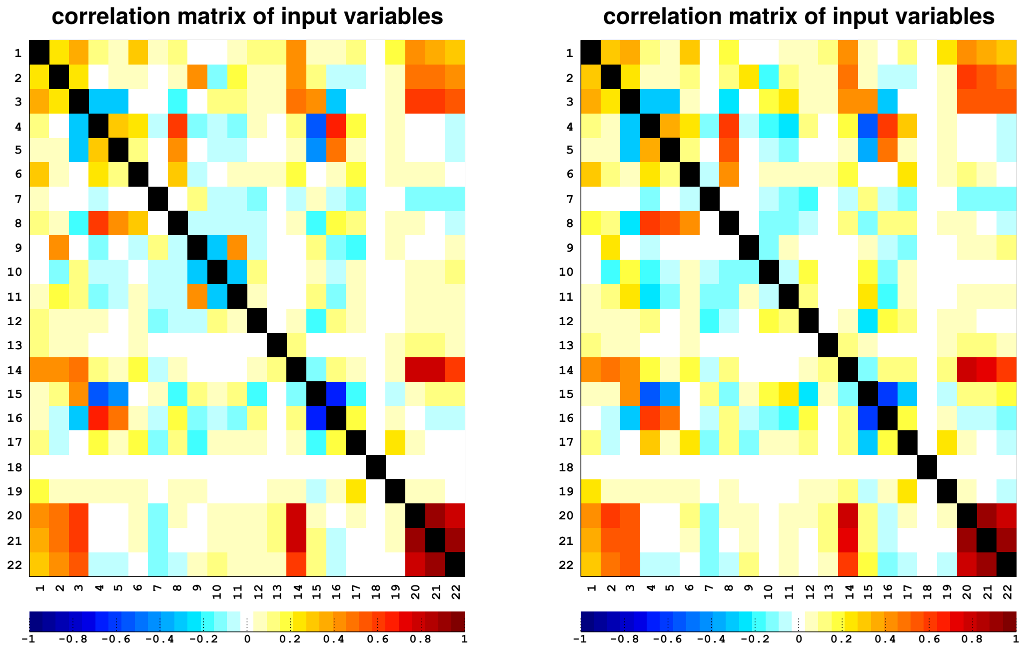

Figure 6.6.: Correlations between the input variables of the NN in the muon channel (left) and the electron channel (right). The target variable is entry 1, entries 2 to 22 correspond to the 21 input variables in the ranking order of tables 6.1 and 6.2 (Entry number = rank +1).

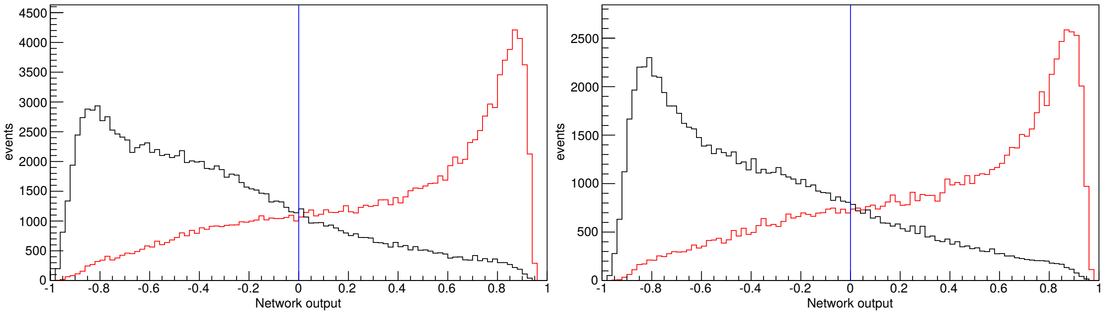

Figure 6.7.: Shapes of the discriminators of the neural network for training events. The network is able to discriminate signal (red) and background (black) events for both the muon (left) and electron (right) channel.

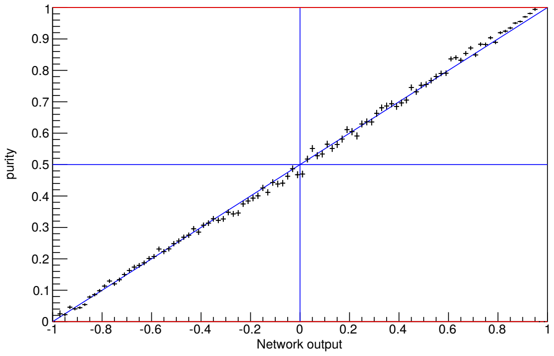

Figure 6.8.: Purity for different cuts on the network discriminator for the muon (left) and electron (right) channel. The purity is proportional to the network discriminator.

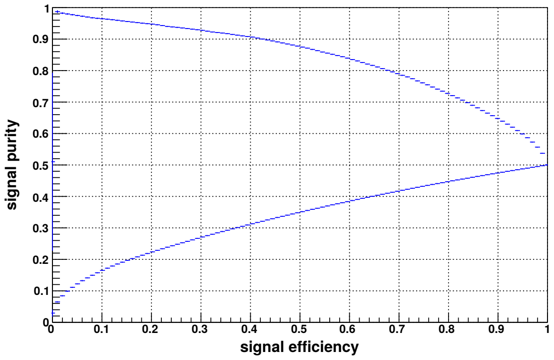

Figure 6.9.: Purity-efficiency plot for different cuts on the network discriminator for the muon (left) and electron (right) channel. The upper curve depicts the purity-efficiency above a certain cut, the lower curve for values below a certain cut value.

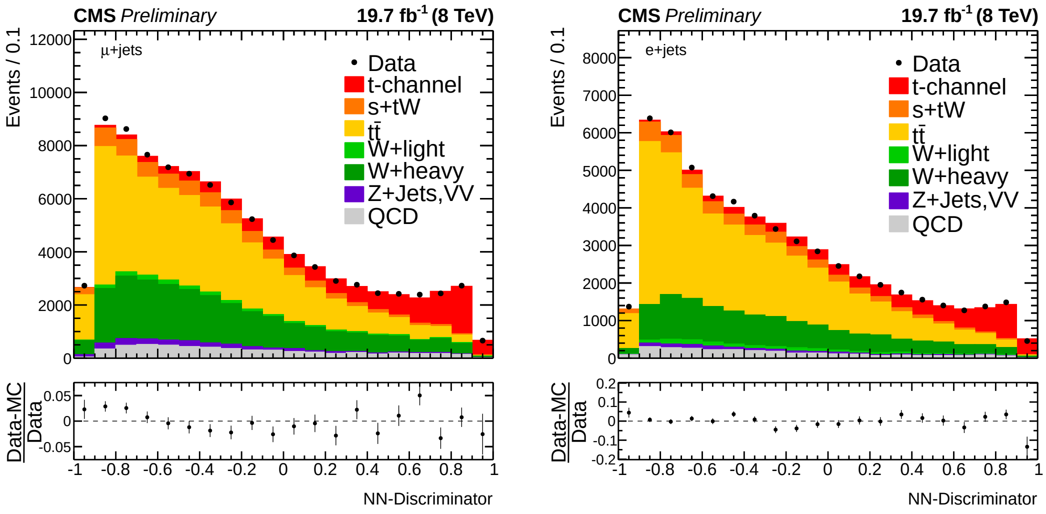

(a)

(b)

Figure 6.10.: Neural network discriminator in the signal region (2j1t) for the muon (a) and electron (b) channel.

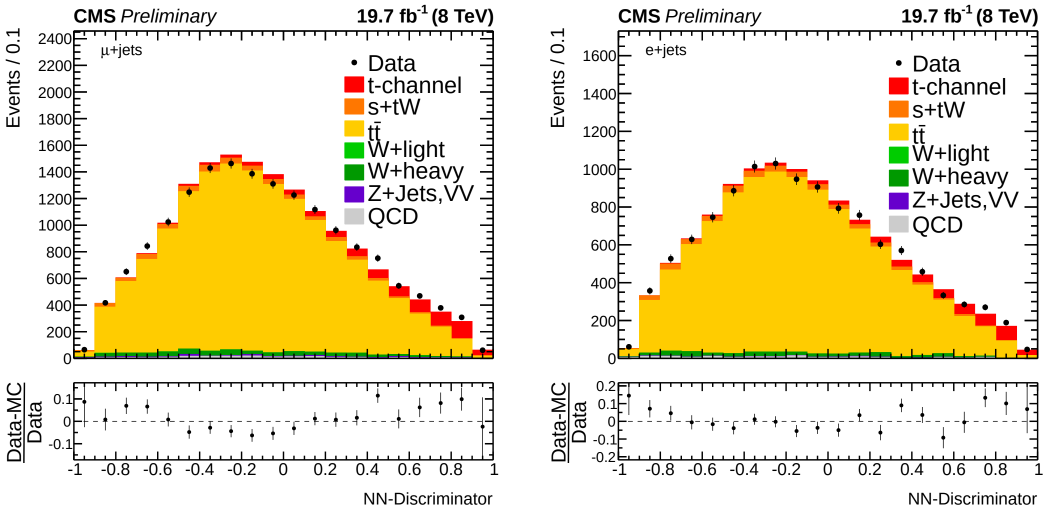

(a)

(b)

Figure 6.11.: Neural network discriminator in the $t\bar{t}$ control region (3j2t) for the muon (a) and electron (b) channel.

6.4. Estimation of Optimal Cut Values

In order to get a signal enriched sample, a cut on the NN discriminator is applied. The optimal cut value is determined on the basis of the figure of merit $\frac{S}{\sqrt{S+B}}$. A scan on the NN discriminator is performed, ranging from the minimum to the maximum value and performing a cut on the discriminator for both the signal and background templates. A cut value of 0.3 for the muon channel and of 0.4 for the electron channel yields the largest significance. The scan and the optimal cut value (dashed line) for both muon and electron channel is shown in Fig. 6.12.

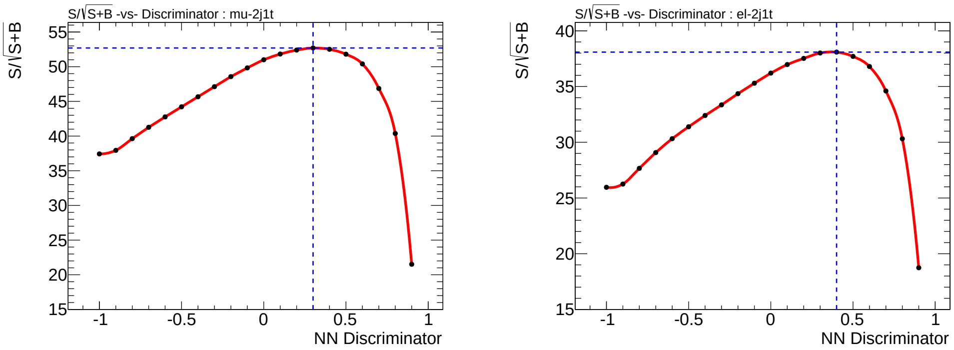

(a)

(b)

Figure 6.12.: Neural Network discriminator scan in the signal region. The NN discriminator is scanned from minimum to maximum range for the signal and background templates in order to find the optimum cut value (dashed line) depending on the signal and background ratio, separately for the electron and muon channel.

6.5. Background and Signal Estimation

The amount of background events is determined by a simultaneous fit of the neural network discriminator in the signal and $t\bar{t}$ control region in order to improve constraining the fraction of $t\bar{t}$ events. The fit is performed separately for the muon and electron channel.

A binned likelihood fit ranging from -1 to 1 in 20 bins of the discriminator distribution is performed with the THETA framework [173] in order to estimate the scale factors. The scale factors are defined as $\beta_i = \frac{\sigma_{\text{meas.}}}{\sigma_{\text{SM}}}$, where i is the index of the fitted process, $\sigma_{\text{meas.}}$ is the measured cross section and σ_{SM} is the predicted SM cross section. A scale factor of $\beta_i = 1$ means that exactly as many events have been measured as predicted. The predictions are taken from theoretical calculations and simulation.

Background processes are constrained within already measured uncertainties while still allowing for additional deviations due to different phase spaces than in this measurement. The prior uncertainty on $t\bar{t}$ is $\Delta = 20\%$ while the prior uncertainty on the other backgrounds is $\Delta = 30\%$. The QCD multijet template is being fixed during the fit to the results from the dedicated QCD estimation described in Section 5.4.

The likelihood function L is defined as

$$L(\beta_1, \ldots, \beta_C) = \prod_{k=1}^{B} P(n_k|\mu_k) \cdot \prod_{j=2}^{C} G(\beta_j|\Delta_j)\,, \tag{6.7}$$

where k is the bin index, B the number of bins, j the process index and C the number of all processes.

$$P(n_k|\mu_k) = \frac{(\mu_k)^{n_k}}{n_k!} \cdot e^{-\mu_k}\,, \tag{6.8}$$

where μ_k is the mean value of the expected number of events in bin k and n_k is the number of observed events in bin k. The mean value of the expected number of events μ_k is the sum of expected events for all processes

$$\mu_k = \sum_{j=1}^{C} \mu_{jk} = \sum_{j=1}^{C} \beta_j \cdot \hat{\nu}_j \cdot \alpha_{jk}\,, \tag{6.9}$$

where μ_{jk} is the expected number of events for process j in bin k and α_{jk} is the relative fraction of events for process j in bin k. The sum of all relative fractions must add up to one, $\sum_{k=1}^{B} \alpha_{jk} = 1$ for all processes j.

The second term $G(\beta_j|\Delta_j)$ in Eq. (6.7) is used to constrain background processes with a normal distribution with mean value 1 and a standard deviation of Δ_j

$$G(\beta_j|\Delta_j) = \frac{1}{\sqrt{2\pi}\Delta_j} \cdot e^{\left(-\frac{(\beta_j-1)^2}{2\Delta_j^2}\right)}\,, \tag{6.10}$$

where Δ_j is the relative rate uncertainty of the background process j.

The resulting scale factors for the muon and electron channel are shown in Table 6.3 and Table 6.4, respectively. Both the fit to the signal region and the combined fit including the $t\bar{t}$ control region are shown. The combined fit significantly reduces the uncertainty on the $t\bar{t}$ contribution while only marginally changing the signal beta factor. Therefore the results of the combined fit are used for the further analysis.

Table 6.3.: Scale factors for the neural network discriminator fit in the muon channel. The uncertainty quoted on the scale factor is the statistical uncertainty on the signal and background yields.

	Combined (3j2t-2j1t)	2j1t
Process	Scale Factor	Scale Factor
t-channel	0.98±0.02	1.00±0.02
s-channel	0.73±0.29	0.80±0.21
tW	1.38±0.24	0.78±0.28
$t\bar{t}$	1.08±0.01	1.25±0.05
W+jets(heavy)	1.32±0.07	1.10±0.11
W+jets(light)	0.82±0.29	0.91±0.28
Z+jets	0.98±0.28	0.88±0.28
Diboson (VV)	1.18±0.29	1.07±0.29

Table 6.4.: Scale factors for neural network discriminator fit in the electron channel. The uncertainty quoted on the scale factor is the statistical uncertainty on the signal and background yields.

	Combined (3j2t-2j1t)	2j1t
Process	Scale Factor	Scale Factor
t-channel	0.99±0.03	1.00±0.03
s-channel	0.93±0.29	0.98±0.29
tW	1.36±0.25	0.96±0.29
$t\bar{t}$	1.14±0.01	1.22±0.04
W+jets(heavy)	1.34±0.09	1.23±0.13
W+jets(light)	1.02±0.29	1.02±0.29
Z+jets	1.03±0.29	1.03±0.29
Diboson (VV)	1.08±0.29	1.02±0.29

6.6. Resulting Templates

The event yields after applying the NN cut $\mathrm{NN}_{\mathrm{Discr}} > 0.3$ and $\mathrm{NN}_{\mathrm{Discr}} > 0.4$ are given in Table 6.5 and Table 6.6 for the muon and electron channel, respectively. Due to the applied lepton criteria around twice as much muon as electron events are selected. In order to increase the amount of events for the unfolding procedure both channels are combined. The resulting histograms in the combined lepton+jets channel for the top quark transverse momentum p_{T} and rapidity $|y|$ after applying the NN cut are shown in Fig. 6.13(a) and Fig. 6.13(b), respectively. The MC templates of signal and background processes are normalized to the fit results of the combined fit. The QCD multijet templates are normalized to the results obtained from the dedicated data-driven QCD estimation described in Section 5.4. Both distributions of top quark transverse momentum p_{T} and rapidity $|y|$ and show a good agreement with the measured data.

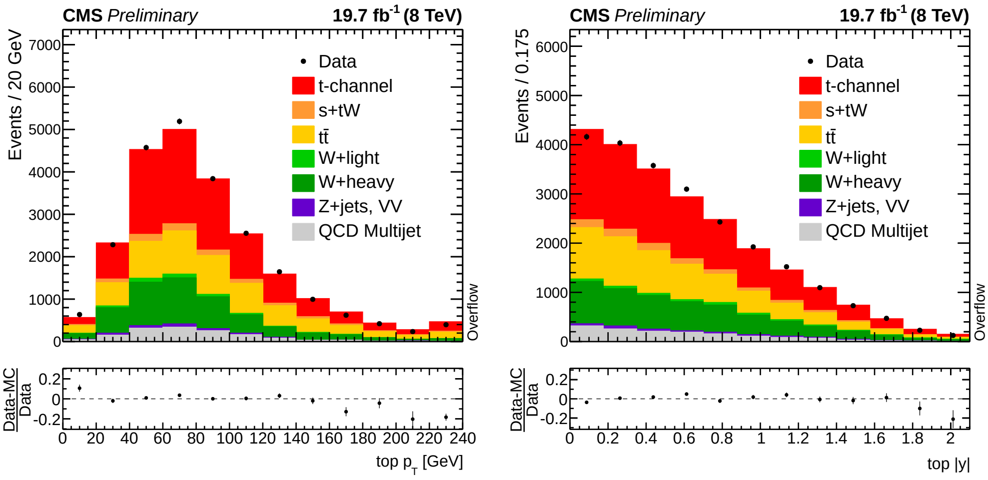

(a) (b)

Figure 6.13.: Top quark transverse momentum p_{T} (a) and rapidity $|y|$ (b) in the combined lepton+jets channel after applying the NN cut. The MC templates are normalized to the fit results.

Table 6.5.: Event yield in the muon channel after cutting the scaled neural network templates at $\mathrm{NN}_{\mathrm{Discr}} > 0.3$. The quoted uncertainties are the statistical uncertainties on the fit.

Muon Channel	Process	Events		Unc.
	t-channel	6618	±	135
	s-channel	75	±	31
	tW	508	±	95
	$\mathrm{t\bar{t}}$	3638	±	76
	W+jets(heavy)	3366	±	200
	W+jets(light)	253	±	90
	Z+jets	172	±	51
	VV	58	±	17
	Multijet QCD	1083	±	55
	Total	15772	±	297
	Data	15843		

Table 6.6.: Event yield in the electron channel after cutting the scaled neural network templates at $\mathrm{NN}_{\mathrm{Discr}} > 0.4$. The quoted uncertainties are the statistical uncertainties on the fit.

Electron Channel	Process	Events		Unc.
	t-channel	3307	±	92
	s-channel	43	±	15
	tW	260	±	53
	$\mathrm{t\bar{t}}$	1985	±	57
	W+jets(heavy)	1360	±	104
	W+jets(light)	129	±	39
	Z+jets	57	±	18
	VV	26	±	9
	Multijet QCD	375	±	40
	Total	7540	±	170
	Data	7548		

7. Differential Cross Section Measurements

In this chapter the final results of this thesis are presented. Based on the analysis in the previous chapters, differential measurements in the single top-quark t-channel of the top quark transverse momentum p_{T} and absolute value of rapidity $|y|$ are performed and compared with predictions from several generators with different approaches. In order to compare with theoretical predictions, the measurement has to take into account the limited detector resolution and selection efficiencies. Events reconstructed in the detector are measured with a finite detector resolution and the efficiency of the event selection cuts affects, if dependent on the investigated variable, its distribution.

In order to correct for these effects, the reconstructed simulated events are compared to events at generator level via a *migration matrix*. A generalized matrix inversion method, called *unfolding*, is performed on this migration matrix with the TUNFOLD package [84]. The algorithm is based on a least squares fit and the *Tikhonov-Phillips regularization* [174, 175], also known as *ridge regression*. The regularization strength parameter τ is estimated by minimizing the global correlation in pseudo experiments [176].

This matrix inversion problem can be formulated mathematically as

$$\tilde{y}_i = \sum_{j=1}^{m} A_{ij}\tilde{x}_j + b_i, 1 \leq i \leq n, \tag{7.1}$$

where the m bins $\tilde{x}_j$ describe the true distribution, A_{ij} is the smearing matrix, consisting of the migration matrix filled with the possibilities of migration from bin j to the bins i on detector level times the selection efficiency for each bin in the diagonal entries, $\tilde{y}_i$ is the average event count per bin at detector level and b_i is the background in bin i. In addition, systematic uncertainties affecting the migration matrices or the background estimations have to be considered. A schematic representation of the unfolding procedure is shown in Fig. 7.1.

Unfolding is an ill-posed problem in the sense that estimating the inverse of the migration matrix A is very sensitive to perturbations in the data. Ill-posed is the opposite of well-posed [177], which means, that the solution must exist, be unique and depend continuously on the initial boundary conditions. That implies, that simply inverting the matrix is not possible since statistical fluctuations in the event count are amplified and lead to unstable results. However, these fluctuations can be dampened by imposing certain conditions on the smoothness of the unfolded result, called *regularization*.

In the following, first the background estimation and subtraction are discussed. Then, the regularized unfolding method is described in detail and closure tests are presented to check the correctness of the method. After that, the estimation and definition of the systematic uncertainties and their propagation through the unfolding procedure are described. At last, the results are presented and discussed.

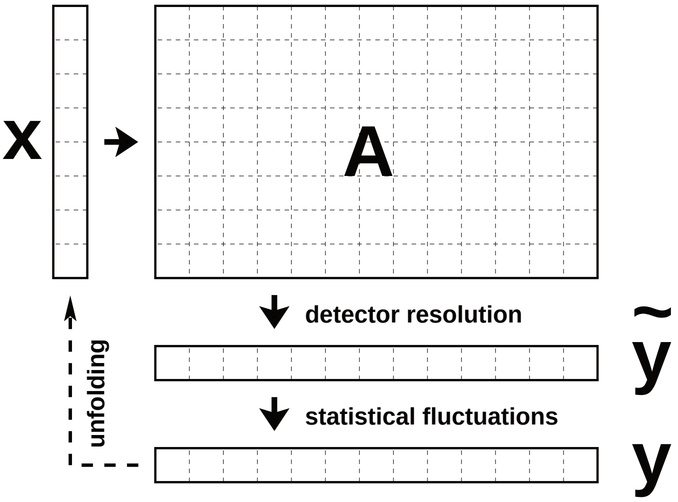

Figure 7.1.: Schematic view of the unfolding procedure with migration effects and statistical fluctuations. The smearing matrix A is used to correct for selection efficiencies and detector resolution effects in data, taking into account statistical fluctuations.

7.1. Background Subtraction

The templates shown in Fig. 6.13 are used as input for the unfolding procedure. The contributions from background processes to data have to be subtracted before unfolding. The number of events stemming from background processes is estimated with a binned likelihood fit to the neural network discriminator as described in Section 6.5.

The reconstructed distributions are corrected for background contributions by subtracting the background templates, normalized to the fit results, from data. In order not to overestimate the statistical uncertainty, the correlations between the different background processes have to be considered. In this analysis, it has been checked with pseudo experiments that the correlation increases the statistical uncertainty only marginally and is not relevant when compared to the systematic uncertainties.

7.2. Regularized Unfolding

As mentioned before, the regularized unfolding solves the ill-posed problem of inverting the smearing matrix in order to get the true, non-smeared distribution from the measured data. The problem can be described mathematically as $\vec{y} = A\vec{x}$, where $\vec{x}$ is the true underlying distribution and A is the smearing matrix, taking into account the selection efficiency, shown in Fig. 7.2, and bin-by-bin migration, shown in Fig. 7.4. The shapes of the investigated variables at generator level, generator level after selection cuts and reconstruction level are shown in Fig. 7.3. In this case the correction from the variable dependent selection efficiency is larger than the migration effect.

The problem can be solved by posing it as a least-square problem and minimizing

$$\chi^2(\vec{x}) = (A\vec{x} - \vec{y})^T V_y^{-1} (A\vec{x} - \vec{y}) \,, \tag{7.2}$$

where V_y is the covariance matrix of the measured distribution $\vec{y}$. A general solution of this problem is

$$\vec{x}_{\chi^2} = A^\dagger \vec{y} \,, \quad \text{where} \quad A^\dagger = (A^T V_y^{-1} A)^{-1} A^T V_y^{-1} \,. \tag{7.3}$$

However, as described before, the solution is not stable and fluctuates wildly with small changes in $\vec{y}$. In order to get a more stable solution, the problem is regularized by adding two additional terms

$$\chi^2(\vec{x}, \kappa) = \chi^2(\vec{x}) + \tau ||L(\vec{x} - \vec{x}_{bias})||^2 + \kappa (N_{obs} - \sum_{i=1}^{n} (A\vec{x}_i))^2 \,, \tag{7.4}$$

where $\vec{x}_{bias}$ is a bias distribution generated from the signal MC sample to allow the curvature to be weighted correctly despite inhomogeneity in the bin statistics. It is normalized to the observed number of events after subtraction divided by the overall selection efficiency. The two additional terms are proportional to the regularization parameter τ and the normalization constant κ. The regularization term introduces a matrix L which in this case is chosen such that $L(\vec{x} - \vec{x}_{bias})$ is proportional to the second derivatives of $\vec{x} - \vec{x}_{bias}$. This regularization scheme is a common choice to smoothen the resulting distributions and suppress unphysical fluctuations. The norm of the solution is fixed by the second additional term proportional to the Lagrangian multiplier κ. The minimization is performed with regard to the two parameters simultaneously.

The choice of the strength of the regularization parameter τ has a large impact on the resulting distribution. If the regularization parameter is too small, the unfolded result often has large fluctuations. When the regularization is too strong, the result is biased against the assumed distribution. Many different methods are known in literature to estimate the best regularization parameter, e.g. minimum global correlation or an L-curve scan [178]. In some cases however, the L-curve scan does not converge. Despite this, the methods are nearly equivalent and the choice is arbitrary. In this analysis the minimum global correlation [176] method is used, where the optimal solution has the smallest correlation between the bins in the unfolded distribution. When the regularization is too weak, the result will have strongly anti-correlated bins. If it is too strong, the result will be mostly flat with large correlation between neighboring bins. The global correlation coefficient is defined as the measure of the total amount of correlation between an element of $\vec{x}$ and all other elements, the correlation for each data in bin i is defined as:

$$\rho_i = \sqrt{1 - (V_{x,ii} \cdot V_{x,ii}^{-1})^{-1}} \,. \tag{7.5}$$

The correlation coefficient ρ_i can take values between 0 and 1. If all bins of the result are completely uncorrelated the covariance matrix V_x is diagonal and all ρ_i are zero.

The global correlation efficient is the total correlation between all bins is defined as the arithmetic or geometric mean of all correlation efficients

$$\rho_{tot} = \left(\frac{1}{n} \sum_{i=1}^{n} \rho_i^2 \right)^{\frac{1}{2}} . \tag{7.6}$$

A scan with different values of the regularization parameter τ is performed and each time the global correlation ρ_{tot} is calculated for the unfolded distribution. The result with the minimal global correlation yields the best choice for τ.

The unfolding is performed in twelve bins for the reconstructed spectrum, six bins are used for the unfolded distribution. The number of reconstructed bins has to be larger than the number of unfolded bins to guarantee a stable solution [84]. The reasonableness of the chosen binning scheme can be estimated by looking at the purity P and stability S of each bin in the unfolded spectrum. The purity is defined as

$$P = \frac{N_{rec,gen}}{N_{rec}} , \tag{7.7}$$

and measures the probability for events with a reconstructed top-quark p_{T} (or $|y|$) value in a certain range, N_{rec}, to have also a generated value in this range, $N_{rec,gen}$. Since the number of reconstructed bins is twice as large as the number of generated bins, each time two reconstructed bins are compared with one generated bin. The stability is defined as

$$S = \frac{N_{rec,gen}}{N_{gen}} , \tag{7.8}$$

and measures the probability for events with a generated top-quark p_{T} (or $|y|$) value in a certain range, N_{gen}, to also have a reconstructed value in this range, $N_{rec,gen}$. Values above 50% for both quantities are advised.

For the measurement of top-quark p_{T} the purity lies in the range between 50 and 75% while the stability is in the range from 50 to 85%. For the measurement of top-quark $|y|$ the purity is between 53 and 67% while the stability is between 41 and 81%. The stability of the sixth bin is a bit lower with only 32%. While events with top-quark p_{T} ($|y|$)values beyond 240 GeV ($|y| > 2.1$) are collapsed into the last visible bin in the reconstructed bin shown in Fig. 6.13 (overflow bin), the events are not considered in the unfolding, i.e. only events with $p_{\mathrm{T}} < 240$ GeV ($|y| < 2.1$) are used to derive the unfolded differential cross sections.

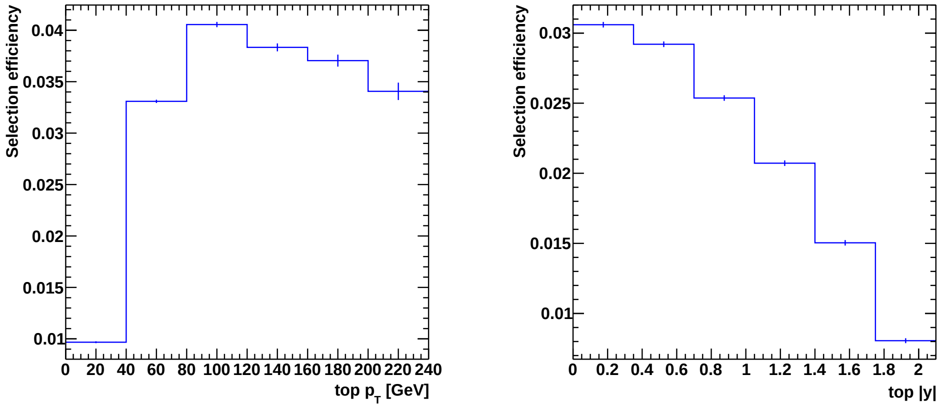

(a) (b)

Figure 7.2.: Selection efficiency as a function of the true top quark p_T (a) and as function of the true top quark $|y|$ (b) for the combined lepton+jets channel. The error bars indicate the statistical uncertainty due to the limited MC sample size.

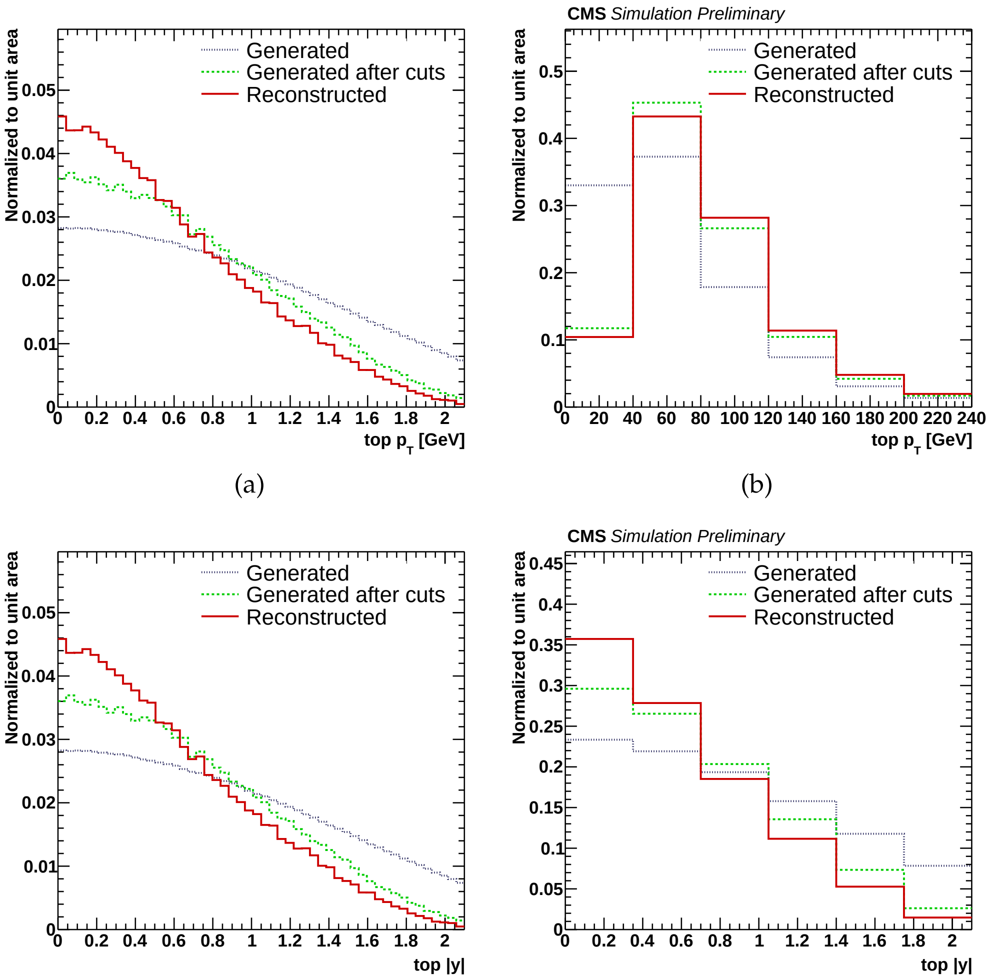

(a) (b)

(c) (d)

Figure 7.3.: Shape comparison of the transverse momentum p_{T} (a), (b) and the absolute value of the rapidity $|y|$ (c), (d) of the single top quark on generator level without any selection cuts, generator level after selection cuts, and reconstruction level after selection cuts in the combined lepton+jets channel. The comparison is shown in two different binnings: (a) and (c) 50 bins; (b) and (d) six bins.

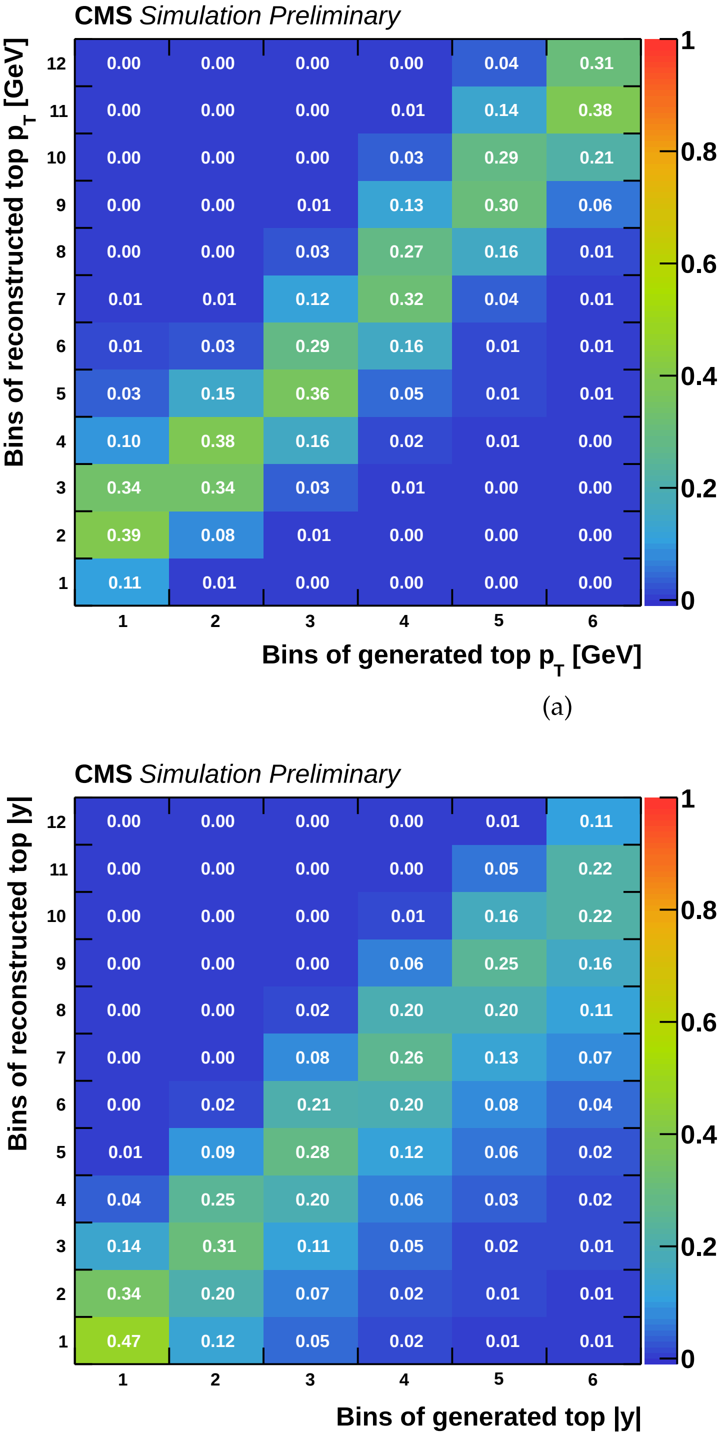

(a)

(b)

Figure 7.4.: Migration matrices for top quark p_T and $|y|$. Each migration matrix gives the probability of an event with a certain true top quark p_T to show up in one of the bins of the reconstructed top quark p_T (a), same for $|y|$ (b).

7.3. Closure Tests of the Unfolding Procedure

The correctness of the unfolding procedure is checked with a closure test, where pseudo data is used and the unfolded value of the top quark p_{T} ($|y|$) is compared to the true value. Fifty thousand pseudo experiments are performed, where a Poisson number N is diced with the expectation value of the bin content and drawn from each bin for each of the templates.

For the closure test, the pull and the relative difference in each of the six generated bins are calculated. The pull for each bin is defined as the difference between the generated and unfolded spectrum in that bin divided by the uncertainty of the unfolded spectrum in that bin. The relative difference is the difference between the generated and unfolded spectrum in that bin divided by the generated spectrum in that bin. The relative differences for each of the six bins are shown in Fig. 7.5 and Fig. 7.6 for the top quark p_{T} and $|y|$, respectively. For the pull distributions Fig. 7.7 and Fig. 7.8 a mean around zero and a width, root mean square (RMS), close to one indicate that the uncertainties are estimated correctly. Similarly, a relative difference around zero indicates that the unfolding is unbiased, while the width is an indicator for the uncertainty from the unfolding procedure. Both conditions are almost fulfilled in the closure test. Only the pull distributions indicate that the binning and regularization scheme introduce a small bias.

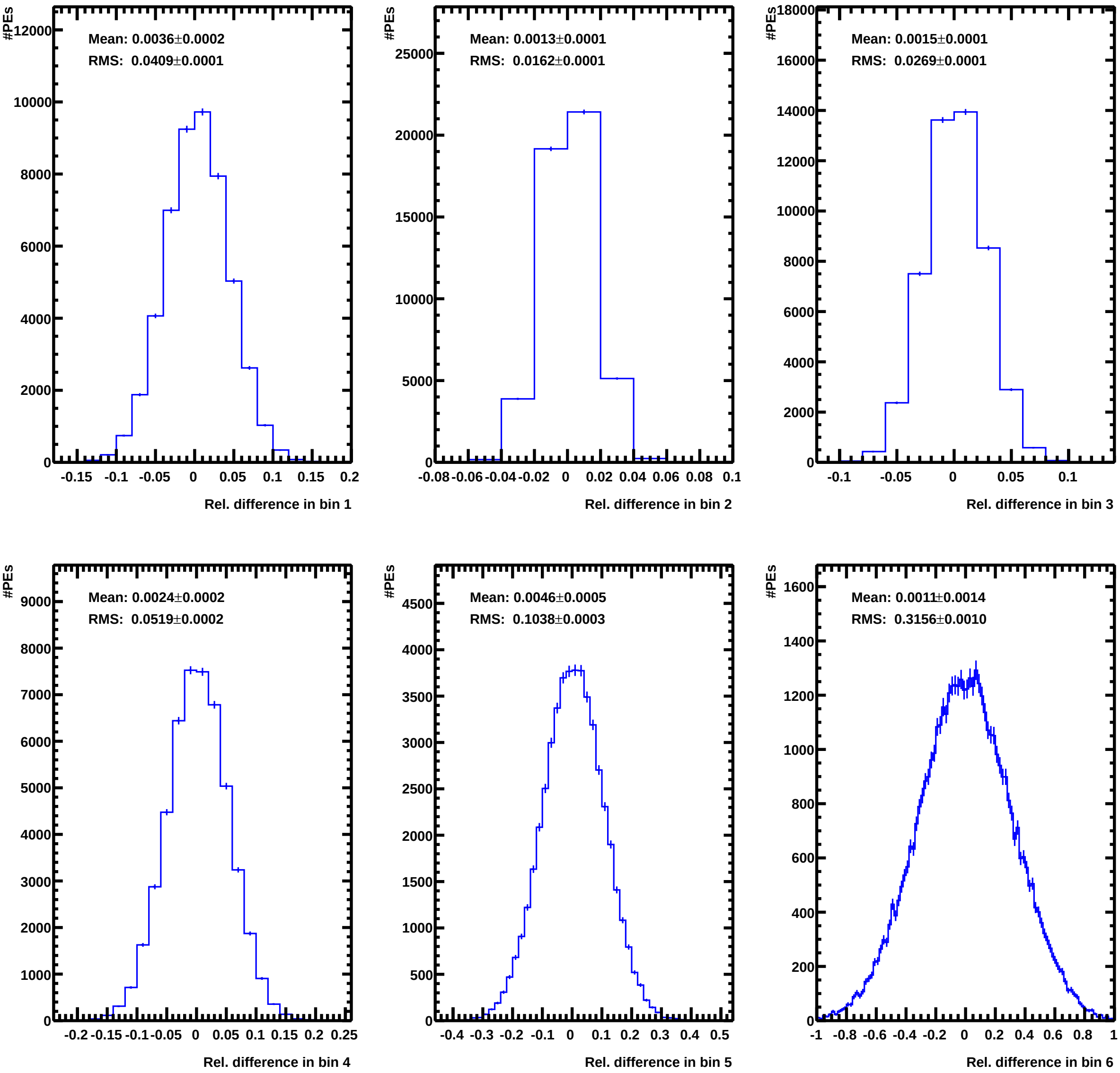

Figure 7.5.: The relative difference between unfolded and true top quark p_T in the combined lepton+jets channel per bin. The means are nearly zero which shows that the unfolding method has minimal bias.

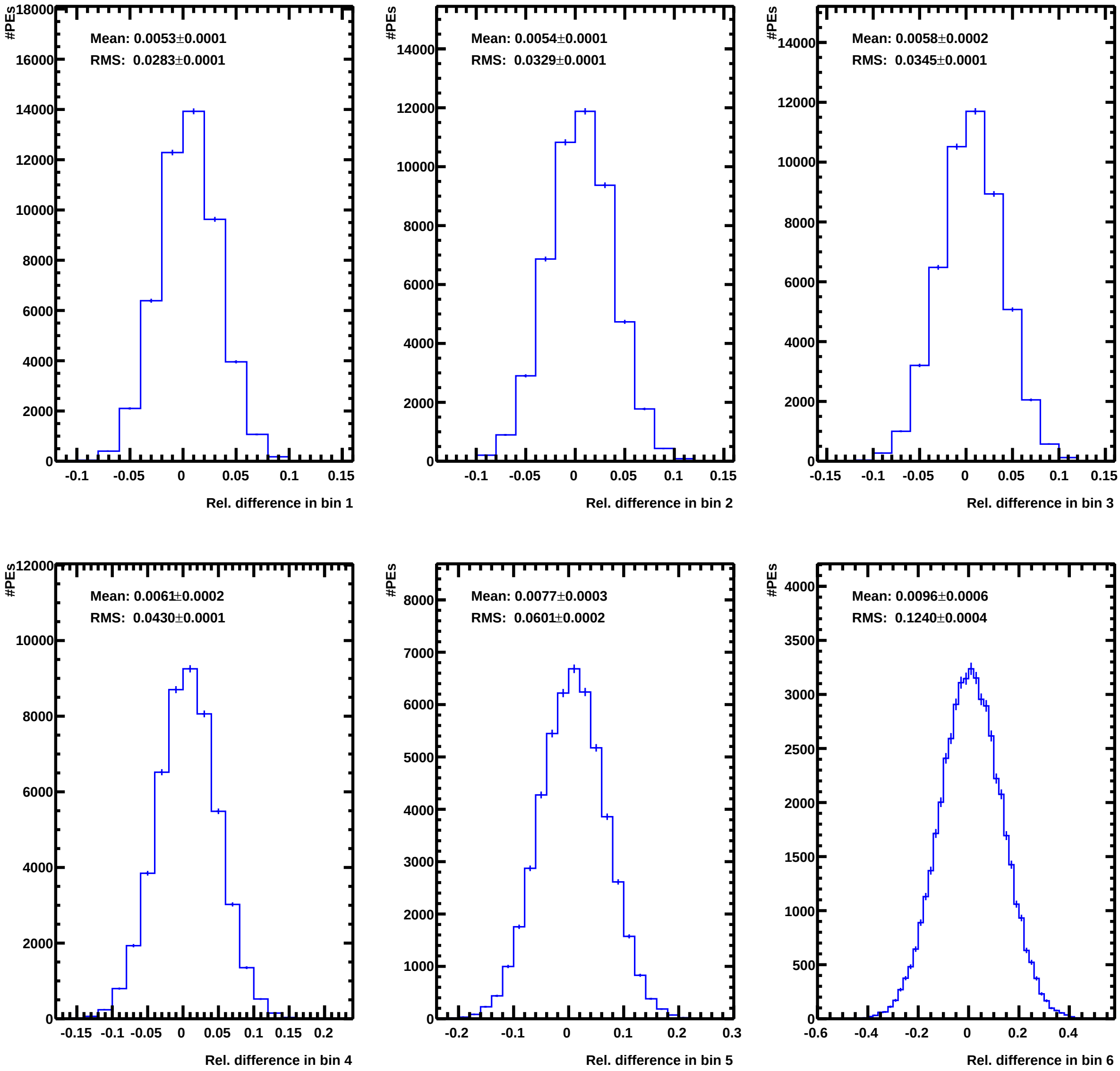

Figure 7.6.: The relative difference between unfolded and true top quark $|y|$ in the combined lepton+jets channel per bin. The means are nearly zero which shows that the unfolding method has minimal bias.

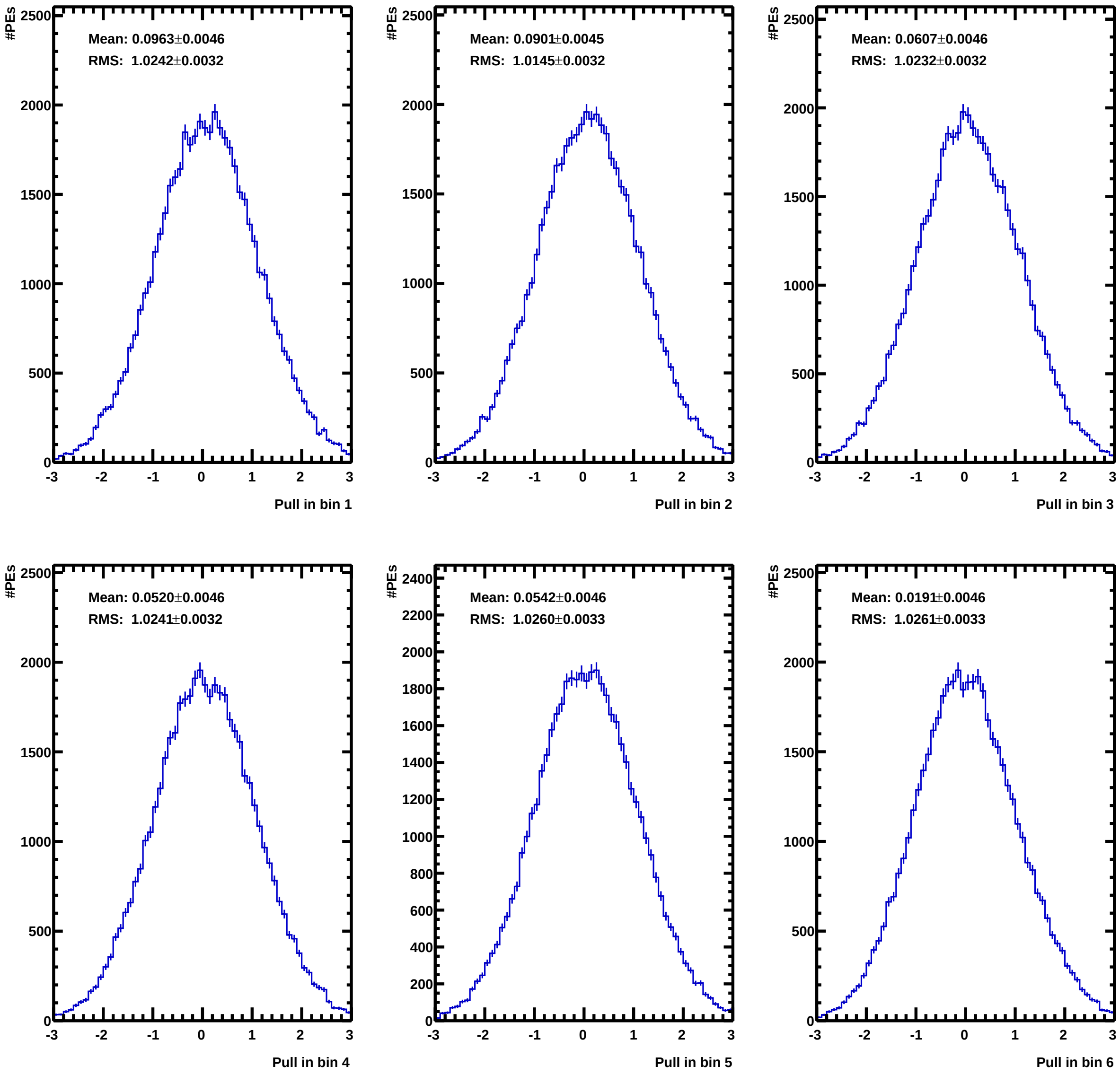

Figure 7.7.: Pulls for top quark p_{T} in the combined lepton+jets channel per bin. The mean is only slightly above zero and the width nearly 1, which shows that the unfolding method has minimal bias.

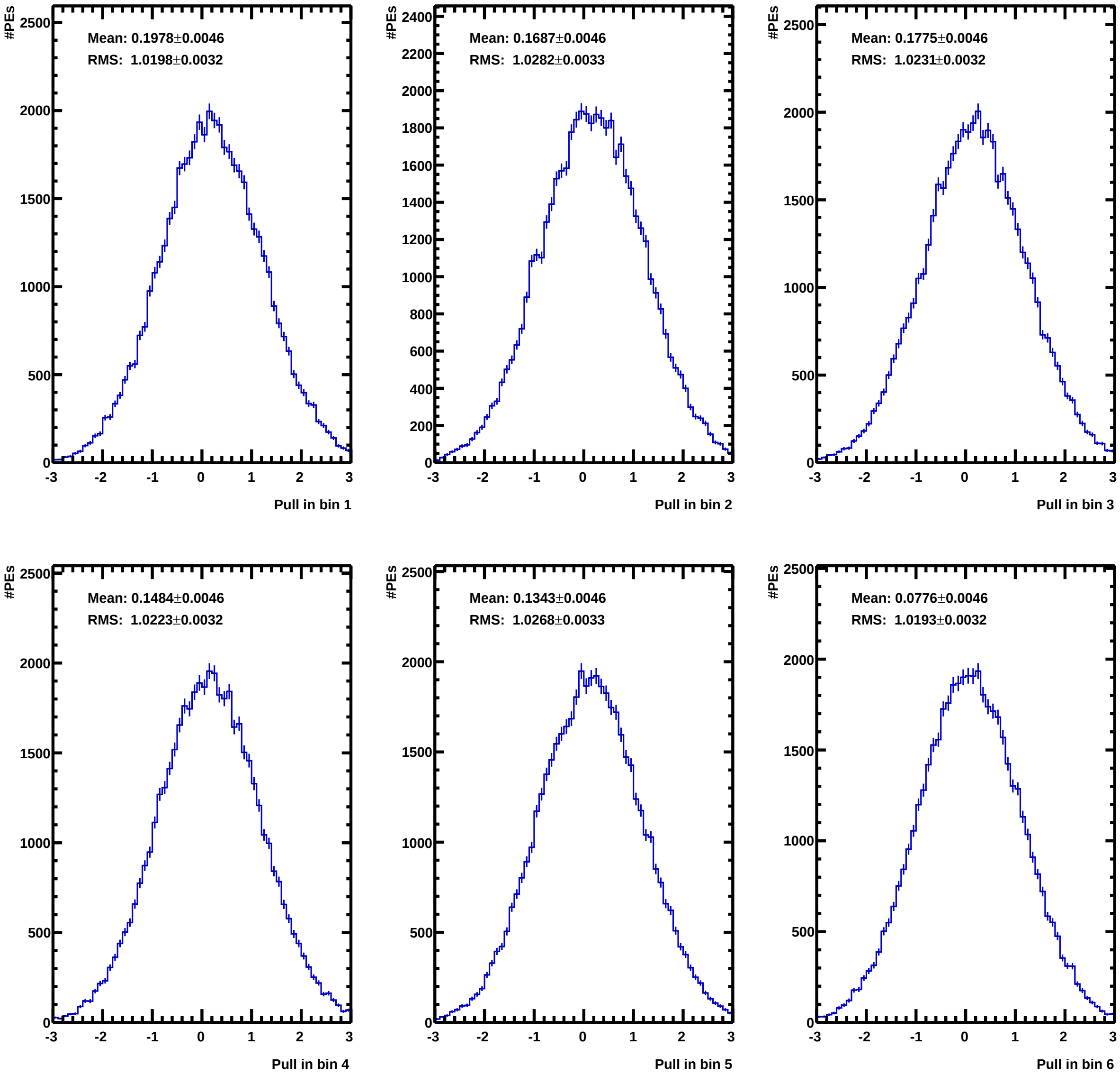

Figure 7.8.: Pulls for top quark $|y|$ in the combined lepton+jets channel per bin. The mean is only slightly above zero and the width nearly 1, which shows that the unfolding method has minimal bias.

7.4. Estimation of Systematic Uncertainties

The unfolded spectra of the top quark p_{T} and top-quark $|y|$ can be affected by various sources of systematic uncertainties due to either the detector resolution, reconstruction efficiencies or theoretical uncertainties in the modeling of signal and background processes. Some systematic uncertainties cancel due to the fact that the result is a normalized differential cross section, where the resulting unnormalized spectrum is divided by the inclusive cross section with the same systematic uncertainties. However, changes in the result are still expected due to the variation in various parameters. The impact of the individual systematic uncertainties described in the following are estimated as follows in a similar way as in the $\mathrm{t\bar{t}}$ charge asymmetry analysis [179]. The full analysis is repeated on the measured data using signal and background templates for the background estimation and unfolding that are affected by the investigated systematic uncertainty. When the systematic uncertainty affects the signal process the affected migration matrices and selection efficiencies are used as well.

The following systematic uncertainties have been considered:

- Jet energy scale (JES): The uncertainty of jet energy scale (JES) is estimated from the uncertainties on the jet energy corrections (JEC) [180]. The uncertainties stem from several independent sources but are combined into one uncertainty. All reconstructed jet four-momenta in simulated events are varied according to the η and p_{T} dependent uncertainties which also changes the total momentum in the transverse plane. Thereby the effect is propagated to $\not{E}_{\mathrm{T}}$.

- Jet energy resolution (JER): Jet asymmetry measurements suggest that resolutions in jet p_{T} are about 5% to 29% worse in data compared to simulation, depending on the $|\eta|$ value of the jet. For that reason the distribution of reconstructed p_{T} for a fixed generated jet p_{T} is broader by the given percentage. The uncertainty on this measurement is about 6 to 20 percent points, again depending on the jet $|\eta|$. To account for this difference, all jets in the simulated samples are scaled accordingly. The systematic uncertainty on this correction is estimated based on further smearing within the uncertainties of the used correction factors [181].

- Unclustered energy in $\not{E}_{\mathrm{T}}$: The energy contribution from all jets with $p_{\mathrm{T}} < 10$ GeV and “PFCandidates” not clustered to jets is called “unclustered energy”. This energy contribution is varied by $\pm 10\%$ and the resulting uncertainty is propagated to the calculation of the missing transverse energy.

- Pileup modelling (PU): All MC samples used in this analysis are reweighted in a manner that the number of simulated pileup events matches the number of pileup events inferred from data. To account for uncertainties in the pileup distribution of data events, the measurement is performed with samples reweighted to match shifted versions of the data pileup distribution, as described at [182]. This corresponds to a $\pm 6\%$ variation in reference to the nominal total inelastic cross section of 69.4 mb.

- b-tagging: In order to estimate the uncertainty related to b-tagging, the applied b-tagging scale factors are varied within their uncertainties [153]. The variations are performed simultaneously for b- and c-quark jets, and they are combined in a common uncertainty. The scale factors for light-flavor jets are varied independently from the heavy-flavor scale factors and are treated as an independent mistag uncertainty.

- Top-quark p_T reweighting: Differential cross section measurements have shown that the p_T spectrum of the top quarks in $\mathrm{t\bar{t}}$ events is significantly softer than the one generated by simulation programs. To correct for this effect the used events are reweighted according to scale factors derived from these measurements. As a measure of the resulting uncertainty, the measurement is performed with samples lacking any reweighting and with samples that have been reweighted twice.

- Top-quark mass: The impact of a different top quark mass than the nominal one of 172.5 GeV is estimated by using different samples for t-channel and $\mathrm{t\bar{t}}$ with a top quark mass of either 171 GeV or 173 GeV.

- Electron and muon trigger/efficiencies: The uncertainties on the globally derived scale factors for electron and muon trigger, isolation and ID are added in quadrature to the already applied scale factors.

- Q^2 scale: The uncertainties on the renormalization and factorization scales are studied with dedicated samples for $\mathrm{t\bar{t}}$, W+jets and single top t-channel. These samples are generated with twice and half the nominal Q value of the hard scattering process.

- Matching threshold: The impact of a higher and lower matching threshold for MADGRAPH processes is studied with dedicated samples for $\mathrm{t\bar{t}}$ and W+jets.

- Muon resolution: The reconstruction of muons has been studied in Z boson decays. A transverse momentum resolution uncertainty of 0.6% is applied to all muons.

- QCD multijet modeling: The estimated rate of the QCD multijet template is scaled up by a factor of two to account for a potential mismodeling from the anti-isolated region.

- Parton Distribution Functions (PDFs): The impact of different PDF sets (CT10, NNPDF2.1 and MSTW2008) and their uncertainty bands has been taken into account for the signal modeling according to the PDF4LHC [43] recommendation.

A breakdown of the impact of the individual systematic uncertainties is given in Table 7.1 and Table 7.2 for top-quark p_T and $|y|$, respectively. The effect on top-quark p_T due to systematic variations is shown in Fig. 7.9,Fig. 7.10 and Fig. 7.11, while the effect on top-quark $|y|$ due to systematic variations is shown in Fig. 7.12,Fig. 7.13 and Fig. 7.14. It can be seen, that the JES, $\not{E}_\mathrm{T}$ and matching scale uncertainties have the largest impact on the measurement.

Table 7.1.: Systematic uncertainties for the unfolding of top p_{T}.

Uncertainty / Δ [%]	Bin 1	Bin 2	Bin 3	Bin 4	Bin 5	Bin 6
Jet energy scale	+12.2 -0.0	+1.0 -2.1	+0.0 -6.2	+0.0 -16.1	+0.0 -26.7	+0.0 -41.0
J energy resolution	+3.4 -0.0	+0.1 -1.0	+0.3 -1.6	+0.0 -2.2	+0.0 -11.1	+0.0 -29.6
$\not{E}_{\mathrm{T}}$	+10.4 -12.1	+1.9 -2.3	+8.9 -8.5	+25.5 -23.4	+42.1 -28.0	+55.4 -31.6
Pileup	+2.9 -0.0	+0.0 -0.2	+0.0 -1.0	+0.0 -3.0	+0.0 -13.1	+0.0 -21.0
b-tagging	+0.7 -1.1	+0.2 -0.1	+1.1 -0.9	+2.4 -1.9	+1.1 -0.6	+1.2 -0.6
Mistagging	+0.2 -0.6	+0.3 -0.2	+0.1 -0.0	+0.3 -0.0	+0.9 -0.3	+0.4 -0.0
Top p_{T} reweighting	+1.5 -1.0	+0.3 -1.0	+0.6 -0.3	+3.4 -2.5	+10.6 -10.3	+17.3 -18.5
Top quark mass	+2.8 -0.0	+0.7 -0.0	+0.0 -1.4	+0.0 -5.6	+0.0 -12.5	+0.0 -35.8
Lepton efficiencies	+1.0 -0.0	+0.7 -0.0	+0.0 -0.3	+0.0 -2.5	+0.0 -10.2	+0.0 -18.6
Q^2 scale t-channel	+0.0 -1.0	+0.9 -0.0	+0.0 -0.3	+0.4 -0.9	+0.8 -0.0	+13.6 -3.2
Q^2 scale W+heavy jets	+11.1 -0.0	+0.4 -6.7	+0.0 -5.7	+0.0 -7.5	+20.3 -0.0	+6.2 -0.0
Q^2 scale $\mathrm{t\bar{t}}$	+3.8 -0.9	+1.5 -1.2	+1.5 -0.9	+0.0 -3.4	+0.0 -12.9	+0.0 -19.1
Matching W+heavy jets	+2.8 -1.5	+1.3 -1.3	+0.0 -3.5	+0.0 -13.1	+29.0 -0.0	+72.0 -0.0
Matching $\mathrm{t\bar{t}}$	+1.7 -0.0	+0.3 -0.2	+0.5 -0.4	+0.0 -2.8	+0.0 -9.0	+0.0 -31.1
Muon resolution	+1.0 -0.0	+0.0 -0.5	+0.2 -0.0	+0.2 -0.0	+0.0 -3.9	+0.0 -9.4
QCD multijet estimation	+0.0 -1.2	+0.8 0.0	+0.0 -0.9	+1.4 0.0	+7.2 0.0	+0.0 -4.1
PDF	+0.1 -0.9	+0.0 -0.1	+0.5 -0.1	+1.8 -0.3	+3.5 -0.6	+3.8 -1.6
Total systematic uncertainty	+20.9 -12.5	+3.4 -7.7	+9.1 -12.8	+26.0 -33.4	+56.6 -49.2	+93.7 -86.1

Table 7.2.: Systematics uncertainties for the unfolding of top $|y|$.

Uncertainty / Δ [%]	Bin 1	Bin 2	Bin 3	Bin 4	Bin 5	Bin 6
Jet energy scale	+0.7 -5.1	+2.4 -2.3	+0.6 -0.2	+3.6 -2.2	+5.8 -1.9	+2.6 -0.8
Jet energy resolution	+0.0 -2.9	+1.9 -0.0	+0.8 -0.0	+1.4 -0.9	+1.3 -1.7	+0.0 -2.2
$\not{E}_T$	+6.1 -9.2	+4.2 -3.2	+1.9 -0.5	+5.1 -5.0	+7.3 -6.8	+7.4 -6.6
Pileup	+0.0 -1.5	+0.5 -0.0	+0.1 -0.2	+0.5 -0.0	+1.2 -0.0	+1.6 -0.0
b-tagging	+0.0 -0.5	+1.0 -0.0	+0.4 -0.0	+0.0 -0.2	+0.0 -0.9	+0.0 -1.1
Mistagging	+0.0 -0.7	+1.0 -0.0	+0.4 -0.0	+0.0 -0.4	+0.0 -1.0	+0.0 -1.2
Top quark p_T	+0.3 -0.2	+0.1 -0.2	+0.0 -0.2	+0.3 -0.2	+0.4 -0.1	+0.0 -0.3
Top quark mass	+2.1 -1.1	+1.4 -0.0	+0.6 -0.6	+0.0 -1.6	+0.0 -1.8	+0.0 -1.2
Lepton efficiencies	+0.0 -0.2	+1.1 -0.0	+0.2 -0.0	+0.0 -0.5	+0.0 -1.2	+0.0 -0.9
Q^2 scale t-channel	+2.2 -0.0	+1.5 -0.0	+0.3 -0.0	+0.0 -1.2	+0.0 -3.3	+0.0 -3.3
Q^2 scale W+heavy jets	+9.4 -0.0	+0.0 -2.9	+0.0 -3.5	+0.8 -3.7	+3.7 -1.8	+4.5 -4.6
Q^2 scale $t\bar{t}$	+0.4 -1.6	+0.3 -0.4	+0.4 -0.0	+0.9 -0.0	+1.1 -0.6	+1.5 -2.3
Matching W+heavy jets	+0.0 -7.5	+0.0 -8.2	+1.8 -3.9	+8.3 -0.0	+16.0 -0.0	+20.8 -0.0
Matching $t\bar{t}$	+0.3 -0.1	+0.2 -0.2	+0.5 -0.2	+0.3 -0.0	+0.0 -0.5	+0.0 -1.1
Muon resolution	+1.1 -0.0	+0.4 -0.0	+0.0 -0.2	+0.0 -0.6	+0.0 -0.9	+0.0 -1.3
QCD multijet estimation	+0.0 -3.6	+0.0 -1.5	+0.1 0.0	+1.6 0.0	+3.7 0.0	+4.8 0.0
PDF	+0.9 -1.7	+0.4 -0.9	+0.2 -0.2	+1.1 -0.6	+2.1 -1.1	+2.1 -1.1
Total systematic uncertainty	+11.7 -14.1	+6.0 -9.7	+3.0 -5.3	+10.8 -7.1	+19.5 -8.7	+23.4 -9.7

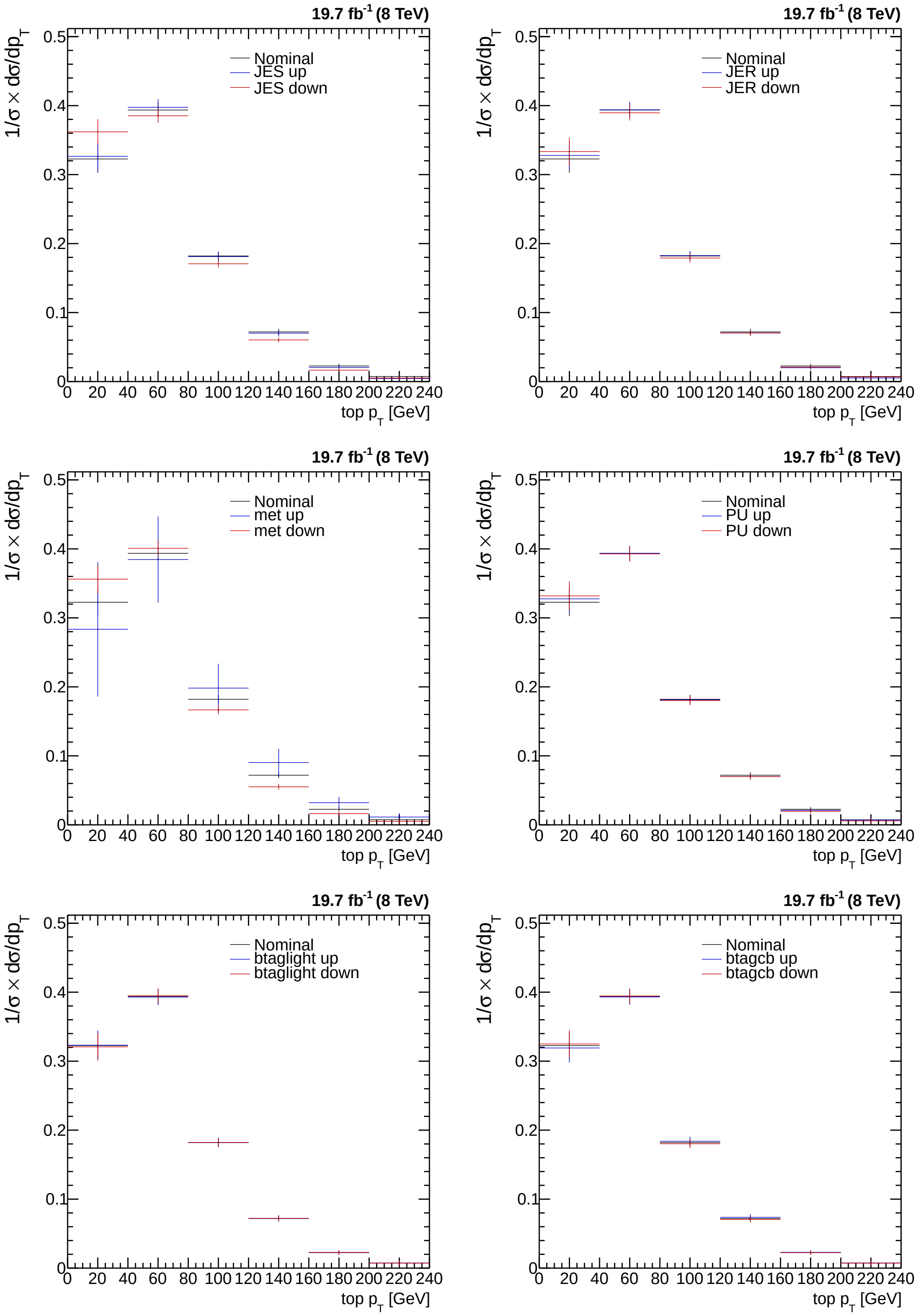

Figure 7.9.: Effect on the shape of the unfolded top-quark p_T spectrum due to variations in (a) the jet energy scale (JES); (b) the jet energy resolution (JER); (c) the unclustered energy; (d) pile up modeling; (e) and (f) b tagging efficiencies.

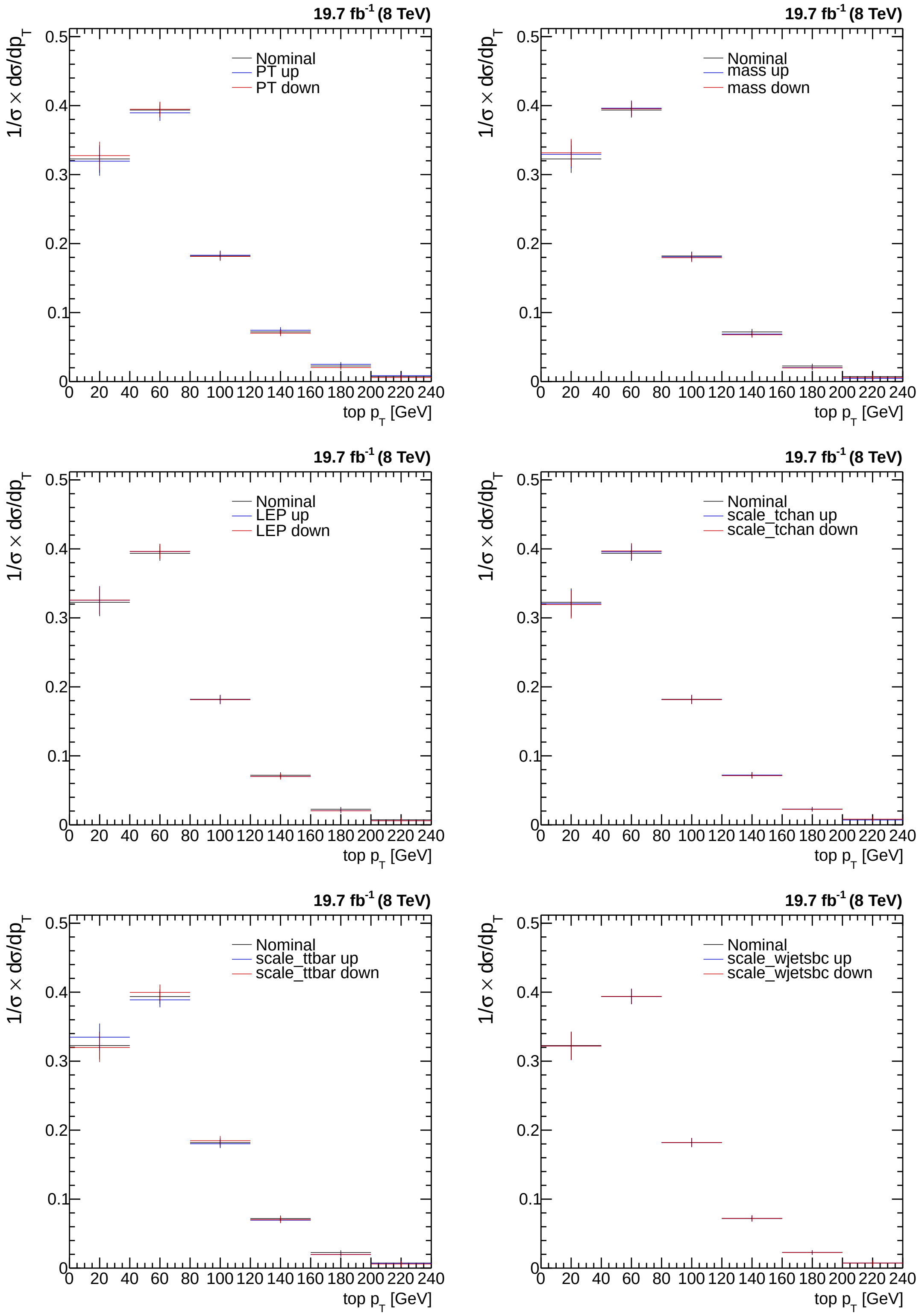

Figure 7.10.: Effect on the shape of the unfolded top-quark p_T spectrum due to variations in (a) top-quark-p_T reweighting; (b) the top-quark mass; (c) the lepton efficiencies; (d-f) the scale variations for single top t-channel, $t\bar{t}$ and W+jets.

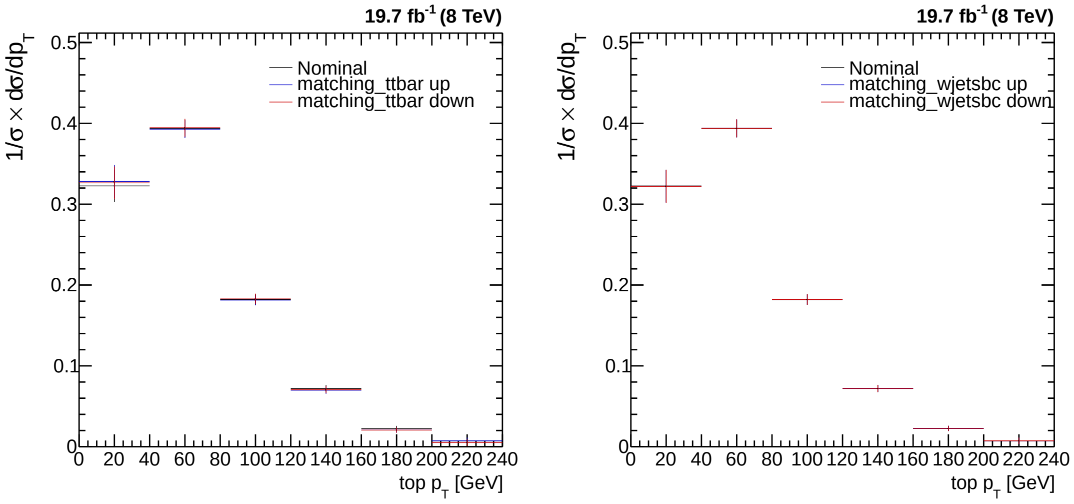

Figure 7.11.: Effect on the shape of the unfolded top-quark p_T spectrum due to variations in the matching threshold of (a) t$\bar{t}$ and (b) W+jets simulated events.

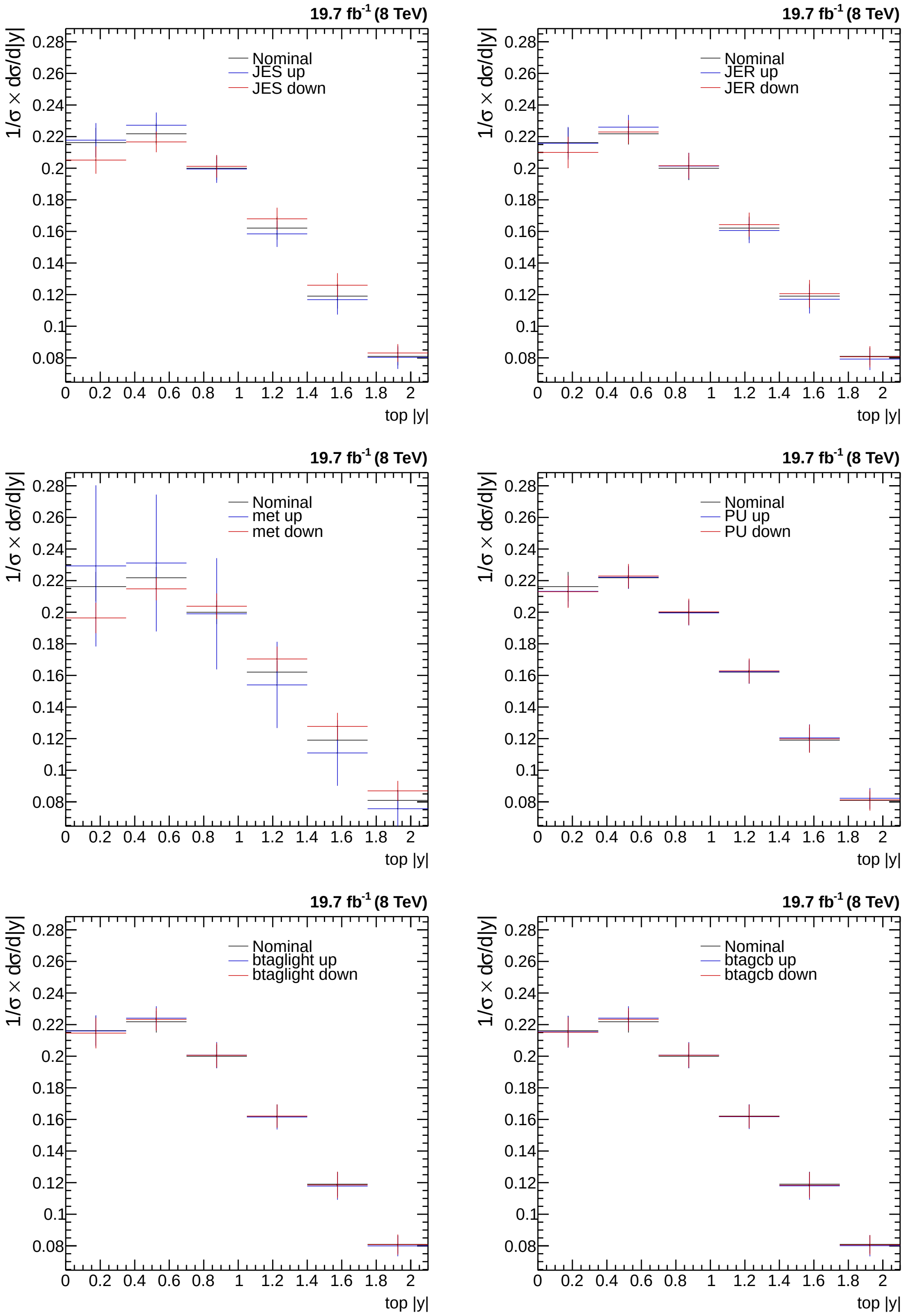

Figure 7.12.: Effect on the shape of the unfolded top-quark rapidity spectrum due to variations in (a) the jet energy scale (JES); (b) the jet energy resolution (JER); (c) the unclustered energy; (d) pile up modeling; (e) and (f) b tagging efficiencies

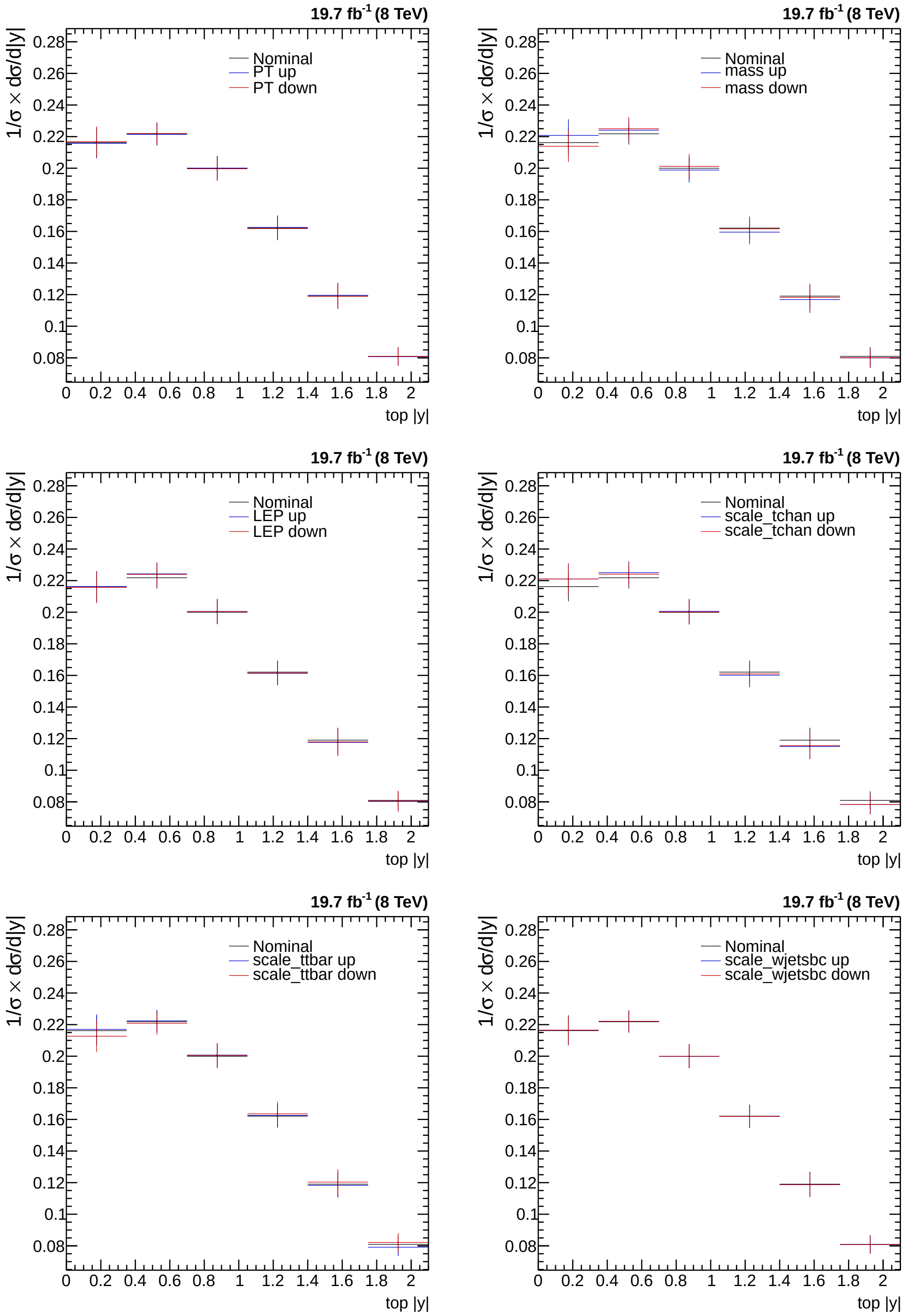

Figure 7.13.: Effect on the shape of the unfolded top-quark rapidity spectrum due to variations in (a) top-quark-p_T reweighting; (b) the top-quark mass; (c) the lepton efficiencies; (d-f) the scale variations for single top *t*-channel, $\mathrm{t\bar{t}}$ and W+jets.

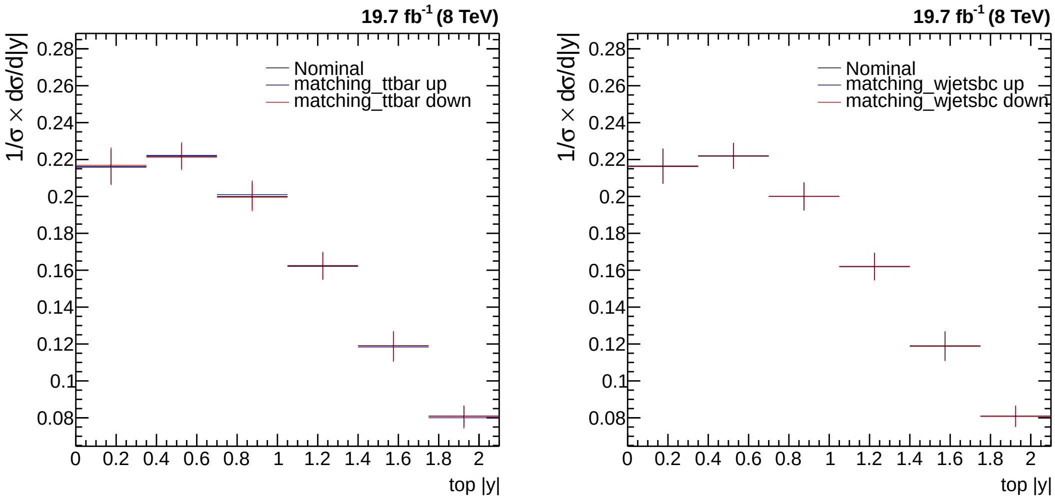

Figure 7.14.: Effect on the shape of the unfolded top-quark rapidity spectrum due to variations in the matching threshold of (a) $t\bar{t}$ and (b) W+jets simulated events.

7.5. Results

The aforementioned unfolding technique is used in the signal enriched phase space and the transverse momentum p_{T} and the rapidity of the top quark $|y|$ are unfolded in the combined lepton+jets channel. The unfolded data and generated distributions are shown in Fig. 7.15, normalized to the measured inclusive cross section. The normalized differential cross sections for each bin in p_{T} and $|y|$ are given in Table 7.3 and Table 7.4, respectively. The unfolded distributions from data are compared with distributions generated with different MC generators: POWHEG and AMC@NLO, two NLO generators, and COMPHEP. The largest difference between the two NLO generators is the flavor scheme used for the calculation. The signal MC generated with POWHEG was simulated in the 5-flavor-scheme and showered with PYTHIA 6. The AMC@NLO sample was produced in the 4FS and showered with PYTHIA 8. The matched COMPHEP sample, combining the $2 \rightarrow 2$ and $2 \rightarrow 3$ processes matched on the basis of the p_{T} spectrum of the second b quark, was showered with PYTHIA 6. All three different simulations describe the unfolded data well within the estimated statistical and systematic uncertainties. Although the simulations show differences in the hardness of the p_{T} spectrum and centralness of the $|y|$ spectrum, the dominating systematic uncertainties have to be greatly reduced in order to differentiate between them. No large deviation can be seen which would be a sign for new physics. The results presented here have been published by the CMS Collaboration as a preliminary physics analysis summary [183].

Table 7.3.: Normalized differential cross section as function of the transverse momentum of the top quark, $\frac{1}{\sigma} \times \frac{d\sigma}{dp_{\mathrm{T}}}$, compared to theory predictions calculated with POWHEG.

	Normalized differential cross section: $\frac{1}{\sigma} \times \frac{d\sigma}{dp_{\mathrm{T}}}$	
p_{T}	Unfolded	Generated (POWHEG)
$[0.0, 40.0]$	$0.323 \pm 0.020(\text{stat.})^{+0.067}_{-0.040}(\text{syst.})$	0.330
$[40.0, 80.0]$	$0.394 \pm 0.011(\text{stat.})^{+0.013}_{-0.030}(\text{syst.})$	0.373
$[80.0, 120.0]$	$0.182 \pm 0.006(\text{stat.})^{+0.017}_{-0.023}(\text{syst.})$	0.179
$[120.0, 160.0]$	$0.072 \pm 0.004(\text{stat.})^{+0.019}_{-0.024}(\text{syst.})$	0.074
$[160.0, 200.0]$	$0.023 \pm 0.003(\text{stat.})^{+0.013}_{-0.011}(\text{syst.})$	0.031
$[200.0, 240.0]$	$0.007 \pm 0.004(\text{stat.})^{+0.007}_{-0.006}(\text{syst.})$	0.014

Table 7.4.: Normalized differential cross section as function of the absolute rapidity of the top quark, $\frac{1}{\sigma} \times \frac{d\sigma}{d|y|}$, compared to theory predictions calculated with POWHEG.

	Normalized differential cross section: $\frac{1}{\sigma} \times \frac{d\sigma}{d|y|}$	
$|y|$	Unfolded	Generated (POWHEG)
$[0.0, 0.35]$	$0.216 \pm 0.009(\text{stat.})^{+0.025}_{-0.030}(\text{syst.})$	0.233
$[0.35, 0.7]$	$0.222 \pm 0.007(\text{stat.})^{+0.013}_{-0.022}(\text{syst.})$	0.219
$[0.7, 1.05]$	$0.200 \pm 0.007(\text{stat.})^{+0.006}_{-0.011}(\text{syst.})$	0.193
$[1.05, 1.4]$	$0.162 \pm 0.007(\text{stat.})^{+0.018}_{-0.012}(\text{syst.})$	0.158
$[1.4, 1.75]$	$0.119 \pm 0.008(\text{stat.})^{+0.023}_{-0.010}(\text{syst.})$	0.118
$[1.75, 2.1]$	$0.081 \pm 0.006(\text{stat.})^{+0.019}_{-0.008}(\text{syst.})$	0.078

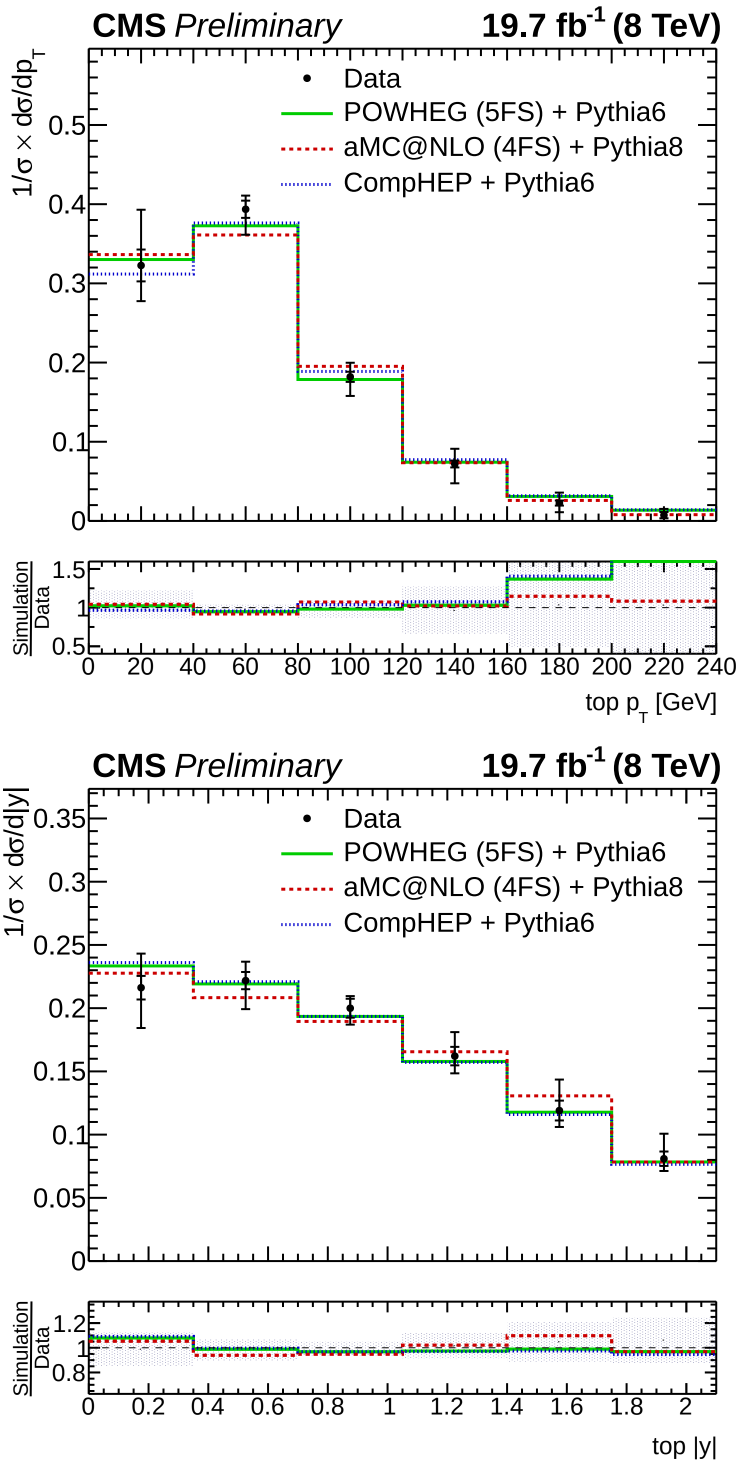

Figure 7.15.: Unfolded top-quark p_T (top) and top-quark $|y|$ (bottom) spectra in the combined lepton+jets channel. The distributions are normalized to 1.0 by dividing each bin with the inclusive cross section corresponding to the fitted event yields. Statistical and systematic uncertainties are shown.

8. Summary and Outlook

8.1. Summary

The endeavor to study electroweak single top quark production in the scope of this thesis at CMS has been very fruitful. Several properties of the top quark and the standard model have been measured:

- cross sections, and thus the CKM matrix element $|V_{tb}|$,
- charge ratio, giving a handle on the u/d PDF of the proton,
- top quark polarization, constraining anomalous couplings,
- differential cross sections in the t-channel for top-quark p_{T} and $|y|$.

Single top-quark production cross sections have now been measured at $\sqrt{s} = 7$ TeV and $\sqrt{s} = 8$ TeV in all three production modes. The development of a neural network analysis for the first measurement at $\sqrt{s} = 7$ TeV was crucial to select a large enough amount of signal candidates with the limited amount of data available. The CKM matrix element $|V_{tb}|$ has been measured with an uncertainty of 4.2%, currently the world's most precise measurement, and can be constrained in the SM to $0.92 < |V_{tb}| \leq 1.0$ at 95% confidence level. Together with recent Higgs boson measurements this diminishes the possibility of a fourth quark generation.

The charge ratio measurement performed at $\sqrt{s} = 8$ TeV is consistent with several predictions made in the scope of this thesis with different PDFs. However, the uncertainties on the charge ratio are currently too large to distinguish between different PDFs or to pick a favorite.

The top quark polarization has been measured with an unfolding method developed in the scope of this thesis and is consistent with the SM predictions within the estimated uncertainties. With the current amount of data no further constraints on anomalous couplings than with measurements from W boson helicity are possible.

As the main focus of this thesis, the differential cross section of single top-quark production in the t-channel has been measured as a function of the transverse momentum p_{T} and the rapidity $|y|$ of the top quark using a dataset corresponding to a total integrated luminosity of 19.7 fb^{-1} collected by the CMS detector at a center-of-mass energy of $\sqrt{s} = 8$ TeV.

In order to obtain a signal-enriched sample a multivariate analysis employing a neural network has been trained. Detector effects and selection efficiencies have been corrected with an unfolding method. Closure tests have been performed on pseudo data in order to check that the bias introduced by the unfolding is negligible. The unfolded distributions are well described by three different NLO MC predictions within the estimated uncertainties. With the current amount of data, all three compared MC generators using different flavor schemes, 4FS or 5FS, describe the measured distributions remarkably well. No deviations from the SM as sign of new physics is visible in the measured distributions with the currently available amount of data.

Single top quark physics has drawn level with measurements from top quark pair production and entered the precision era. Measurements such as the differential cross section of single top-quark production in the t-channel presented in this thesis can be used to compare different QCD predictions for several kinematic variables and allow a better understanding of SM physics and the calibration of MC generators for the ongoing search for new physics beyond the SM.

8.2. Outlook

After the first two-year-long upgrade, the LHC was successfully resurrected again on Easter Sunday, and first test beams traversed the main ring consecutively in both directions with an upgraded center-of-mass energy. With an expected increased center-of-mass energy of $\sqrt{s} = 13$ TeV and an expected integrated luminosity of up to 100 fb^{-1} in Run II, a plethora of top quarks will be produced. With a large dataset like this, the methods developed and utilized in this thesis will allow the detailed study of the production and properties of single top quarks. With enough data, even the Higgs coupling to top quarks is accessible through associated production.

The analysis developed in this thesis can be enhanced through performing the differential cross section in a fiducial region. This will lessen the effects from the extrapolation of the measured cross section in the selected phase space to the total cross section. Another possible enhancement of this thesis and exciting prospect for many theorists is the measurement of the single top quark t-channel cross section differential in the transverse momentum and rapidity of the jet assigned to the second b quark. Although more work is needed to accomplish this, this measurement would for the first time enable to constrain the b quark PDF without data from DIS and with data directly obtained at the energy scale Q^2 relevant for the search of new physics.

Appendix

A. Statistical Methods

A.1. Best Linear Unbiased Estimator (BLUE)

The Best Linear Unbiased Estimator (BLUE) [66] method applies the Gauss-Markov theorem to correctly combine two or more measurements with uncertainties[1]. Like the name suggests the nature of the BLUE technique is that

- the solution is a linear combination of the individual estimates;
- the estimate is unbiased and
- has the smallest possible variance σ^2.

For a combination of two measurements, the aim is to find the linear combination $x = w_1 \cdot x_1 + w_2 \cdot x_2$ with the results x_i and the corresponding weights w_i. This is equivalent to the minimization of a χ^2-function while taking into account the full covariance matrix:

$$\chi^2 = \begin{pmatrix} x_1 - x & x_2 - x \end{pmatrix} \begin{pmatrix} \sigma_1^2 & \rho\sigma_1\sigma_2 \\ \rho\sigma_1\sigma_2 & \sigma_2^2 \end{pmatrix}^{-1} , \begin{pmatrix} x_1 - x \\ x_2 - x \end{pmatrix} \tag{A.1}$$

with the correlation ρ between the two measurements and their uncertainties σ_1 and σ_2. Minimizing this χ^2-function yields the two weights

$$w_1 = \frac{\sigma_2^2 - \rho\sigma_1\sigma_2}{\sigma_1^2 - 2\rho\sigma_1\sigma_2 + \sigma_2^2} , \tag{A.2}$$

and

$$w_2 = \frac{\sigma_1^2 - \rho\sigma_1\sigma_2}{\sigma_1^2 - 2\rho\sigma_1\sigma_2 + \sigma_2^2} . \tag{A.3}$$

---

[1] See `http://agiamann.web.cern.ch/agiamann/blue` for the implementation used in this thesis.

B. Event Shape Variables

Event shape variables [80,184] describe the geometry of a hadronic event. The momentum or sphericity tensor is defined as follows

$$S^{\alpha\beta} = \frac{\sum_i p_i^\alpha p_i^\beta}{\sum_i |\mathbf{p_i}|^2}\,, \tag{B.1}$$

where p_i^α is the momentum of the final state particle i of the event and $\alpha, \beta = 1, 2, 3$ correspond to the x, y and z components. Standard diagonalization of the tensor yields three eigenvalues $\lambda_1 \geq \lambda_2 \geq \lambda_3$ with $\lambda_1 + \lambda_2 + \lambda_3 = 1$.

The sphericity of an event is defined as

$$S = \frac{3}{2}(\lambda_2 + \lambda_3)\,, \tag{B.2}$$

and is a measure of the summed transverse momenta squared of the final state particles with respect to the event axis. S approaches 0 for 2-jet events and events with small transverse momenta and 1 for events with large multiplicity and isotropic phase-space distributions of the involved particles.

Aplanarity can distinguish between spherical and planar events and is defined as

$$A = \frac{3}{2}\lambda_3\,. \tag{B.3}$$

Aplanarity is constrained to the range $0 \leq A \leq \frac{1}{2}$ and measures the transverse momentum component out of the event plane. It can be used to distinguish between planar events, $A \approx 0$, and isotropic events, $A \approx \frac{1}{2}$.

The event shape variable C is a linear combination of the eigenvalues and defined as

$$C = 3(\lambda_1\lambda_2 + \lambda_1\lambda_3 + \lambda_2\lambda_3)\,. \tag{B.4}$$

and measures the 3-jet structure of an event. It vanishes for a perfect 2-jet event.

C. Input variables

C.1. Muon channel

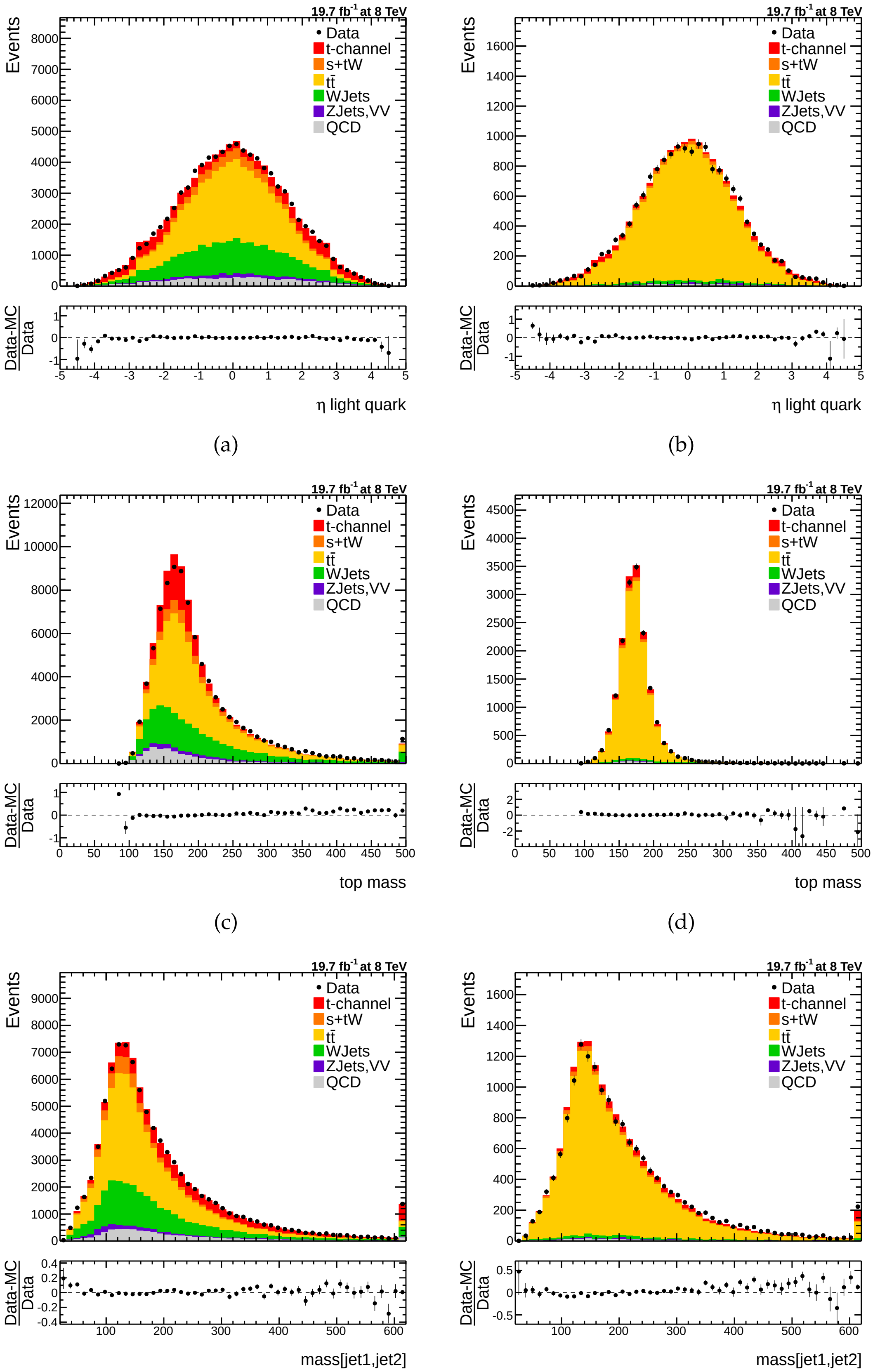

(a) (b)

(c) (d)

(e) (f)

Figure C.1.: Muon channel input variables. η_{lq}, $m_{\ell\nu\mathrm{b}}$ and $m_{\mathrm{jet1,jet2}}$.

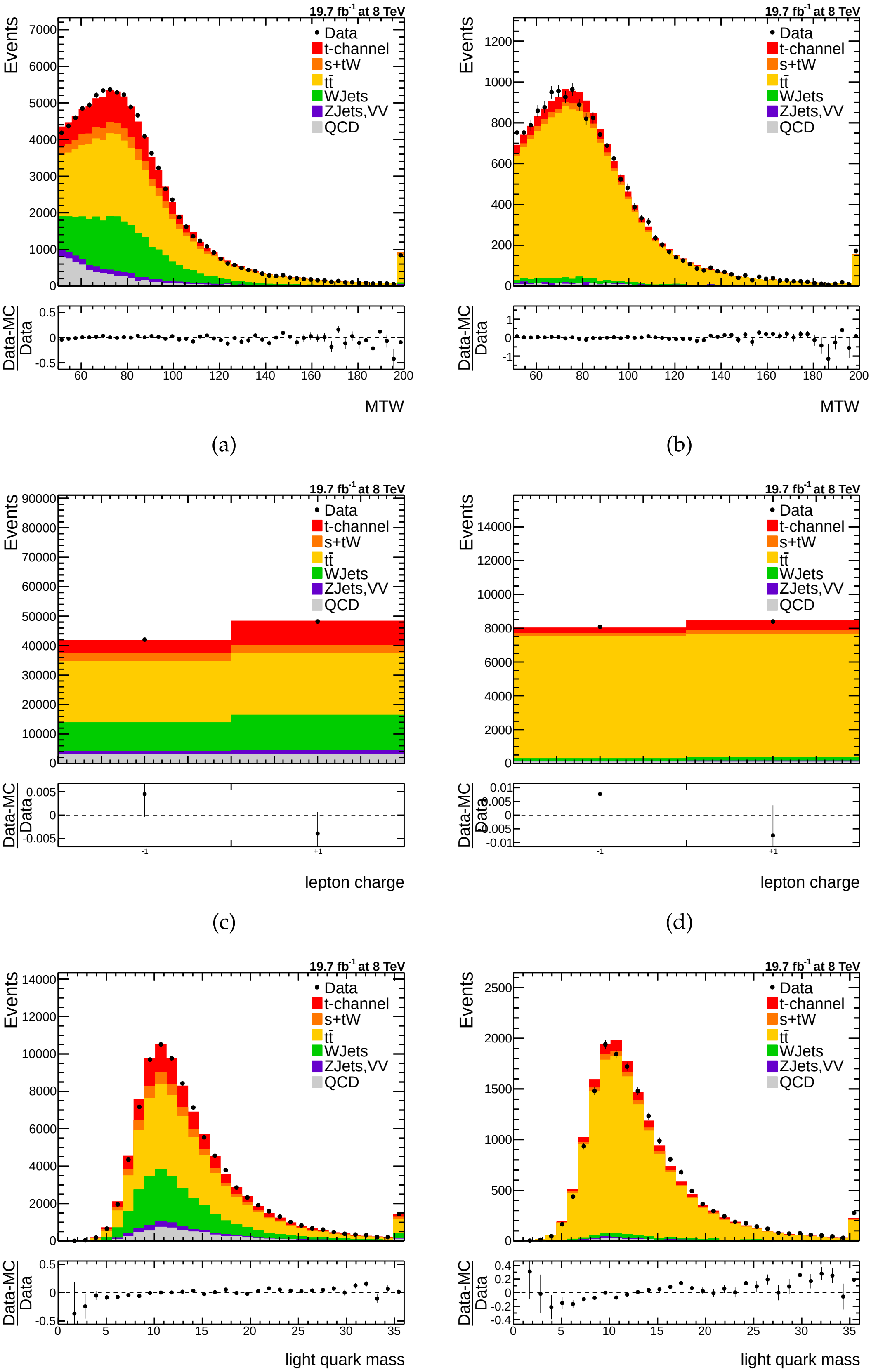

(a)

(b)

(c)

(d)

(e)

(f)

Figure C.2.: Muon channel input variables. $m_{\mathrm{T,W}}$, Q_{ℓ} and m_{lq}.

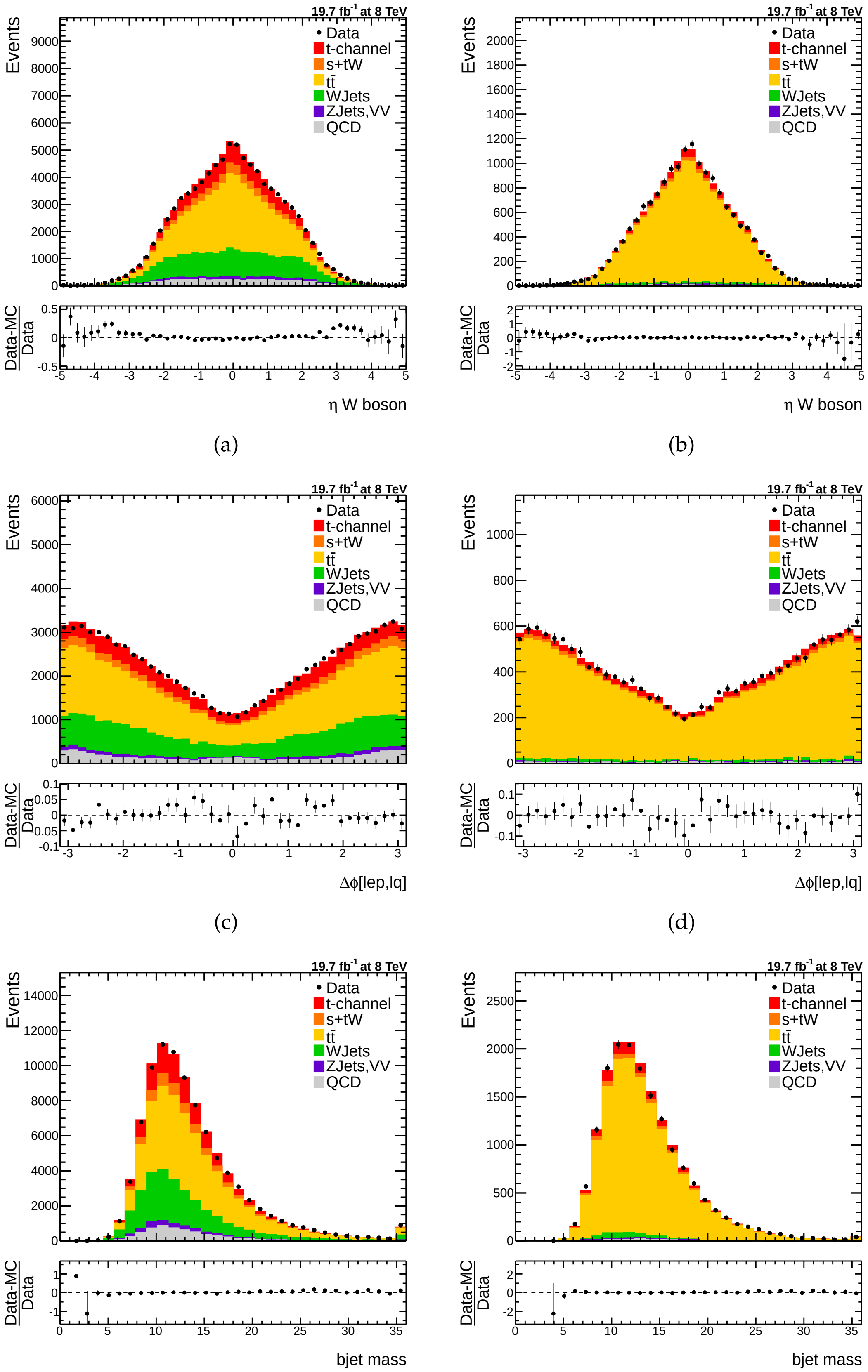

(a)

(b)

(c)

(d)

(e)

(f)

Figure C.3.: Muon channel input variables. η_W, $\Delta\phi[\ell, lq]$ and $m_{b_{top}}$.

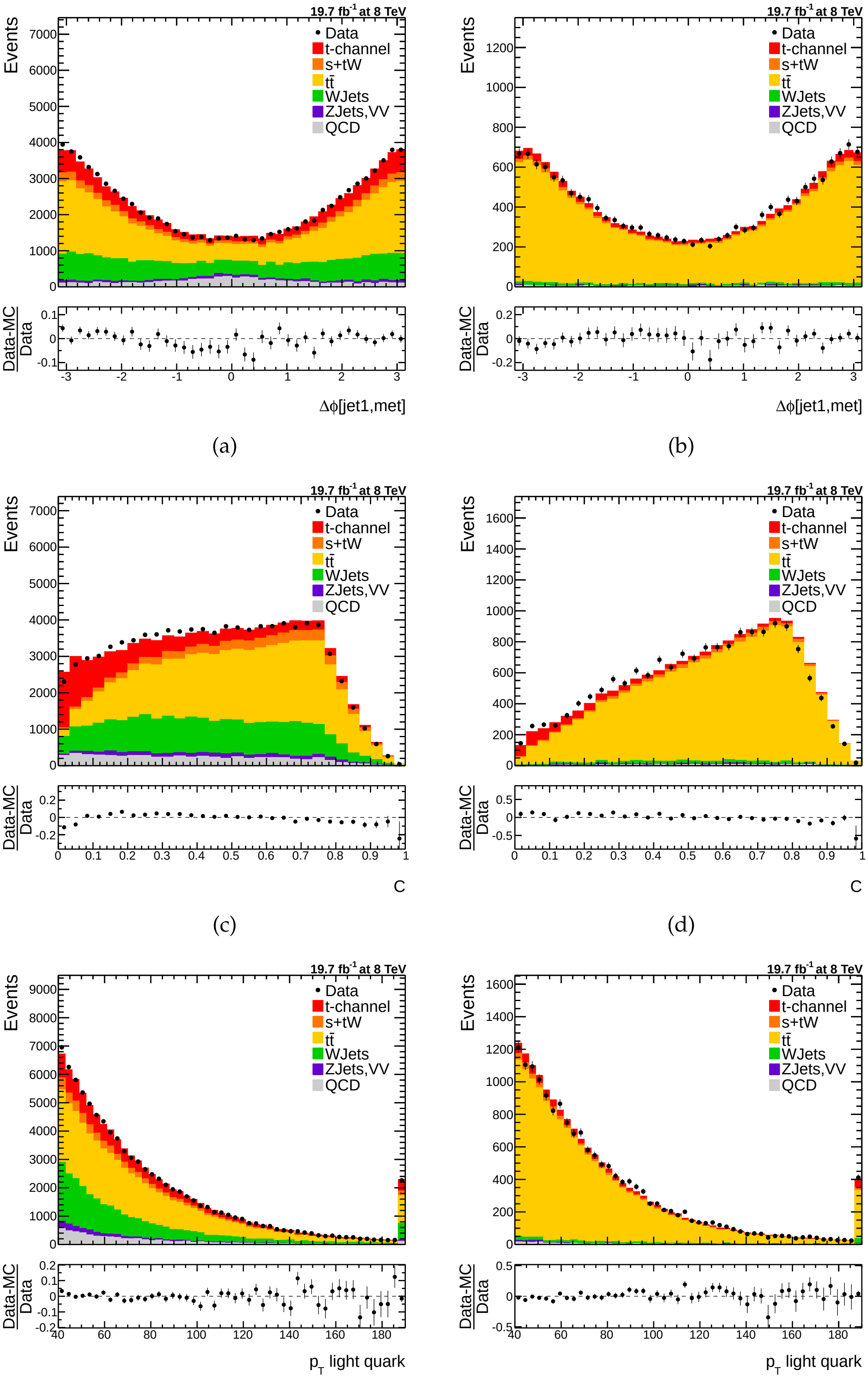

(a) (b)

(c) (d)

(e) (f)

Figure C.4.: Muon channel input variables. $\Delta\phi(jet1, \not{E}_T)$, C and $p_{T,lq}$.

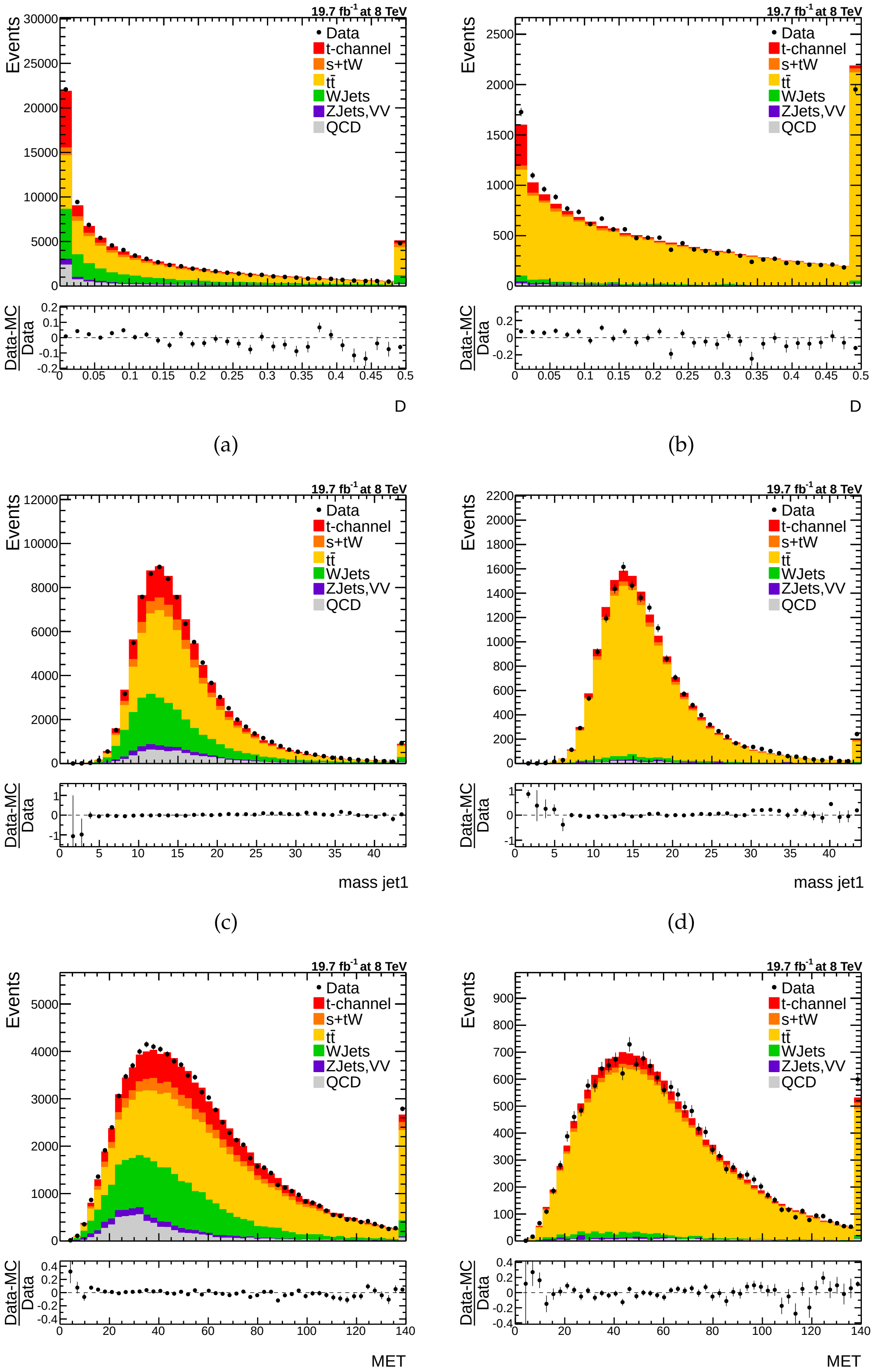

(a)

(b)

(c)

(d)

(e)

(f)

Figure C.5.: Muon channel input variables. D, m_{jet1} and $\not{E}_{\text{T}}$.

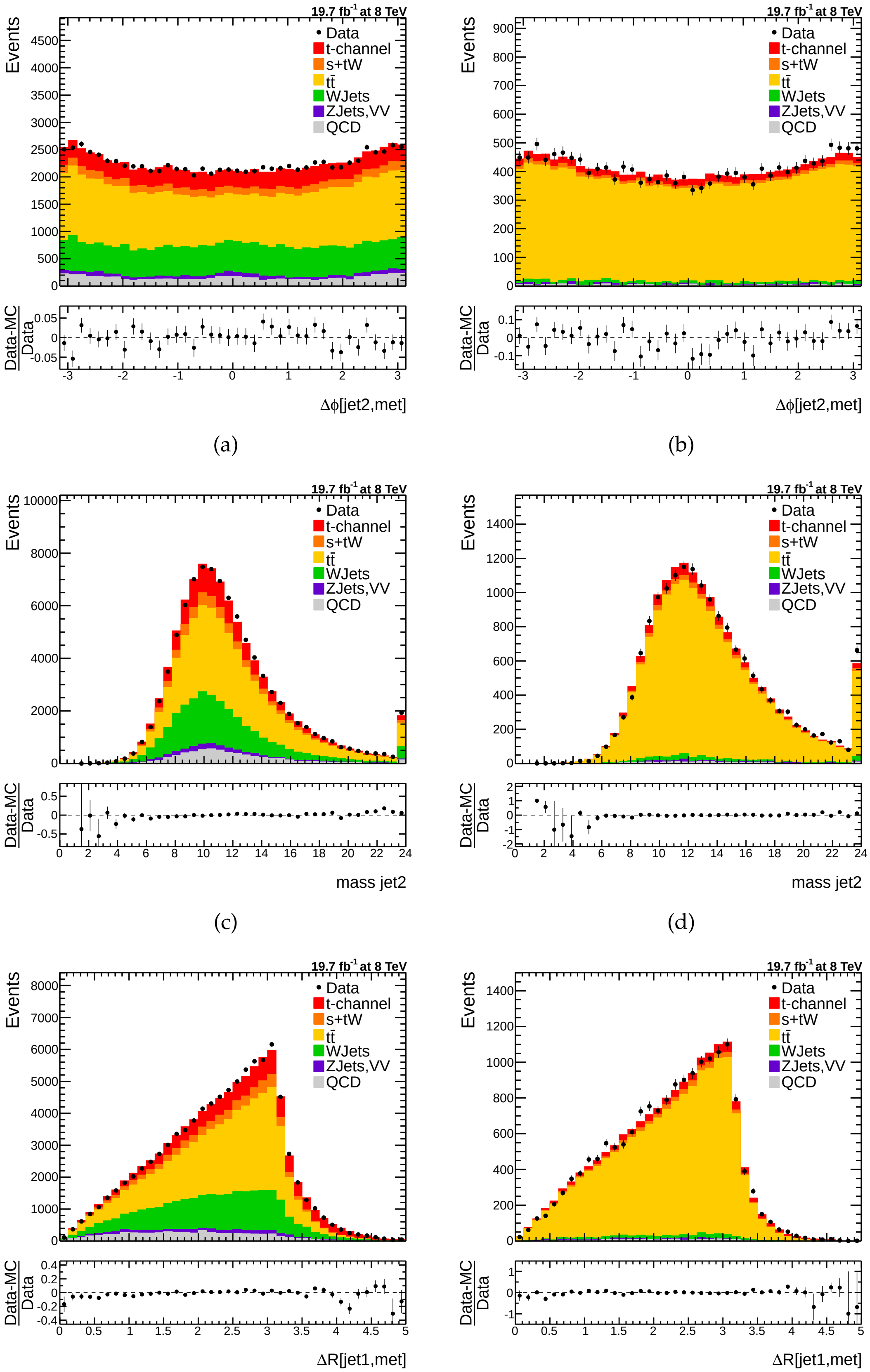

(a) (b)

(c) (d)

(e) (f)

Figure C.6.: Muon channel input variables. $\Delta\phi(jet2, \not{E}_{\mathrm{T}})$, m_{jet2} and $\Delta R(jet1, \not{E}_{\mathrm{T}})$.

C.2. Electron channel

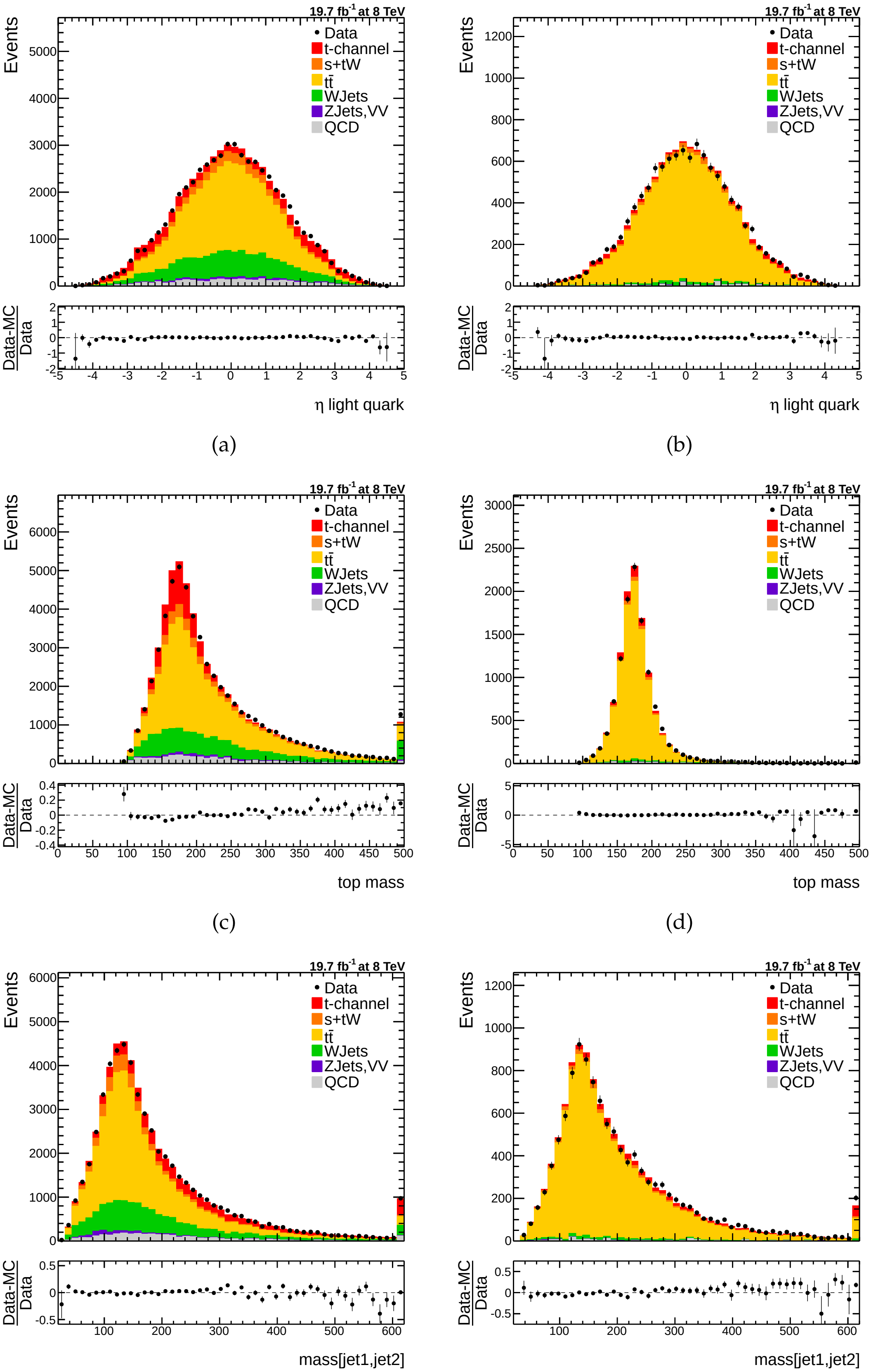

(a) (b)

(c) (d)

(e) (f)

Figure C.7.: Electron channel input variables. η_{lq}, $m_{\ell\nu\mathrm{b}}$ and $m_{\mathrm{jet1,jet2}}$.

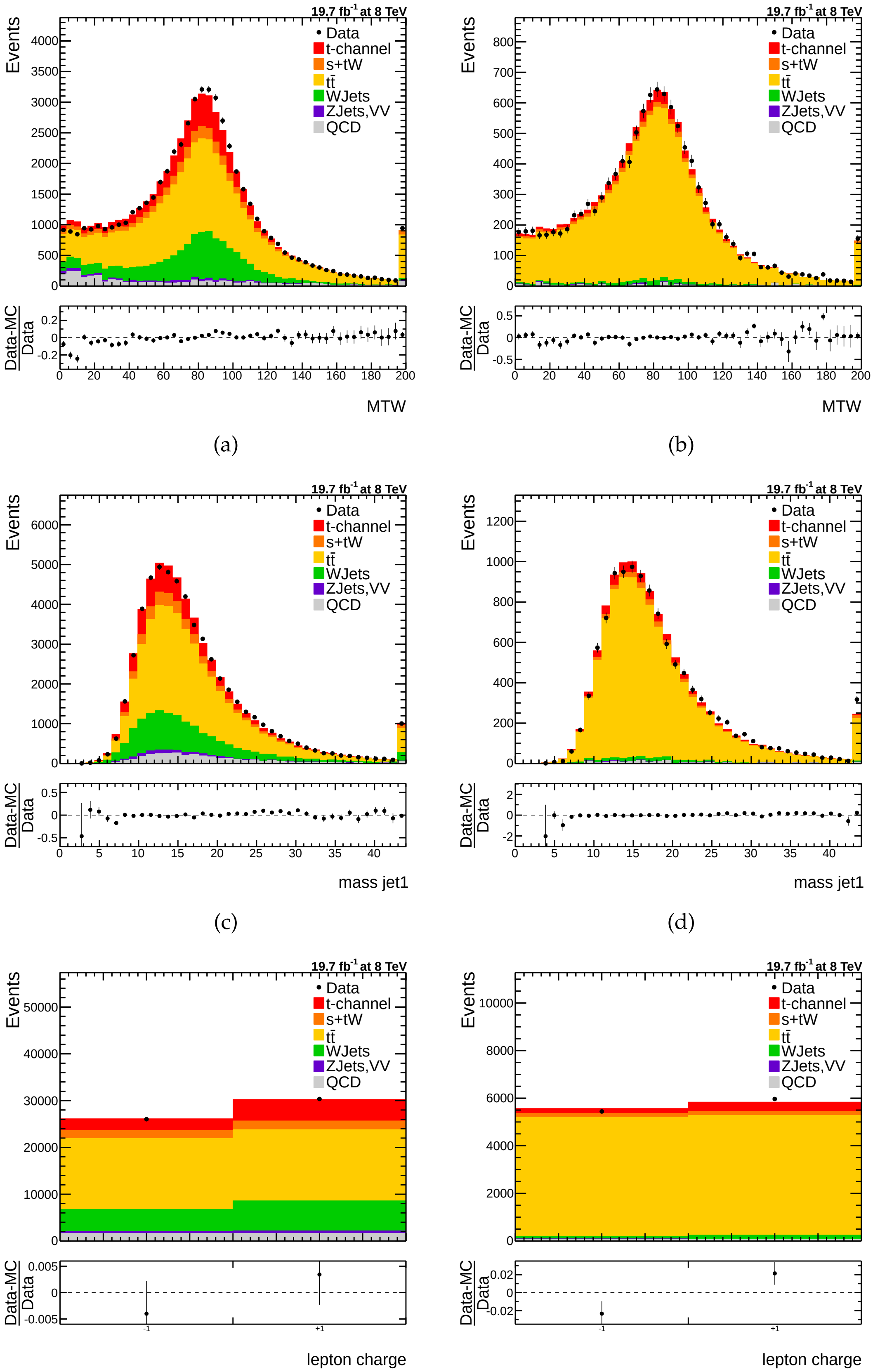

(a) (b)

(c) (d)

(e) (f)

Figure C.8.: Electron channel input variables. $m_{\mathrm{T,W}}$, m_{jet1} and Q_{ℓ}.

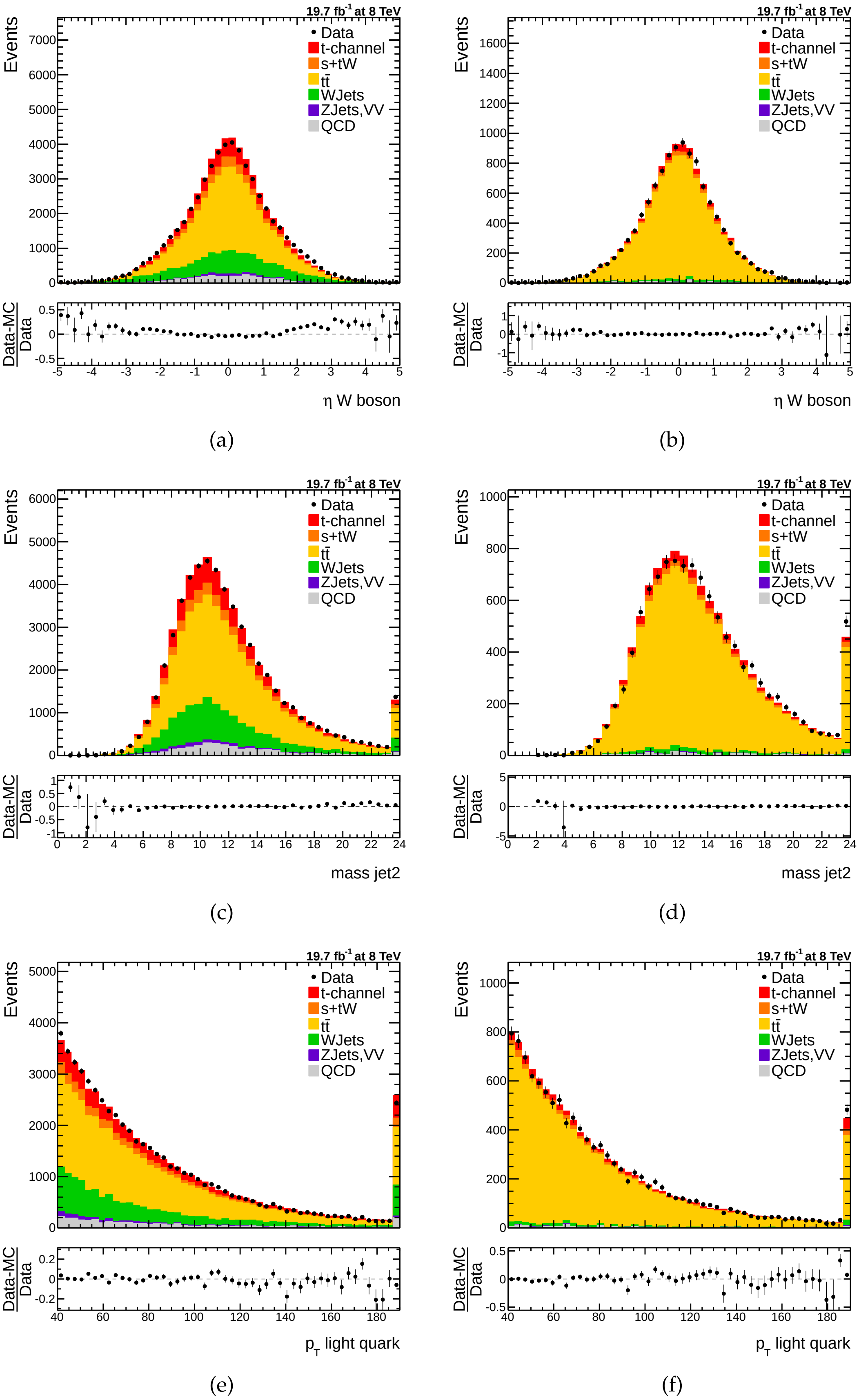

(a) (b)

(c) (d)

(e) (f)

Figure C.9.: Electron channel input variables. η_{W}, m_{jet2} and $p_{\mathrm{T,lq}}$.

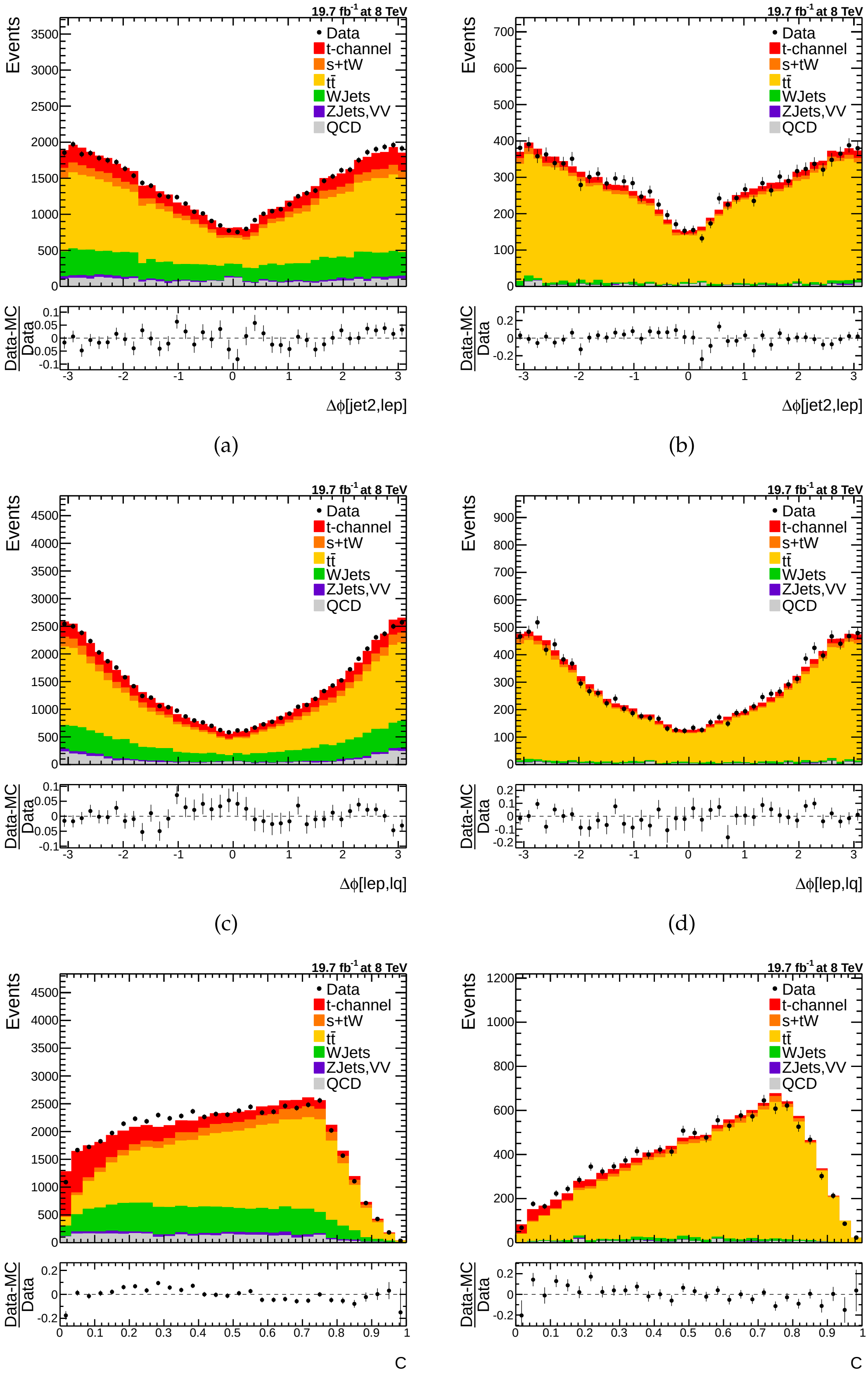

(a)

(b)

(c)

(d)

(e)

(f)

Figure C.10.: Electron channel input variables. $\Delta\phi[jet2, \ell]$, $\Delta\phi[\ell, lq]$ and C.

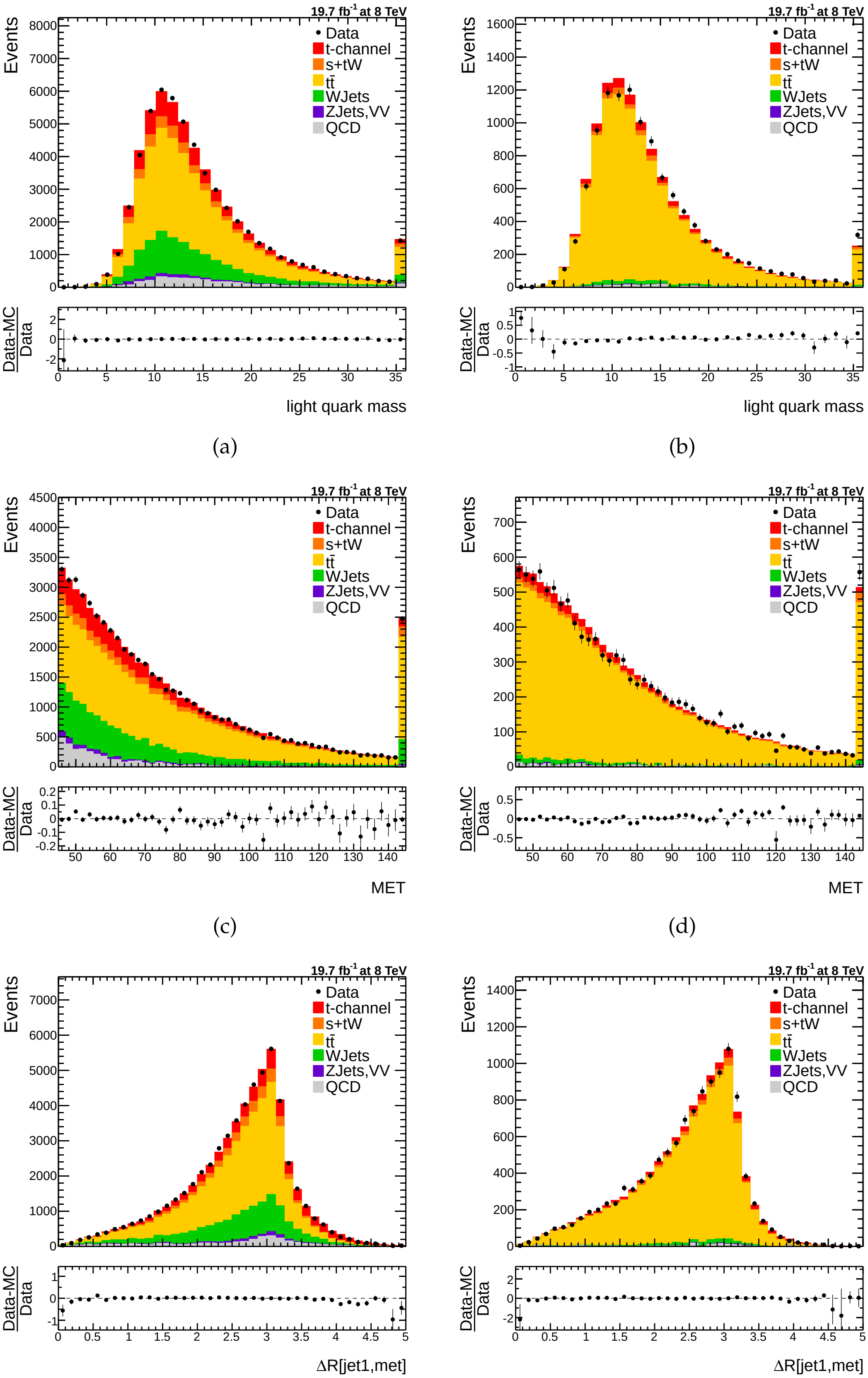

(a) (b)

(c) (d)

(e) (f)

Figure C.11.: Electron channel input variables. m_{lq}, $\not{E}_T$ and $\Delta R(jet1, \not{E}_T)$.

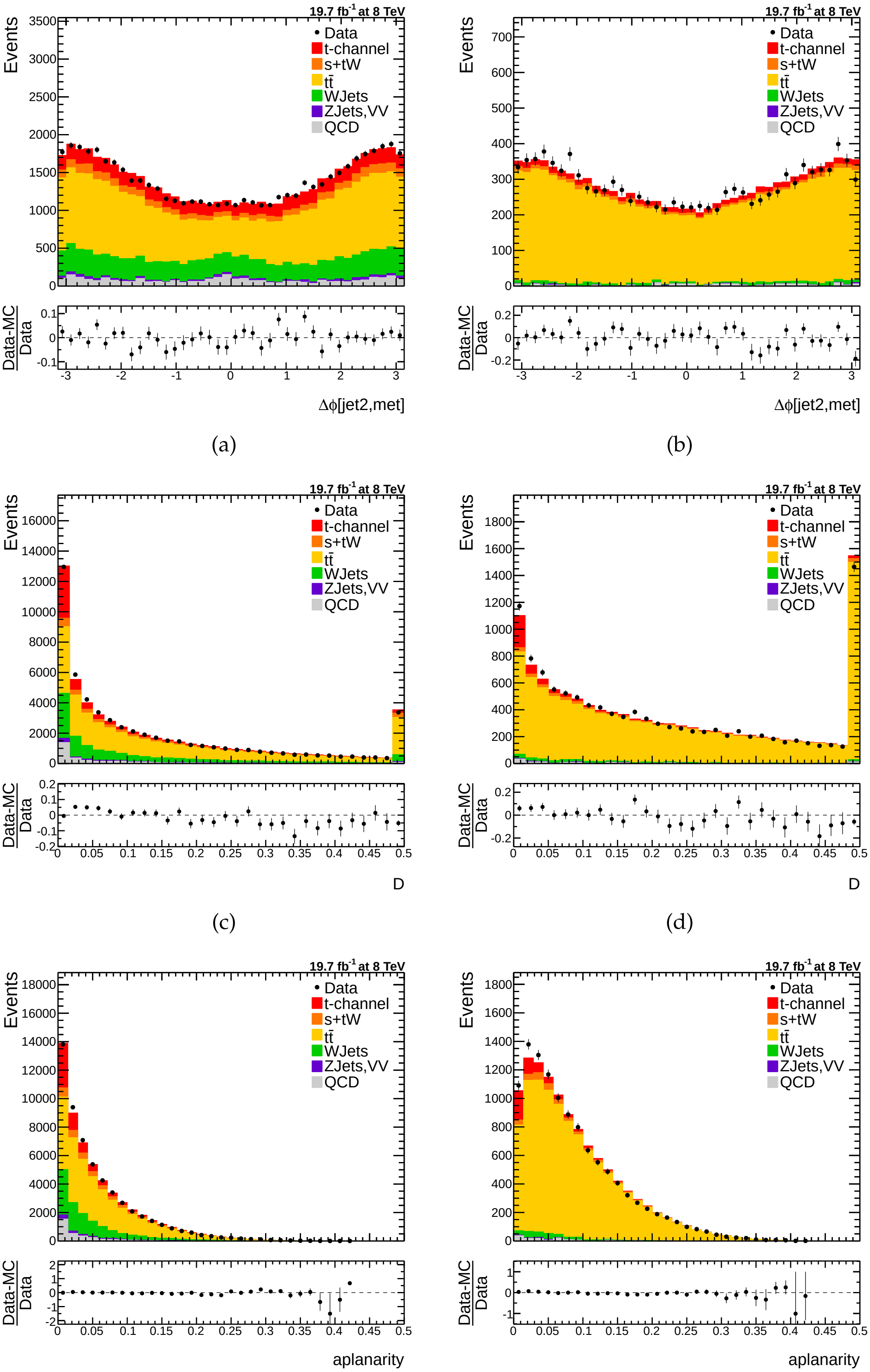

(a) (b)

(c) (d)

(e) (f)

Figure C.12.: Electron channel input variables. $\Delta\phi(jet2, \not{E}_{\mathrm{T}})$, D and A.

Bibliography

[1] A. Einstein, "Grundlage der Allgemeinen Relativitätstheorie," *Annalen Phys.* **49** (1916) 769–822.

[2] **Planck** Collaboration, P. Ade *et al.*, "Planck 2015 results. XIII. Cosmological parameters," `arXiv:1502.01589 [astro-ph.CO]`.

[3] **CMS** Collaboration, S. Chatrchyan *et al.*, "Observation of a new boson at a mass of 125 GeV with the CMS experiment at the LHC," *Phys.Lett.* **B716** (2012) 30–61, `arXiv:1207.7235 [hep-ex]`.

[4] **ATLAS** Collaboration, G. Aad *et al.*, "Observation of a new particle in the search for the Standard Model Higgs boson with the ATLAS detector at the LHC," *Phys.Lett.* **B716** (2012) 1–29, `arXiv:1207.7214 [hep-ex]`.

[5] D. Griffiths, *Introduction to Elementary Particles*. Wiley-VCH, 2008.

[6] C. Burgess and G. Moore, *The Standard Model – A Primer*. Cambridge University Press, 2006.

[7] G. t. Hooft, "The Evolution of Quantum Field Theory, From QED to Grand Unification," `arXiv:1503.05007 [hep-th]`.

[8] E. Noether, "Invariante Variationsprobleme," *Nachrichten von der Gesellschaft der Wissenschaften zu Göttingen, Mathematisch-Physikalische Klasse* **1918** (1918) 235–257. `http://eudml.org/doc/59024`.

[9] S. L. Glashow, "Partial Symmetries of Weak Interactions," *Nucl. Phys.* **22** (1961) 579–588.

[10] S. Weinberg, "A Model of Leptons," *Phys. Rev. Lett.* **19** (1967) 1264–1266.

[11] A. Salam and J. C. Ward, "Electromagnetic and Weak Interactions," *Phys. Lett.* **13** (1964) 168–171.

[12] **Particle Data Group** Collaboration, K. A. Olive *et al.*, "Review of Particle Physics," *Chin. Phys. C* **38** (2014) 090001.

[13] **KATRIN** Collaboration, J. Angrik *et al.*, "KATRIN design report 2004,".

[14] **ATLAS** Collaboration, **CDF** Collaboration, **CMS** Collaboration, **DØ** Collaboration, "First combination of Tevatron and LHC measurements of the top-quark mass," `arXiv:1403.4427 [hep-ex]`.

[15] P. W. Higgs, "Broken symmetries, massless particles and gauge fields," *Phys. Lett.* **12** no. 2, 132–133.

[16] F. Englert and R. Brout, "Broken Symmetry and the Mass of Gauge Vector Mesons," *Phys. Rev. Lett.* **13** 321–323.

[17] G. Guralnik, C. Hagen, and T. Kibble, "Global Conservation Laws and Massless Particles," *Phys. Rev. Lett.* **13** (1964) 585–587.

[18] P. W. Higgs, "Spontaneous Symmetry Breakdown without Massless Bosons," *Phys. Rev.* **145** 1156–1163.

[19] L. Alvarez-Gaume and J. Ellis, "Eyes on a prize particle," *Nature Phys.* **7** no. 1, (2011) 2–3. `https://cds.cern.ch/record/1399903`. Editorial Material.

[20] Y. Nambu, "Quasi-Particles and Gauge Invariance in the Theory of Superconductivity," *Phys. Rev.* **117** (Feb, 1960) 648–663. `http://link.aps.org/doi/10.1103/PhysRev.117.648`.

[21] J. Goldstone, "Field theories with ≪ Superconductor ≫ solutions," *Il Nuovo Cimento* **19** no. 1, (1961) 154–164. `http://dx.doi.org/10.1007/BF02812722`.

[22] J. Goldstone, A. Salam, and S. Weinberg, "Broken Symmetries," *Phys. Rev.* **127** (Aug, 1962) 965–970. `http://link.aps.org/doi/10.1103/PhysRev.127.965`.

[23] N. Cabibbo, "Unitary Symmetry and Leptonic Decays," *Phys. Rev. Lett.* **10** (1963) 531–533.

[24] M. Kobayashi and T. Maskawa, "CP Violation in the Renormalizable Theory of Weak Interaction," *Prog.Theor.Phys.* **49** (1973) 652–657.

[25] R. P. Feynman, "The Theory of Positrons," *Physical Review* **76** (Sept., 1949) 749–759.

[26] W.J. Stirling. Private communication.

[27] Y. L. Dokshitzer, "Calculation of the Structure Functions for Deep Inelastic Scattering and e+ e- Annihilation by Perturbation Theory in Quantum Chromodynamics.," *Sov.Phys.JETP* **46** (1977) 641–653.

[28] V. Gribov and L. Lipatov, "Deep inelastic e p scattering in perturbation theory," *Sov.J.Nucl.Phys.* **15** (1972) 438–450.

[29] G. Altarelli and G. Parisi, "Asymptotic Freedom in Parton Language," *Nucl.Phys.* **B126** (1977) 298.

[30] H.-L. Lai, M. Guzzi, J. Huston, Z. Li, P. M. Nadolsky, *et al.*, "New parton distributions for collider physics," *Phys.Rev.* **D82** (2010) 074024, `arXiv:1007.2241 [hep-ph]`.

[31] **CDF** Collaboration, "Observation of Top Quark Production in $\overline{p}p$ Collisions with the Collider Detector at Fermilab," *Phys. Rev. Lett.* **74** (Apr, 1995) 2626–2631. `http://link.aps.org/doi/10.1103/PhysRevLett.74.2626`.

[32] **DØ** Collaboration, "Search for High Mass Top Quark Production in $p\overline{p}$ Collisions at $\sqrt{s} =$ 1.8 TeV," *Phys. Rev. Lett.* **74** (Mar, 1995) 2422–2426. `http://link.aps.org/doi/10.1103/PhysRevLett.74.2422`.

[33] M. Czakon, P. Fiedler, and A. Mitov, "Total Top-Quark Pair-Production Cross Section at Hadron Colliders Through $\mathcal{O}(\alpha_S^4)$," *Phys.Rev.Lett.* **110** (2013) 252004, `arXiv:1303.6254 [hep-ph]`.

[34] Z. Bern, V. Del Duca, W. B. Kilgore, and C. R. Schmidt, "The infrared behavior of one loop QCD amplitudes at next-to-next-to leading order," *Phys.Rev.* **D60** (1999) 116001, `arXiv:hep-ph/9903516 [hep-ph]`.

[35] S. Catani and M. Grazzini, "The soft gluon current at one loop order," *Nucl.Phys.* **B591** (2000) 435–454, `arXiv:hep-ph/0007142 [hep-ph]`.

[36] S. S. Willenbrock and D. A. Dicus, "Production of Heavy Quarks from W Gluon Fusion," *Phys.Rev.* **D34** (1986) 155.

[37] S. Mandelstam, "Determination of the Pion-Nucleon Scattering Amplitude from Dispersion Relations and Unitarity. General Theory," *Physical Review* **112** (Nov., 1958) 1344–1360.

[38] **CDF** Collaboration, T. Aaltonen *et al.*, "Observation of Electroweak Single Top Quark Production," *Phys. Rev. Lett.* **103** (2009) 092002, `arXiv:0903.0885 [hep-ex]`.

[39] **DØ** Collaboration, V. M. Abazov *et al.*, "Observation of Single Top Quark Production," *Phys. Rev. Lett.* **103** (2009) 092001, `arXiv:0903.0850 [hep-ex]`.

[40] N. Kidonakis, "Top Quark Production," `arXiv:1311.0283 [hep-ph]`.

[41] M. Aliev, H. Lacker, U. Langenfeld, S. Moch, P. Uwer, *et al.*, "HATHOR: HAdronic Top and Heavy quarks crOss section calculatoR," *Comput.Phys.Commun.* **182** (2011) 1034–1046, `arXiv:1007.1327 [hep-ph]`.

[42] P. Kant, O. Kind, T. Kintscher, T. Lohse, T. Martini, *et al.*, "HATHOR for single top-quark production: Updated predictions and uncertainty estimates for single top-quark production in hadronic collisions," `arXiv:1406.4403 [hep-ph]`.

[43] M. Botje, J. Butterworth, A. Cooper-Sarkar, A. de Roeck, J. Feltesse, *et al.*, "The PDF4LHC Working Group Interim Recommendations," `arXiv:1101.0538 [hep-ph]`.

[44] A. Martin, W. Stirling, R. Thorne, and G. Watt, "Parton distributions for the LHC," *Eur.Phys.J.* **C63** (2009) 189–285, `arXiv:0901.0002 [hep-ph]`.

[45] A. Martin, W. Stirling, R. Thorne, and G. Watt, "Uncertainties on alpha(S) in global PDF analyses and implications for predicted hadronic cross sections," *Eur.Phys.J.* **C64** (2009) 653–680, `arXiv:0905.3531 [hep-ph]`.

[46] R. D. Ball, V. Bertone, S. Carrazza, C. S. Deans, L. Del Debbio, *et al.*, "Parton distributions with LHC data," *Nucl.Phys.* **B867** (2013) 244–289, `arXiv:1207.1303 [hep-ph]`.

[47] TopLHCWG recommended predictions for single top cross sections, https://twiki.cern.ch/twiki/bin/view/LHCPhysics/SingleTopRefXsec.

[48] M. Brucherseifer, F. Caola, and K. Melnikov, "On the NNLO QCD corrections to single-top production at the LHC," *Phys.Lett.* **B736** (2014) 58–63, `arXiv:1404.7116 [hep-ph]`.

[49] **CMS** Collaboration, S. Chatrchyan *et al.*, "Observation of the associated production of a single top quark and a W boson in pp collisions at $\sqrt{s}$ =8 TeV," *Phys.Rev.Lett.* **112** no. 23, (2014) 231802, `arXiv:1401.2942 [hep-ex]`.

[50] C. D. White, S. Frixione, E. Laenen, and F. Maltoni, "Isolating Wt production at the LHC," *JHEP* **0911** (2009) 074, `arXiv:0908.0631 [hep-ph]`.

[51] J. Alwall, R. Frederix, J.-M. Gérard, A. Giammanco, M. Herquet, S. Kalinin, E. Kou, V. Lemaitre, and F. Maltoni, "Is Vtb $\simeq$ 1?," *The European Physical Journal C* **49** no. 3, (2007) 791–801. `http://dx.doi.org/10.1140/epjc/s10052-006-0137-y`.

[52] A. Djouadi and A. Lenz, "Sealing the fate of a fourth generation of fermions," *Phys.Lett.* **B715** (2012) 310–314, `arXiv:1204.1252 [hep-ph]`.

[53] O. Eberhardt, G. Herbert, H. Lacker, A. Lenz, A. Menzel, *et al.*, "Impact of a Higgs boson at a mass of 126 GeV on the standard model with three and four fermion generations," *Phys.Rev.Lett.* **109** (2012) 241802, `arXiv:1209.1101 [hep-ph]`.

[54] S. Alekhin, A. Djouadi, and S. Moch, "The top quark and Higgs boson masses and the stability of the electroweak vacuum," *Phys.Lett.* **B716** (2012) 214–219, `arXiv:1207.0980 [hep-ph]`.

[55] M. Jezabek and J. H. Kühn, "QCD Corrections to Semileptonic Decays of Heavy Quarks," *Nucl.Phys.* **B314** (1989) 1.

[56] A. Czarnecki, J. G. Korner, and J. H. Piclum, "Helicity fractions of W bosons from top quark decays at NNLO in QCD," *Phys.Rev.* **D81** (2010) 111503, `arXiv:1005.2625 [hep-ph]`.

[57] M. Jezabek and J. H. Kühn, "V-A tests through leptons from polarized top quarks," *Phys.Lett.* **B329** (1994) 317–324, `arXiv:hep-ph/9403366 [hep-ph]`.

[58] G. Mahlon and S. J. Parke, "Single top quark production at the LHC: Understanding spin," *Phys.Lett.* **B476** (2000) 323–330, `arXiv:hep-ph/9912458 [hep-ph]`.

[59] G. Mahlon, "Observing spin correlations in single top production and decay," `arXiv:hep-ph/0011349 [hep-ph]`.

[60] **ATLAS** Collaboration, "Observation of t Channel Single Top-Quark Production in pp Collisions at $\sqrt{s} = 7$ TeV with the ATLAS detector." ATLAS-CONF-2011-088, ATLAS-COM-CONF-2011-097, 2011.

[61] **CMS** Collaboration, S. Chatrchyan *et al.*, "Measurement of the t-channel single top quark production cross section in pp collisions at $\sqrt{s} = 7$ TeV," *Phys.Rev.Lett.* **107** (2011) 091802, `arXiv:1106.3052 [hep-ex]`.

[62] **CMS** Collaboration, S. Chatrchyan *et al.*, "Measurement of the single-top-quark t-channel cross section in pp collisions at $\sqrt{s} = 7$ TeV," *JHEP* **1212** (2012) 035, `arXiv:1209.4533 [hep-ex]`.

[63] **CMS** Collaboration, V. Khachatryan *et al.*, "Measurement of the t-channel single-top-quark production cross section and of the $\mid V_{tb} \mid$ CKM matrix element in pp collisions at $\sqrt{s}$= 8 TeV," *JHEP* **1406** (2014) 090, `arXiv:1403.7366 [hep-ex]`.

[64] **CMS** Collaboration, S. Röcker *et al.*, "Measurement of the t-channel single top quark cross section at $\sqrt{s} = 7$ TeV using neural networks," CMS Internal Note 2011/191, 2011.

[65] S. Röcker, "Prospects for the Observation of Single Top Quark Production with the CMS Experiment using Neural Networks," Diploma thesis, Karlsruhe Institute of Technology, 2011. IEKP-KA/2011-06.

[66] L. Lyons, D. Gibaut, and P. Clifford, "How to Combine Correlated Estimates of a Single Physical Quantity," *Nucl.Instrum.Meth.* **A270** (1988) 110.

[67] J. M. Campbell, R. Frederix, F. Maltoni, and F. Tramontano, "NLO predictions for t-channel production of single top and fourth generation quarks at hadron colliders," *JHEP* **0910** (2009) 042, `arXiv:0907.3933 [hep-ph]`.

[68] N. Kidonakis, "Next-to-next-to-leading-order collinear and soft gluon corrections for t-channel single top quark production," *Phys.Rev.* **D83** (2011) 091503, `arXiv:1103.2792 [hep-ph]`.

[69] J. A. Aguilar-Saavedra, "A minimal set of top anomalous couplings," *Nucl. Phys. B* **812** (2009) 181, `arXiv:0811.3842 [hep-ph]`.

[70] G. L. Kane, G. A. Ladinsky, and C. P. Yuan, "Using the top quark for testing standard model polarization and CP predictions," *Phys. Rev. D* **45** (1992) 124.

[71] T. G. Rizzo, "Single top quark production as a probe for anomalous moments at hadron colliders," *Phys. Rev. D* **53** (1996) 6218, `arXiv:hep-ph/9506351 [hep-ph]`.

[72] G. J. Feldman and R. D. Cousins, "Unified approach to the classical statistical analysis of small signals," *Phys. Rev. D* **57** (Apr, 1998) 3873–3889. `http://link.aps.org/doi/10.1103/PhysRevD.57.3873`.

[73] **DØ** Collaboration, V. M. Abazov *et al.*, "An Improved determination of the width of the top quark," *Phys.Rev.* **D85** (2012) 091104, `arXiv:1201.4156 [hep-ex]`.

[74] **CMS** Collaboration, "Measurement of the ratio $B(t \to Wb)/B(t \to Wq)$ in pp collisions at $\sqrt{s} = 8$ TeV," *Phys. Lett. B* **736** (2014) .

[75] **CDF** Collaboration, "Measurement of single top polarization with 3.2/fb." CDF NOTE 9920, 2009.

[76] J. Pata, "Measurement of top quark polarisation in t-channel single top production with the CMS detector," Master's thesis, University of Tartu, 2014. `http://hdl.handle.net/10062/41806`.

[77] S. Alioli, P. Nason, C. Oleari, and E. Re, "A general framework for implementing NLO calculations in shower Monte Carlo programs: the POWHEG BOX," *JHEP* **1006** (2010) 043, `arXiv:1002.2581 [hep-ph]`.

[78] S. Alioli, P. Nason, C. Oleari, and E. Re, "NLO single-top production matched with shower in POWHEG: s- and t-channel contributions," *JHEP* **0909** (2009) 111, `arXiv:0907.4076 [hep-ph]`.

[79] S. Frixione, P. Nason, and C. Oleari, "Matching NLO QCD computations with Parton Shower simulations: the POWHEG method," *JHEP* **0711** (2007) 070, `arXiv:0709.2092 [hep-ph]`.

[80] T. Sjöstrand, S. Mrenna, and P. Z. Skands, "PYTHIA 6.4 Physics and Manual," *JHEP* **0605** (2006) 026, `arXiv:hep-ph/0603175 [hep-ph]`.

[81] S. Jadach, J. H. Kühn, and Z. Was, "TAUOLA: A Library of Monte Carlo programs to simulate decays of polarized tau leptons," *Comput.Phys.Commun.* **64** (1990) 275–299.

[82] E. Boos, M. Dubinin, V. Edneral, V. Ilyin, A. Kryukov, A. Pukhov, A. Rodionov, V. Savrin, D. Slavnov, and A. Taranov, "CompHEP - computer system for calculation of particle collisions at high energies ," *SINP MSU* **report 89-63/140** (1989) .

[83] E. Boos *et al.*, "Method for simulating electroweak top-quark production events in the NLO approximation: SingleTop event generator," *Phys.Atom.Nucl.* **69, 8** (2006) 1317.

[84] S. Schmitt, “TUnfold, an algorithm for correcting migration effects in high energy physics,” *Journal of Instrumentation* **7** no. 10, (2012) T10003.

[85] A. Valassi and R. Chierici, “Information and treatment of unknown correlations in the combination of measurements using the BLUE method,” *Eur.Phys.J.* **C74** (2014) 2717, `arXiv:1307.4003 [physics.data-an]`.

[86] J. Gruschke, *Observation of Top Quarks and First Measurement of the $t\bar{t}$ Production Cross Section at a Centre-Of-Mass Energy of 7 TeV with the CMS Experiment at the LHC*. PhD thesis, Karlsruhe Institute of Technology, 2011. IEKP-KA/2011-04.

[87] **ATLAS** Collaboration, G. Aad *et al.*, “The ATLAS Experiment at the CERN Large Hadron Collider,” *Journal of Instrumentation* **3** no. 08, (2008) S08003. `http://stacks.iop.org/1748-0221/3/i=08/a=S08003`.

[88] **CMS** Collaboration, S. Chatrchyan *et al.*, “The CMS experiment at the CERN LHC,” *JINST* **3** no. 08, (2008) S08004.

[89] **LHCb** Collaboration, J. Alves, A. Augusto *et al.*, “The LHCb Detector at the LHC,” *JINST* **3** (2008) S08005.

[90] **ALICE** Collaboration, K. Aamodt *et al.*, “The ALICE experiment at the CERN LHC,” *Journal of Instrumentation* **3** no. 08, (2008) S08002. `http://stacks.iop.org/1748-0221/3/i=08/a=S08002`.

[91] M. Benedikt, P. Collier, V. Mertens, J. Poole, and K. Schindl, “LHC Design Report. 3. The LHC injector chain,” Tech. Rep. CERN-2004-003-V-3, CERN-2004-003, 2004.

[92] `https://twiki.cern.ch/twiki/bin/view/CMSPublic/LumiPublicResults`.

[93] T. Sakuma and T. McCauley, “Detector and Event Visualization with SketchUp at the CMS Experiment,” *J.Phys.Conf.Ser.* **513** (2014) 022032, `arXiv:1311.4942 [physics.ins-det]`.

[94] **CMS** Collaboration, V. Karimäki, M. Mannelli, P. Siegrist, H. Breuker, A. Caner, R. Castaldi, K. Freudenreich, G. Hall, R. Horisberger, M. Huhtinen, and A. Cattai, *The CMS tracker system project: Technical Design Report*. Technical Design Report CMS. CERN, Geneva, 1997. `http://cds.cern.ch/record/368412`.

[95] **CMS** Collaboration, *The CMS tracker: addendum to the Technical Design Report*. Technical Design Report CMS. CERN, Geneva, 2000. `https://cds.cern.ch/record/490194`.

[96] P. Adzic, “Energy resolution of the barrel of the CMS Electromagnetic Calorimeter,” *Journal of Instrumentation* **2** no. 04, (2007) P04004. `http://stacks.iop.org/1748-0221/2/i=04/a=P04004`.

[97] **CMS** Collaboration, S. Chatrchyan *et al.*, "Energy Calibration and Resolution of the CMS Electromagnetic Calorimeter in pp Collisions at $\sqrt{s} = 7$ TeV," *JINST* **8** (2013) P09009, `arXiv:1306.2016 [hep-ex]`.

[98] **CMS** Collaboration, G. L. Bayatian *et al.*, *CMS Physics: Technical Design Report Volume 1: Detector Performance and Software*. Technical Design Report CMS. CERN, Geneva, 2006. `http://cds.cern.ch/record/922757`.

[99] **CMS** Collaboration, *The CMS muon project: Technical Design Report*. Technical Design Report CMS. CERN, Geneva, 1997. `https://cds.cern.ch/record/343814`.

[100] A. Scheurer *et al.*, "German contributions to the CMS computing infrastructure," *Journal of Physics: Conference Series* **219** no. 6, (2010) 062064. `http://stacks.iop.org/1742-6596/219/i=6/a=062064`.

[101] I. Bird, K. Bos, N. Brook, D. Duellmann, C. Eck, *et al.*, "LHC computing Grid. Technical design report," tech. rep., 2005.

[102] **CMS** Collaboration, G. L. Bayatyan, M. Della Negra, L. Foà, A. Hervé, and A. Petrilli, *CMS computing: Technical Design Report*. Technical Design Report CMS. CERN, Geneva, 2005. `http://cds.cern.ch/record/838359`.

[103] V. Büge, V. Mauch, G. Quast, A. Scheurer, and A. Trunov, "Site specific monitoring of multiple information systems – the HappyFace Project," *Journal of Physics: Conference Series* **219** no. 6, (2010) 062057. `http://stacks.iop.org/1742-6596/219/i=6/a=062057`.

[104] S. Röcker, A. Burgmeier, M. Heinrich, G. Quast, G. Vollmer, and M. Zvada, "Meta-Monitoring with the Happyface Project," *Distributed Computing and Grid-technologies in Science and Education: Proceedings of the 5th Int. Conf.* (2012) . `http://grid2012.jinr.ru/docs/grid2012.pdf`.

[105] **CMS** Collaboration, "Particle-Flow Event Reconstruction in CMS and Performance for Jets, Taus, and MET," Tech. Rep. CMS-PAS-PFT-09-001, 2009.

[106] **CMS** Collaboration, "Commissioning of the Particle-Flow reconstruction in Minimum-Bias and Jet Events from pp Collisions at 7 TeV," Tech. Rep. CMS-PAS-PFT-10-002, 2010.

[107] **CMS** Collaboration, "Commissioning of the Particle-flow Event Reconstruction with the first LHC collisions recorded in the CMS detector," Tech. Rep. CMS-PAS-PFT-10-001, 2010.

[108] **CMS** Collaboration, "Description and performance of track and primary-vertex reconstruction with the CMS tracker," *Journal of Instrumentation* **9** no. 10, (2014) P10009. `http://stacks.iop.org/1748-0221/9/i=10/a=P10009`.

[109] **CMS** Collaboration, "CMS Physics Technical Design Report, Volume II: Physics Performance," *Journal of Physics G: Nuclear and Particle Physics* **34** no. 6, (2007) 995. `http://stacks.iop.org/0954-3899/34/i=6/a=S01`.

[110] R. Frühwirth, "Application of Kalman filtering to track and vertex fitting," *Nucl.Instrum.Meth.* **A262** (1987) 444–450.

[111] **CMS** Collaboration, "Performance of CMS muon reconstruction in pp collision events at $\sqrt{s} = 7$ TeV," *Journal of Instrumentation* **7** no. 10, (2012) P10002. `http://stacks.iop.org/1748-0221/7/i=10/a=P10002`.

[112] S. Baffioni, C. Charlot, F. Ferri, D. Futyan, P. Meridiani, *et al.*, "Electron reconstruction in CMS," *Eur.Phys.J.* **C49** (2007) 1099–1116.

[113] **CMS** Collaboration, V. Khachatryan *et al.*, "Performance of electron reconstruction and selection with the CMS detector in proton-proton collisions at sqrt(s)=8 TeV," `arXiv:1502.02701 [physics.ins-det]`.

[114] R. Frühwirth, "Track fitting with non-Gaussian noise," *Comput.Phys.Commun.* **100** (1997) 1–16.

[115] W. Adam, R. Frühwirth, A. Strandlie, and T. Todorov, "Reconstruction of electrons with the Gaussian-sum filter in the CMS tracker at the LHC," *Journal of Physics G: Nuclear and Particle Physics* **31** no. 9, (2005) N9. `http://stacks.iop.org/0954-3899/31/i=9/a=N01`.

[116] M. Pioppi, "A pre-identification for electron reconstruction in the CMS particle-flow algorithm," *Journal of Physics: Conference Series* **119** no. 3, (2008) 032039. `http://stacks.iop.org/1742-6596/119/i=3/a=032039`.

[117] S. Catani, Y. L. Dokshitzer, M. Seymour, and B. Webber, "Longitudinally invariant K_t clustering algorithms for hadron hadron collisions," *Nucl.Phys.* **B406** (1993) 187–224.

[118] S. D. Ellis and D. E. Soper, "Successive combination jet algorithm for hadron collisions," *Phys.Rev.* **D48** (1993) 3160–3166, `arXiv:hep-ph/9305266 [hep-ph]`.

[119] Y. L. Dokshitzer, G. Leder, S. Moretti, and B. Webber, "Better jet clustering algorithms," *JHEP* **9708** (1997) 001, `arXiv:hep-ph/9707323 [hep-ph]`.

[120] M. Cacciari, G. P. Salam, and G. Soyez, "The anti- k t jet clustering algorithm," *Journal of High Energy Physics* **2008** no. 04, (2008) 063. `http://stacks.iop.org/1126-6708/2008/i=04/a=063`.

[121] M. Cacciari, G. P. Salam, and G. Soyez, "FastJet User Manual," *Eur.Phys.J.* **C72** (2012) 1896, `arXiv:1111.6097 [hep-ph]`.

[122] M. Cacciari and G. P. Salam, "Dispelling the N^3 myth for the k_t jet-finder," *Phys.Lett.* **B641** (2006) 57–61, `arXiv:hep-ph/0512210 [hep-ph]`.

[123] **CMS** Collaboration, "Plans for Jet Energy Corrections at CMS," Tech. Rep. CMS-PAS-JME-07-002, 2008.

[124] **CMS** Collaboration, "Determination of jet energy calibration and transverse momentum resolution in CMS," *Journal of Instrumentation* **6** no. 11, (2011) P11002. `http://stacks.iop.org/1748-0221/6/i=11/a=P11002`.

[125] `https://twiki.cern.ch/twiki/bin/view/CMS/JetResolution`.

[126] **CMS** Collaboration, S. Chatrchyan *et al.*, "Identification of b-quark jets with the CMS experiment," *JINST* **8** (2013) P04013, `arXiv:1211.4462 [hep-ex]`.

[127] **ATLAS** Collaboration, "b-tagging in dense environments," Tech. Rep. ATL-PHYS-PUB-2014-014, CERN, Geneva, 2014. `https://cds.cern.ch/record/1750682`.

[128] **CMS** Collaboration, "Performance of b tagging at sqrt(s)=8 TeV in multijet, ttbar and boosted topology events," Tech. Rep. CMS-PAS-BTV-13-001, 2013.

[129] **CMS** Collaboration, "Missing transverse energy performance of the CMS detector," *Journal of Instrumentation* **6** no. 09, (2011) P09001. `http://stacks.iop.org/1748-0221/6/i=09/a=P09001`.

[130] N. Metropolis and S. Ulam, "The Monte Carlo Method," *Journal of the American Statistical Association* **44** no. 247, (1949) 335–341. PMID: 18139350.

[131] M. Dobbs and J. B. Hansen, "The HepMC C++ Monte Carlo event record for High Energy Physics," *Computer Physics Communications* **134** no. 1, (2001) 41 – 46.

[132] B. Andersson, G. Gustafson, G. Ingelman, and T. Sjöstrand, "Parton Fragmentation and String Dynamics," *Phys.Rept.* **97** (1983) 31–145.

[133] **CMS** Collaboration, "Pileup Jet Identification," Tech. Rep. CMS-PAS-JME-13-005, CERN, Geneva, 2013. `http://cds.cern.ch/record/1581583`.

[134] **GEANT4** Collaboration, S. Agostinelli *et al.*, "GEANT4: A Simulation toolkit," *Nucl.Instrum.Meth.* **A506** (2003) 250–303.

[135] J. Allison, K. Amako, J. Apostolakis, H. Araujo, P. Dubois, *et al.*, "Geant4 developments and applications," *IEEE Trans.Nucl.Sci.* **53** (2006) 270.

[136] M. Dobbs, S. Frixione, E. Laenen, K. Tollefson, H. Baer, *et al.*, "Les Houches guidebook to Monte Carlo generators for hadron collider physics," `arXiv:hep-ph/0403045 [hep-ph]`.

[137] J. Alwall, M. Herquet, F. Maltoni, O. Mattelaer, and T. Stelzer, "MadGraph 5 : Going Beyond," *JHEP* **1106** (2011) 128, `arXiv:1106.0522 [hep-ph]`.

[138] N. D. Christensen and C. Duhr, "FeynRules - Feynman rules made easy," *Comput.Phys.Commun.* **180** (2009) 1614–1641, `arXiv:0806.4194 [hep-ph]`.

[139] F. Maltoni and T. Stelzer, "MadEvent: Automatic event generation with MadGraph," *JHEP* **0302** (2003) 027, `arXiv:hep-ph/0208156 [hep-ph]`.

[140] J. Alwall, R. Frederix, S. Frixione, V. Hirschi, F. Maltoni, *et al.*, "The automated computation of tree-level and next-to-leading order differential cross sections, and their matching to parton shower simulations," *JHEP* **1407** (2014) 079, `arXiv:1405.0301 [hep-ph]`.

[141] S. Frixione and B. R. Webber, "Matching NLO QCD computations and parton shower simulations," *JHEP* **0206** (2002) 029, `arXiv:hep-ph/0204244 [hep-ph]`.

[142] P. Nason, "A New method for combining NLO QCD with shower Monte Carlo algorithms," *JHEP* **0411** (2004) 040, `arXiv:hep-ph/0409146 [hep-ph]`.

[143] E. Re, "Single-top Wt-channel production matched with parton showers using the POWHEG method," *Eur.Phys.J.* **C71** (2011) 1547, `arXiv:1009.2450 [hep-ph]`.

[144] R. Frederix, E. Re, and P. Torrielli, "Single-top t-channel hadroproduction in the four-flavour scheme with POWHEG and aMC@NLO," *JHEP* **1209** (2012) 130, `arXiv:1207.5391 [hep-ph]`.

[145] L. Hilser, "Monte-Carlo-Simulation des Single-Top + Jets Prozesses und Untersuchungen zur Notwendigkeit zusätzlicher Jets auf Matrixelement-Level für eine korrekte Beschreibung von Single-Top-Ereignissen," 2015. `https://ekp-invenio.physik.uni-karlsruhe.de/record/48620`. IEKP-BACHELOR-KA/2015-03.

[146] `https://twiki.cern.ch/twiki/bin/viewauth/CMS/SingleTopMC`.

[147] **CMS** Collaboration, J. Chou *et al.*, "Anomalous HB/HE Noise at Startup: Characteristics and Rejection Algorithms," CMS Internal Note 2010/006, 2010.

[148] `https://twiki.cern.ch/twiki/bin/view/CMS/MuonTagAndProbe`.

[149] `https://twiki.cern.ch/twiki/bin/viewauth/CMS/MuonReferenceEffs`.

[150] `https://twiki.cern.ch/twiki/bin/view/CMSPublic/SWGuideMuonId?rev=48#Tight_Muon`.

[151] `https://twiki.cern.ch/twiki/bin/view/CMS/MultivariateElectronIdentification`.

[152] https://twiki.cern.ch/twiki/bin/viewauth/CMS/ConversionTools.

[153] https://twiki.cern.ch/twiki/bin/viewauth/CMS/BtagPOG.

[154] M. Feindt, "A Neural Bayesian Estimator for Conditional Probability Densities," arXiv:physics/0402093.

[155] M. Feindt and U. Kerzel, "The NeuroBayes neural network package," *Nucl. Instrum. Meth.* **A559** (2006) 190–194.

[156] W. McCulloch and W. Pitts, "A logical calculus of the ideas immanent in nervous activity," *The Bulletin of Mathematical Biophysics* **5** no. 4, (1943) 115–133. http://dx.doi.org/10.1007/BF02478259.

[157] C. M. Bishop, *Neural Networks for Pattern Recognition*. Oxford University Press, Inc., 1995.

[158] F. Rosenblatt, "The Perceptron: A Probabilistic Model for Information Storage and Organization in the Brain," *Psychological Review* **65** no. 6, (1958) 386–408.

[159] M. Minsky and S. Papert, *Perceptrons: An Introduction to Computational Geometry*. MIT Press, 1988.

[160] G. Cybenko, "Approximation by superpositions of a sigmoidal function," *Mathematics of Control, Signals and Systems* **2** no. 4, (1989) 303–314.

[161] K. Hornik, "Approximation capabilities of multilayer feedforward networks," *Neural Networks* **4** no. 2, (1991) 251 – 257.

[162] C. G. Broyden, "The Convergence of a Class of Double-rank Minimization Algorithms 1. General Considerations," *IMA Journal of Applied Mathematics* **6** no. 1, (Mar., 1970) 76–90.

[163] R. Fletcher, "A New Approach to Variable Metric Algorithms.," *Comput. J.* **13** no. 3, (1970) 317–322.

[164] D. Goldfarb, "A Family of Variable-Metric Methods Derived by Variational Means," *Mathematics of Computation* **24** no. 109, (1970) pp. 23–26.

[165] D. F. Shanno, "Conditioning of Quasi-Newton Methods for Function Minimization," *Mathematics of Computation* **24** no. 111, (1970) pp. 647–656.

[166] D. Rumelhart, G. Hinton, and R. Williams, "Learning representations by back-propagating errors," *Nature* **323** no. 6088, (1986) 533–536.

[167] M. A. Nielsen, *Neural Networks and Deep Learning*. Determination Press, 2015.

[168] C. Böser, S. Fink, and S. Röcker, "Introduction to Boosted Decision Trees - A multivariate approach to classification problems," Slides of a talk given at the KSETA Doctoral Workshop 2014, Freudenstadt. `https://indico.scc.kit.edu/indico/event/48/session/4/contribution/35`.

[169] phi–t, *The NeuroBayes User's Guide*, 2012. Unpublished.

[170] J. Lück, *Observation of Electroweak Single Top-Quark Production with the CDF II Experiment*. PhD thesis, Karlsruhe Institute of Technology, 2009. IEKP-KA/2009-22.

[171] R. H. Byrd, P. Lu, J. Nocedal, and C. Zhu, "A Limited Memory Algorithm for Bound Constrained Optimization," *SIAM J. Sci. Comput.* **16** no. 5, (Sept., 1995) 1190–1208. `http://dx.doi.org/10.1137/0916069`.

[172] K. Pearson, "Note on Regression and Inheritance in the Case of Two Parents," *Proceedings of the Royal Society of London* **58** (1895) pp. 240–242. `http://www.jstor.org/stable/115794`.

[173] Th. Müller, J. Ott, and J. Wagner-Kuhr, "`theta` — A Framework for Template-Based Modeling and Inference," 2010. CMS-IN-2010/017 (internal).

[174] A. N. Tikhonov, "On the solution of ill-posed problems and the method of regularization," *Doklady Akademii Nauk SSR* **151** (1963) 501–504.

[175] D. L. Phillips, "A Technique for the Numerical Solution of Certain Integral Equations of the First Kind," *J. ACM* **9** no. 1, (Jan., 1962) 84–97.

[176] V. Blobel, "An Unfolding method for high-energy physics experiments," `arXiv:hep-ex/0208022 [hep-ex]`.

[177] J. Hadamard, "Sur les problèmes aux Dérivées partielles et leur signification physique," *Princeton University Bulletin* **13** (1902) 49–52.

[178] T. Peiffer, *Erste Messung der Ladungsasymmetrie und Suche nach schweren Resonanzen in der Top-Quark-Paarproduktion mit dem CMS-Experiment*. PhD thesis, 2011. IEKP-KA/2011-16.

[179] **CMS** Collaboration, "Inclusive and differential measurements of the $t\bar{t}$ charge asymmetry in pp collisions at $\sqrt{s} = 8$ TeV," Tech. Rep. CERN-PH-EP-2015-141. CMS-TOP-12-033-003. arXiv:1507.03119, CERN, 2015. `http://cds.cern.ch/record/2033253`. Submitted to Phys. Lett. B.

[180] https://twiki.cern.ch/twiki/bin/viewauth/CMS/JECUncertaintySources.

[181] https://twiki.cern.ch/twiki/bin/view/CMS/JetResolution#JER_Uncertainty.

[182] https://twiki.cern.ch/twiki/bin/viewauth/CMS/PileupSystematicErrors.

[183] **CMS** Collaboration, “Single top t-channel differential cross section at 8 TeV,” Tech. Rep. CMS-PAS-TOP-14-004, CERN, Geneva, 2014. `http://cds.cern.ch/record/1956681`.

[184] J. D. Bjorken and S. J. Brodsky, “Statistical Model for Electron-Positron Annihilation into Hadrons,” *Phys. Rev. D* **1** (Mar, 1970) 1416–1420. `http://link.aps.org/doi/10.1103/PhysRevD.1.1416`.

Danksagungen

An erster Stelle möchte ich mich bei Herrn Prof. Dr. Müller bedanken, der es mir ermöglichte in seiner TOP-Arbeitsgruppe mitzuarbeiten. Auf seine Unterstützung konnte ich stets zählen, sei es bei der Rückendeckung meiner Analysen oder durch die Möglichkeit Konferenzen und Schulen zu besuchen.

Meinem Korreferenten Herrn Prof. Dr. Günter Quast möchte ich für seine jahrelange Zusammenarbeit und Betreuung danken. In seinem Computing-Team konnte ich viele Erfahrungen sammeln. Ein besonderes Highlight bleibt für mich der Besuch der Grid-Konferenz in Dubna, den er ermöglichte.

Ohne meine zwei Betreuer wäre diese Arbeit nicht möglich gewesen. Ein sehr großer Dank gebührt Dr. Thorsten Chwalek, der nicht nur diese Arbeit betreut und korrekturgelesen hat, sondern auch einen Großteil meiner Analysen begleitet hat. Besonders zu Anfang diese Arbeit war Dr. Jeannine Wagner-Kuhr eine sehr große Hilfe. Auch der Austausch mit Prof. Dr. Ulrich Husemann und Dr. Matthias Mozer war sehr hilfreich.

Meinen Zimmerkollegen Dr. Christian Böser, Simon Fink und Benedikt Maier möchte ich für die angenehme Atmosphäre in unserem Büro danken. Danke an meine Kollegen Frank Roscher, Dr. Alexis Descroix und Shawn Williamson für den Austausch in und außerhalb der Physik. Danke auch an den ganzen Rest des IEKPs, insbesondere Captain Zanders tollkühne Crew, die wahren Gewinner der KSETA-Challenge, und den vielen ehemalige Kollegen: Dr. Jan Lück, Dr. Julia Bauer, Dr. Jasmin Gruschke, Dr. Jochen Ott, Dr. Manuel Zeise, Dr. Oliver Oberst, Dr. Michael Prim und Dr. Fred Stober.

Meinen Kollegen Dr. Daniel Martschei, Jens Hansen und Dr. Dennis Klingebiel möchte ich für ihren Einsatz danken, ohne den die 7 TeV Analyse mit den ersten Daten nicht möglich gewesen wäre. I would like to thank my colleagues Andrea Giammanco, Joosep Pata, Matthias Komm and Andres Tiko for the hard work they put into the polarization analysis. I would also like to thank the conveners Andrea, Rebeca, Orso, Luca, Andreas and Martijn for their supervision and support. I would to thank Wajid Ali Khan for the fun we had during his stay in Karlsruhe and the unique insight he provided into his culture.

Auch meinen Freunden in Stuttgart, Karlsruhe und im Hochhaus möchte ich herzlichst danken. Mit ihnen gab es ein Leben außerhalb der Physik das trotz Stress ziemlich viel Spaß gemacht hat. Die nötige Ablenkung von meiner Arbeit war zeitweise äußerst hilfreich. Besonders möchte ich mich bei Constanze Wille dafür bedanken, dass sie in der schwersten Zeit an meiner Seite stand und an mich glaubte.

Ein besonderer Dank gilt schlussendlich meinen Eltern sowie meiner Oma, die mich stets unterstützt und mir dieses Studium ermöglichten haben, sowie meinem Bruder Markus und meinen Verwandten.